Draft version May 26, 2026
Typeset using LaTeX **twocolumn** style in AASTeX7.0.1

GWTC-5.0: Constraints on the Cosmic Expansion Rate and Modified Gravitational-wave Propagation

The LIGO Scientific Collaboration, the Virgo Collaboration, and the KAGRA Collaboration

ABSTRACT

We employ 236 gravitational-wave (GW) sources in the fifth LIGO–Virgo–KAGRA Collaboration (LVK) Gravitational-Wave Transient Catalog (GWTC-5.0) to estimate the Hubble constant H_0. We compare the luminosity distance measured from GWs to the redshift inferred i) using features in the mass spectrum, and ii) using statistical host galaxy association. Probing the relationship between source luminosity distances and redshifts obtained in this way yields constraints on cosmological parameters. We estimate $H_0 = 71.0^{+9.0}_{-7.1}\,\mathrm{km\,s^{-1}\,Mpc^{-1}}$ (median with 68% symmetric credible interval). This combines information from the source-frame mass distribution with the H_0 measurement from GW170817 and its electromagnetic counterpart as well as galaxy catalog information from Dark Energy Survey Year 6 (DES-Y6). We improve over the GWTC-4.0 measurement by using more GW sources, some with significantly smaller sky localization volumes, which leads to a reduction by 25.7% of the H_0 uncertainty and a reconstructed mass distribution with lower uncertainties. We also constrain deviations from general relativity (GR) which affect GW propagation, specifically those that modify the luminosity distance inferred from the GW signal. We find no departures from GR in parameterized tests of GW propagation.

Keywords: Gravitational wave astronomy (675) – Gravitational wave sources (677) – Hubble constant (758) – Observational cosmology (1146)

1. INTRODUCTION

Obtaining independent measurements of the Hubble constant (H_0) is a major focus of gravitational-wave (GW) cosmology, driven by the existing discrepancy between early Universe measurements from the cosmic microwave background (CMB) radiation and local measurements from standardizable sources such as Type Ia supernovae (SNe Ia). Measurements of H_0 made by the Planck Collaboration in the Planck 2018 Data Release (Aghanim et al. 2020) and the Supernovae H0 for the Equation of State (SH0ES) project with the recalibration of supernovae by Large Magellanic Cloud Cepheids (Riess et al. 2022) have now reached an ∼8% discrepancy with $\gtrsim 5\sigma$ credibility, although other local measurements, including alternative methods of calibrating the distance ladder, suggest a smaller tension (e.g., Di Valentino & Brout 2024).

The possibility of using GW detections to infer cosmological parameters, such as H_0, was first proposed by Schutz (1986). GWs from compact binary coalescences (CBCs) serve as *standard sirens* (Holz & Hughes 2005), providing a self-calibrated measure of luminosity distance that is independent of traditional methods such as the cosmic distance ladder. If combined with redshift information, GWs can be used as probes of the luminosity distance-redshift relation, which depends on the cosmological model and its parameters. In this way GW sources may help to resolve the H_0 discrepancy, and can also provide insights into possible new physics beyond the standard Lambda cold dark matter (ΛCDM) cosmological model (Bull et al. 2016; Perivolaropoulos & Skara 2022; Abdalla et al. 2022; Di Valentino et al. 2025).

However, the redshift of a CBC source cannot be determined from the GW signal itself due to its degeneracy with the binary source masses (Krolak & Schutz 1987). Several methods have been proposed to break this degeneracy. If a counterpart in the electromagnetic (EM) spectrum can be uniquely associated to the GW event, the redshift of the host galaxy can be determined via astronomical photometry or spectroscopy (Holz & Hughes 2005; Dalal et al. 2006; Nissanke et al. 2010, 2013; Abbott et al. 2017a; Chen et al. 2018; Feeney et al. 2019) - referred to as a *bright* siren. The only bright siren observed to date is the binary neutron star (BNS) merger GW170817 (Abbott et al. 2017b), which, combined with coincident EM transients associated with the host galaxy NGC 4993 (Abbott et al. 2017c), provided the first bright standard siren measurement of H_0 (Abbott et al. 2017a). In the absence of further bright siren events, the steady increase of detections

Corresponding author:
LSC P&P Committee via LVK Publications as proxy
lvc.publications@ligo.org

from binary black hole (BBH), neutron star–black hole binary (NSBH) and other BNS candidates without confident EM counterparts has driven forward other methods to measure H_0.

One approach relies on the presence of features in the mass spectrum of binary compact objects to break the mass–redshift degeneracy (Chernoff & Finn 1993; Markovic 1993; Taylor et al. 2012; Farr et al. 2019; You et al. 2021; Mastrogiovanni et al. 2021; Ezquiaga & Holz 2021, 2022), referred to as the *spectral* siren method (also sometimes called the *population* method). The cosmological parameters are sampled together with a set of population parameters describing the intrinsic CBC parameter distribution (for instance the source-frame masses) and the CBC merger rate.

A second approach, referred to as the *dark* siren method (also called *galaxy catalog* method), consists of supplementing the spectral siren method with additional redshift information from galaxy surveys (Schutz 1986; MacLeod & Hogan 2008; Del Pozzo 2012; Nishizawa 2017; Fishbach et al. 2019; Soares-Santos et al. 2019; Gray et al. 2020; Palmese et al. 2020; Abbott et al. 2021a; Finke et al. 2021a; Abbott et al. 2023a; Gair et al. 2023; Borghi et al. 2024; Bom et al. 2024). Alternative approaches to infer the source redshift, which we will not consider in this work, take advantage of the cross-correlation between the spatial distribution of GWs and galaxies (Camera & Nishizawa 2013; Oguri 2016; Mukherjee et al. 2020, 2021b, 2024; Afroz & Mukherjee 2024; Fonseca et al. 2023; Zazzera et al. 2025; Ferri et al. 2024; Pedrotti et al. 2025; Cheng & Gair 2026), the adoption of theoretical priors on the merger-redshift distributions (Ding et al. 2019; Ye & Fishbach 2021), and the use of tidal distortions of neutron stars (NSs) (Messenger & Read 2012; Del Pozzo et al. 2017; Chatterjee et al. 2021).

Both spectral and dark siren approaches have been applied in Abac et al. (2025b) to the merger candidates reported in the fourth Gravitational-Wave Transient Catalog (GWTC) (Abac et al. 2025c) using the latest version of the codes used by the LIGO–Virgo–KAGRA Collaboration (LVK), `gwcosmo`[1] (Gray et al. 2020, 2022, 2023; Papadopoulos et al. 2026) and `icarogw`[2] (Mastrogiovanni et al. 2023, 2024). Both codes implement the dark siren method allowing marginalization over the GW population parameters, while incorporating galaxy catalog information. This approach delivers cosmological constraints that are more robust to the systematic uncertainties introduced by fixing population parameters (Mastrogiovanni et al. 2021; Abbott et al. 2023a; Pierra et al. 2024b; Agarwal et al. 2025).

The second part of the fourth observing run (O4b) of the LVK network of detectors began on 2024 April 10 at 15:00:00 UTC, following the end of the first part of the fourth observing run (O4a) which ended on 2024 January 16 at 16:00:00 UTC. O4b included the two Laser Interferometer Gravitational-Wave Observatory (LIGO; Aasi et al. 2015) detectors and the Virgo detector (Acernese et al. 2015) in observing mode, while the KAGRA (Akutsu et al. 2021) detector did not join the observing run. O4b ended on 2025 January 28 at 17:00:00 UTC, and the accompanying version of the GWTC, hereafter referred to as GWTC-5.0 (Abac et al. 2026a,b,c), contains all the candidates reported in previous observing runs, which include the first observing run (O1; Abbott et al. 2016), the second observing run (O2; Abbott et al. 2019), the third observing run (O3; Abbott et al. 2021b, 2023b, 2024), and O4a (Abac et al. 2025c) in addition to the latest observations from O4b. See (Abac et al. 2026a) for a general introduction to GWTC-5.0, and the articles presented in the GWTC-5.0 Focus Issue (Abac et al. 2026d) for other aspects of this data set.

In this paper we present an updated estimate of H_0 using the full population of BNS, NSBH, and BBH candidates reported in GWTC-5.0. We select candidates for inclusion in the analysis based on a false alarm rate (FAR) of less than 0.25 per year to reduce contamination from noise events. This allows us to combine the bright siren event GW170817 with an additional 235 GW detections used as dark sirens to obtain our final estimate of H_0 with a total of 236 candidates.

In addition, we present constraints on deviations from general relativity (GR) that affect the propagation of GWs and which can be parameterized in terms of a modified GW–EM luminosity-distance ratio (Belgacem et al. 2018a; Ezquiaga 2021; Mancarella et al. 2022; Leyde et al. 2022; Mastrogiovanni et al. 2023; Chen et al. 2024a; Abac et al. 2025b). These constraints test the hypothesis that gravity behaves differently from GR on cosmological scales, which is interpreted as the existence of a dark energy component (see Clifton et al. 2012 for a comprehensive review of modified gravity models).

The remainder of this paper is organized as follows. In Section 2 we summarize the spectral and dark siren statistical methods adopted in this study to jointly infer the cosmological and population parameters. In Section 3 we detail the properties of the GW candidates and the galaxy catalog used. In Section 4 we present the results of our analysis and the tests made to check its robustness against systematic errors, while in Section 5 we discuss how our results compare with the literature and the limitations of our analysis. In Section 6 we present our conclusions.

Throughout this paper, unless otherwise stated, we assume a flat-ΛCDM cosmology and the best-fit Planck-2015 value of $\Omega_\mathrm{m} = 0.3065$ for the fractional matter density in the current epoch (Ade et al. 2016).

---

[1] https://git.ligo.org/lscsoft/gwcosmo

[2] https://github.com/simone-mastrogiovanni/icarogw

2. METHODS

2.1. *Dark Siren Statistical Framework*

To jointly infer cosmology and population–level properties of GW sources from the observed event catalog, we employ a hierarchical Bayesian framework (Mandel et al. 2019; Thrane & Talbot 2019; Vitale et al. 2020). The observed sample is modeled as resulting from an inhomogeneous Poisson process in the presence of selection effects, assuming statistically independent and non-overlapping events. Each event in the catalog is described by detector–frame parameters $\boldsymbol{\theta}^{\rm det}$, which include the detector–frame masses and GW luminosity distance, $\boldsymbol{\theta}^{\rm det} \ni \{m_1^{\rm det}, m_2^{\rm det}, D_{\rm L}^{\rm GW}\}$ (where $m_1^{\rm det} \geq m_2^{\rm det}$). For each event, labeled by the index i, individual parameter constraints are given in the form of samples from the posterior probability $p\big(\boldsymbol{\theta}_i^{\rm det}|d_i\big)$ for the parameters $\boldsymbol{\theta}_i^{\rm det}$ given the observed data d_i. These are assumed to be obtained with a parameter estimation prior that we denote $\pi_{\rm PE}(\boldsymbol{\theta}^{\rm det})$. The event parameters are drawn from a distribution which is modeled as a function of source–frame quantities $\boldsymbol{\theta}$, which include the source–frame masses and redshift, $\boldsymbol{\theta} \ni \{m_1, m_2, z\}$. The population distribution $p_{\rm pop}(\boldsymbol{\theta}|\boldsymbol{\Lambda})$ is described parametrically by a set of *hyperparameters* $\boldsymbol{\Lambda}$ (sometimes simply referred as *parameters*) that includes the cosmological parameters $\boldsymbol{\Lambda}_{\rm c}$, and the parameters describing the astrophysical distribution of sources, such as the mass distribution and the redshift evolution of the merger rate. The set of hyperparameters is inferred through the population-level likelihood, given by (Loredo 2004; Mandel et al. 2019; Vitale et al. 2020)

$$p\left(\{d_i\}_{i=1}^{N_{\rm det}}|\boldsymbol{\Lambda}\right) \propto \xi(\boldsymbol{\Lambda})^{-N_{\rm det}} \prod_{i=1}^{N_{\rm det}} \int {\rm d}\boldsymbol{\theta}_i^{\rm det} \, \frac{p\big(\boldsymbol{\theta}_i^{\rm det}|d_i\big)}{\pi_{\rm PE}(\boldsymbol{\theta}_i^{\rm det})} \times \left[\left|\frac{{\rm d}\boldsymbol{\theta}_i^{\rm det}(\theta,\boldsymbol{\Lambda})}{{\rm d}\boldsymbol{\theta}_i}\right|^{-1} p_{\rm pop}(\boldsymbol{\theta}_i|\boldsymbol{\Lambda})\right], \quad (1)$$

where $\xi(\boldsymbol{\Lambda})$ is the expected fraction of detected events in the population, accounting for selection effects, and the Jacobian term $\left|{\rm d}\boldsymbol{\theta}_i^{\rm det}/{\rm d}\boldsymbol{\theta}_i\right|$ accounts for the transformation from source to detector frame. Finally, $N_{\rm det}$ is the total number of detected events in the catalog, and we assume marginalization over the overall total number of mergers in the observing time, N, with a scale–invariant prior $\propto 1/N$ (Mandel et al. 2019).

A description of the implementation of the likelihood computation is provided in the O4a cosmology paper (Abac et al. 2025b). Throughout, we use two pipelines to sample from the hyperparameter posterior: `icarogw` and `gwcosmo` (Mastrogiovanni et al. 2024; Papadopoulos et al. 2026) that adopt different strategies to evaluate the posterior in Eq. (1).

2.2. *Construction of Redshift Priors*

In this section, we summarize the most relevant aspects of the construction of redshift distributions as a function of sky position. Since the methodological framework is virtually unchanged when compared to the GWTC-4 analysis (Abac et al. 2025b), we only focus on the most relevant equations and refer to Mastrogiovanni et al. (2023); Gray et al. (2023) for further details.

The line-of-sight redshift prior for a specific element in the sky, Ω, receives two contributions

$$p(z|\Omega) \propto \frac{\psi(z|\boldsymbol{\Lambda})}{1+z}\left[\frac{{\rm d}N_{\rm gal,cat}^{\rm eff}}{{\rm d}z{\rm d}\Omega} + \frac{{\rm d}N_{\rm gal,out}^{\rm eff}}{{\rm d}z{\rm d}\Omega}\right], \quad (2)$$

where $\psi(z|\boldsymbol{\Lambda})$ parametrizes the redshift dependence of the CBC merger rate and the factor of $(1+z)^{-1}$ accounts for the conversion of time intervals from source to observer frame. The terms in square brackets represent the contributions to the redshift prior from galaxies within the catalog (first term), and a model for unobserved 'out-of-catalog' galaxies (second term).

In–catalog part, ${\rm d}N_{\rm gal,cat}^{\rm eff}/({\rm d}z{\rm d}\Omega)$—This term is built starting from the galaxies in the catalog. The sky is divided in equal–size pixels, labeled with their central coordinates Ω, with the `healpix` pixelization algorithm (Górski et al. 2005; Zonca et al. 2019). Inside each pixel, we select all galaxies with apparent magnitude smaller than the median inside the pixel, denoted as $m_{\rm thr}(\Omega)$.

For each pixel, a redshift prior is constructed as a weighted sum of the posterior distributions for the true redshift z given observed redshifts $z_{\rm obs}^j$ for the selected galaxies $j = 1, \ldots, N_{\rm gal}(\Omega)$ in the pixel, each denoted by $p(z|z_{\rm obs}^j, \sigma_{z,{\rm obs}}^j, \boldsymbol{\Lambda}_{\rm c})$, where $\sigma_{z,{\rm obs}}^j$ stands for redshift uncertainty (standard deviation of a Gaussian). The weight each galaxy contributes with is computed from the absolute magnitude of each galaxy, M_j (or equivalently its absolute luminosity L_j),

$$w_j(\epsilon, M_j) = \left|\frac{L_j}{L_*}\right|^{\epsilon} = 10^{-0.4\epsilon(M_j - M_*)}, \quad (3)$$

(Gray et al. 2020), where L_* and M_* are the reference luminosity and corresponding magnitude at the knee of the luminosity function, respectively. We assume the luminosity function to be given by the Schechter (1976) form, described in more detail in Appendix B of Abac et al. (2025b).

In Eq. (3), we weight each galaxy by the absolute luminosity in a specific band, L_j, raised to a power ϵ which we treat as a fixed parameter. In particular, we consider the cases $\epsilon = 0$, corresponding to equal probability for all galaxies to host CBCs, which we will refer to as *no–weighting* case, and $\epsilon = 1$ corresponding to a linear weight of galaxies by their luminosity, which we will refer to as *luminosity–weighting* case. It is known that luminosity in specific magnitude bands correlates with galaxy properties such as stellar mass or star formation rate, for example (Neijssel et al. 2019; Adhikari et al. 2020; Santoliquido et al. 2021; Broekgaarden et al. 2022; Rauf et al. 2023; Srinivasan et al. 2023; Hanselman et al. 2025; Li et al. 2025b). Luminosity–weighting reflects an assumption that such galaxy properties may also correlate with likelihood to host CBCs, see e.g. O'Shaughnessy et al. (2017); Artale et al. (2019); Gray et al. (2020); Vijaykumar et al. (2024) for more extended discussions.

For the out-of-catalog contribution, see Appendix B of Abac et al. (2025b) for details.

2.3. *Population Models*

We construct CBC rate models from independent redshift and source mass distributions, and while we assume in most analyses the CBC spins to be isotropically distributed with uniform distribution in the spin magnitudes, in a subset of analyses we additionally model the spin population.

We consider three different models for the distribution of primary mass, $p\,(m_1|\mathbf{\Lambda})$, which enters the term $p_{\rm pop}$ in Eq. (1). These models are denoted as: MULTI PEAK (MLTP), FULLPOP-4.0 and FULLPOP 3 PEAKS. These are phenomenological parametric models defined in terms of relatively simple functional forms that contain features motivated by either astrophysical expectations or previous GW observations. These models are constructed as superpositions of truncated Gaussian and power–law distributions with different parameters (described in Appendix A). In this work we consider these mass models as redshift-independent; see Mukherjee (2022); Karathanasis et al. (2023); Rinaldi et al. (2024); Heinzel et al. (2025); Lalleman et al. (2025); Gennari et al. (2025); Abac et al. (2026e) for investigations into their possible evolution. We will comment upon this further in Section 5.2.

Figure 1 shows a sketch of the typical form of these models, with the different mass features that characterize them highlighted. We briefly describe these models next (see Appendix A and Abac et al. 2026e for more details). The POWERLAW+PEAK (PLP) model used in Abac et al. (2025b) has not been continued in this work: it was slightly disfavored relative to MLTP in Abac et al. (2025b), and we find it more strongly disfavored with GWTC-5.0.

The MLTP mass model was originally introduced in Abbott et al. (2021c). It features a power–law distribution for the primary mass spectrum with a smooth low–mass cutoff and includes a pair of Gaussian peaks to capture excesses at intermediate masses. This model is similar to the BROKEN POWER LAW + 2 PEAKS model adopted in Abac et al. (2025d), except our model has one power law instead of two. This model is characterized by eleven population parameters.

In the MLTP model the full mass distributions are factorized as

$$p(m_1, m_2|\mathbf{\Lambda}) = p(m_1|\mathbf{\Lambda})\, S_{\rm h}(m_1|\mathbf{\Lambda}) \times p(m_2|m_1, \mathbf{\Lambda})\, S_{\rm h}(m_2|\mathbf{\Lambda}), \tag{4}$$

where $p\,(m_2|m_1, \mathbf{\Lambda})$ is the distribution of the secondary mass component conditioned on the primary mass and $S_{\rm h}(m|\mathbf{\Lambda})$ is a smoothing function defined in Appendix C of Abac et al. (2025b). This is modeled assuming that the mass ratio $q = m_2/m_1$ follows a power–law distribution.

The FULLPOP-4.0 model is a generalization of the MLTP, extending the distribution to encompass the full mass spectrum of CBCs, including BNS, NSBH, and BBH mergers. It is designed to cover a wide mass range, from a few to several hundred solar masses (Fishbach et al. 2020; Farah et al. 2022; Mali & Essick 2025a). The model combines a first power–law component for the low–mass region (representing NS-containing events) with a smooth low–mass cut–off, and a second power–law component for the BBH mass distribution, which includes two Gaussian peaks. A dip function is introduced at the junction between the two power–law regimes, aiming to model the apparent mass gap between NSs and BHs. The parameters governing this dip are treated as population parameters. This model is characterized by nineteen parameters.

By modeling the full population of compact objects in a unified framework, the FULLPOP-4.0 model allows us to include a larger set of GW events in our analysis, offering greater sensitivity to features in the mass spectrum. Another major distinction from the MLTP mass model lies in the parametrization of the secondary mass. Instead of modeling m_2 as a power–law conditioned on m_1, as in Eq. (4), the FULLPOP-4.0 model assumes that the distribution of m_2 is given by $p(m_2|\mathbf{\Lambda})$ and employs a pairing function $f(m_1, m_2|\mathbf{\Lambda})$ enforcing the condition $m_1 \geq m_2$ and allowing for further flexibility for the secondary mass (Fishbach & Holz 2020), with

$$p(m_1, m_2|\mathbf{\Lambda}) \propto\; p_{\rm S}(m_1|\mathbf{\Lambda})\, p_{\rm S}(m_2|\mathbf{\Lambda}) f(m_1, m_2|\mathbf{\Lambda})\,, \tag{5}$$

where $p_{\rm S}(m|\mathbf{\Lambda})$ is defined in terms of $p(m|\mathbf{\Lambda})$ and the smoothing functions defined in Appendix C of (Abac et al. 2025b).

Finally, we include a further extension of the FULLPOP-4.0 model, which we denote as FULLPOP 3 PEAKS, which was first used in Pierra & Papadopoulos (2026). This model modifies the FULLPOP-4.0 mass distributions by the addition of a third Gaussian peak intended to model further structure in the BBH mass distribution.

The equations which describe our three population models can be found in Appendix A. For more details, see also Abac et al. (2026e). In Section 4 we compare our analysis obtained using *single–population* models (the MLTP model which is valid for BBH candidates only)

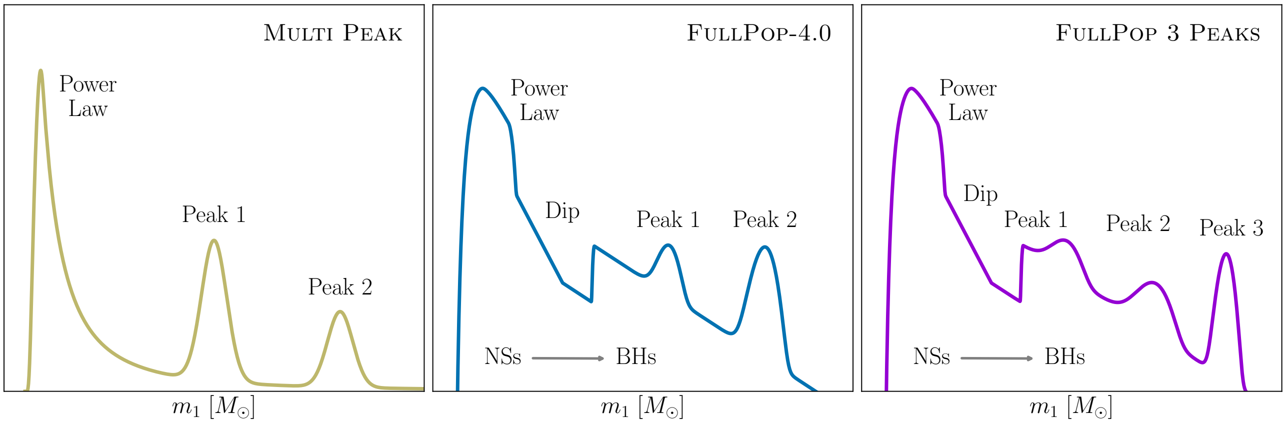

Figure 1. Qualitative graphical representation of the three source-frame mass models considered in this paper and described in Section 2.3 and Appendix A. The mass distribution model displayed in the first panel represent the mass ranges of black holes (BHs), while the second two panels include both BHs and NSs. The mass ranges shown are not to scale.

to that obtained using a *multi-population* model (BNS + NSBH + BBH candidates), i.e., the FullPop-4.0 and FullPop 3 Peaks models.

For the merger rate evolution as a function of the redshift, the term $\psi(z|\mathbf{\Lambda})$ in Eq. (2), is modeled with a Madau–Dickinson parametrization (Madau & Dickinson 2014), which is characterized by parameters $\{\gamma, \kappa, z_\mathrm{p}\} \in \mathbf{\Lambda}$, see Eq. (A.2) in Appendix A for details. In particular, the parameter γ controls the low–redshift slope of the merger rate, with $\psi(z) \propto (1+z)^\gamma$ for $z \ll z_\mathrm{p}$.

In addition, rather than assuming that the spin magnitudes are uniformly distributed and that their orientations are isotropic, these properties can be jointly modeled and inferred alongside the mass and merger rate distribution, defined as an extra $p_\mathrm{pop}(\cdot)$ term in Eq. (1). Such inclusion to the inference framework makes it more general, through a more complete modeling of the CBC population, and potentially could improve the constraints on the cosmology. In this work, we consider two parametrizations, to model the full spin distribution denoted by

$$p(\vec{\chi}, \cos\vec{\theta}|\mathbf{\Lambda}) = p(\vec{\chi}|\mathbf{\Lambda}) p(\cos\vec{\theta}|\mathbf{\Lambda}), \tag{6}$$

factorized as the product between the PDF for the spin magnitude part $p(\vec{\chi}|\mathbf{\Lambda})$ and tilt angles part $p(\cos\vec{\theta}|\mathbf{\Lambda})$. The first parametrization, called the Gaussian model, assumes that the spin magnitudes for each component are given by truncated Gaussian distributions over $[0,1]$, while the tilt angles are given by a mixture model between a uniform distribution between $[-1,1]$ and a truncated Gaussian centered around unity. This model is directly taken from Abac et al. (2025d). The second spin model is taken from Pierra et al. (2024a), in particular we use the so-called Transition model which allows for a possible transition between two spin magnitude distributions via the mass, both described with truncated Gaussians between 0 and 1. The PDF for the spin magnitude now depends directly on the masses and reads as

$$\begin{split}\pi(\chi|m,\Lambda) = {} & W(m)\mathcal{N}_{1,[0,1]}(\chi|\mu_{\chi_1},\sigma_{\chi_1}) + \\ & + (1-W(m))\mathcal{N}_{2,[0,1]}(\chi|\mu_{\chi_2},\sigma_{\chi_2})\,,\end{split} \tag{7}$$

where $W(m)$ is a mass dependent window function which can transition from an initial value λ_f to 0. The window function is constructed as a logistic function such that

$$W(m; m_\mathrm{t}, \delta_{m_\mathrm{t}}, \lambda_\mathrm{f}) = \frac{\lambda_\mathrm{f}}{1 + e^{\frac{m - m_\mathrm{t}}{\delta_{m_\mathrm{t}}}}}\,, \tag{8}$$

where m_t is the mass at which the first spin magnitude distribution transitions to the second one and δ_{m_t} controls the steepness of that transition. With the Transition prescription, the angle distribution of the spins is the same as for the Gaussian model.

Such a spin model is of interest given the recent evidence for correlations between the spin magnitudes and masses of BBHs (Pierra et al. 2024a; Li et al. 2024b; Abac et al. 2025d; Li et al. 2025a). These correlations could improve the resulting H_0 constraint through a more faithful reconstruction of a spin-dependent feature of the mass distribution.

2.4. *Cosmological Models*

2.4.1. *Background Evolution*

Under the assumptions of homogeneity and isotropy, the luminosity distance can be computed based on the Friedmann–Lemaître–Robertson–Walker (FLRW) metric as

$$D_\mathrm{L} = \frac{c(1+z)}{H_0}\int_0^z \frac{\mathrm{d}z'}{E(z')}\,, \tag{9}$$

where $E(z) = H(z)/H_0$ is the dimensionless expansion rate of the Universe. This depends on the cosmological model assumed and can be computed using the Friedmann equations. In this paper, we restrict our focus to a flat–ΛCDM model. Under this assumption, $E(z)$ is given by

$$E(z) = \left[\Omega_{\rm m}(1+z)^3 + \Omega_\Lambda\right]^{1/2} . \tag{10}$$

Here, $\Omega_{\rm m}$ is the fractional energy density in matter components today (cold dark matter + baryonic matter), and we have ignored the radiation energy density which is negligible at the redshifts of our interest. Under this approximation, the dark energy density fraction today is $\Omega_\Lambda = 1 - \Omega_{\rm m}$.

As our data currently have no constraining power on the equation–of–state parameter of dark energy w_0, our main results will be based on the flat–ΛCDM model with $w_0 = -1$.

2.4.2. *Models of Modified GW Propagation*

We also analyze our data in the context of cosmological modified–gravity models. Some of the analyses presented here are continued from (Abac et al. 2025b), where more extensive details can be found. We focus here on a common feature of these models, sometimes referred to as *GW friction* (Saltas et al. 2014; Pettorino & Amendola 2015; Nishizawa 2018; Amendola et al. 2018; Lagos et al. 2019). Under this effect, new terms in the GW propagation equation result in modifications to the GW amplitude received at the observer. This effect is indistinguishable from a change in the luminosity distance to the GW source. The result is that the luminosity distance $D_{\rm L}^{\rm GW}$ inferred for a GW source differs from the EM luminosity distance $D_{\rm L}$ given by Eq. (9). Any measurement of the GW source luminosity distance obtained using EM observables would be unaffected, i.e., $D_{\rm L}^{\rm EM} = D_{\rm L}$.

Based on this, multiple studies (Belgacem et al. 2018b,a, 2019b,a; Mukherjee et al. 2021c; Finke et al. 2021a,b, 2022; Ezquiaga 2021; Finke et al. 2021a; Mancarella et al. 2022; Kalogera et al. 2021; Leyde et al. 2022; Liu et al. 2024; Branchesi et al. 2023; Chen et al. 2024a; Abac et al. 2025a) have considered the ratio $D_{\rm L}^{\rm GW}/D_{\rm L}^{\rm EM}$ as a convenient probe of departures from GR on cosmological scales. This ratio, equal to one in GR, can become a function of redshift in cosmological modified–gravity models. Here we consider two commonly used parameterized forms for the GW–EM luminosity-distance ratio.

Two assumptions are relevant to both parameterized forms. Firstly, we assume the GW propagation speed, c_T, is luminal due to the tight constraint on this parameter from GW170817 (Abbott et al. 2017d). Secondly, we treat departures from GR impacting only the propagation phase of GW signals. That is, we do not consider modifications to the generation of GWs, which would affect the waveform *at source.*

Ξ_0–n Parametrization—In this parametrization, $D_{\rm L}^{\rm GW}$ is described by (Belgacem et al. 2018a)

$$D_{\rm L}^{\rm GW} = D_{\rm L}^{\rm EM}\left(\Xi_0 + \frac{1-\Xi_0}{(1+z)^n}\right) , \tag{11}$$

where both parameters Ξ_0 and n are positive. The primary parameter of interest is Ξ_0, which controls the overall amplitude of departures from GR. At low redshifts, $D_{\rm L}^{\rm GW}/D_{\rm L}^{\rm EM} \to 1$ (irrespective of Ξ_0). At high redshifts, $D_{\rm L}^{\rm GW}/D_{\rm L}^{\rm EM} \to \Xi_0$ as changes to $D_{\rm L}^{\rm GW}$ should saturate at redshifts where the fractional energy density of dark energy, $\Omega_\Lambda(z)$, is negligible. This holds under the assumption that deviations from GR are associated to the late–time emergence of dark energy. The power–law index n controls the rate of transition between these two regimes.

The specific form of the Ξ_0–n parametrization is an assumption, and Eq. (11) was calibrated to cover a large spectrum of known luminal modified–gravity theories (Belgacem et al. 2019b). The GR limit of the theory is $\Xi_0 \to 1$ (for any value of n). However, the parametrization is imperfectly behaved, since $n \to 0$ also recovers the GR behavior $D_{\rm L}^{\rm GW} = D_{\rm L}^{\rm EM}$.

α_M Parametrization—This parametrization is inspired by Horndeski gravity (Horndeski 1974; Deffayet et al. 2011; Kobayashi et al. 2011), which is the most general family of scalar–tensor gravity models with second-order equations of motion. See Kobayashi (2019) and references therein for a review of Horndeski gravity and its phenomena. In the widespread basis of Bellini & Sawicki (2014), adopted for describing linear cosmological perturbations of Horndeski theories around a FLRW solution, $\alpha_M(z)$ is the rate of change of the effective Planck mass, and hence the effective gravitational coupling strength (Bellini & Sawicki 2014; Gleyzes et al. 2015). This results in the following expression for $D_{\rm L}^{\rm GW}$ (Lagos et al. 2019):

$$D_{\rm L}^{\rm GW} = D_{\rm L}^{\rm EM} \exp\left\{\frac{1}{2}\int_0^z \frac{{\rm d}z'}{1+z'}\alpha_M\left(z'\right)\right\} , \tag{12}$$

where in this work we will use the following ansatz for $\alpha_M(z)$

$$\alpha_M(z) = c_M \frac{\Omega_\Lambda(z)}{\Omega_\Lambda} = c_M \frac{1}{E^2(z)} , \tag{13}$$

where $\Omega_\Lambda = \Omega_\Lambda(z=0)$ and c_M is a constant of proportionality. For the dimensionless expansion rate, $E(z)$, we use Eq. (10) which assumes a flat–ΛCDM model with constant dark energy density, as in this work we are not considering changes to the cosmological expansion history. In principle, $\alpha_M(z)$ also enters the background evolution equations; however, any resulting change can be absorbed into other functions such as the effective dark energy equation of state (Bellini & Sawicki 2014). The GR limit of the model is obtained for $c_M = 0$.

The redshift–dependent form of $\alpha_M(z)$ is a choice. The form of Eq. (13) has been widely adopted for large scale structure (LSS) constraints (Bellini et al. 2016; Noller & Nicola 2019; Baker & Harrison 2021; Seraille et al. 2024; Ishak et al. 2024).

Connection to gravitational coupling.—We noted above that, in Horndeski gravity, the function $\alpha_M(z)$ controls the rate of change of an effective gravitational coupling strength. As detailed further in Appendix F, in Horndeski gravity the following relation holds:

$$\frac{G_{\rm GW}(z)}{G_{\rm GW}(0)} = \left(\frac{D_{\rm L}^{\rm GW}}{D_{\rm L}^{\rm EM}}\right)^2 \tag{14}$$

where $G_{\rm GW}(z)$ is an effective gravitational coupling associated to GW propagation, which may be redshift-dependent. In GR this quantity would be Newton's constant, $G_{\rm N}$. A change in the value of $G_{\rm GW}(z)$ between $z_{\rm source}$ and $z = 0$ is a common leading-order change to GW propagation in Horndeski gravity. By squaring our constraints on the GW-EM distance ratio, we can interpret our constraints in this light via Eq. (14).

We note that a different gravitational coupling strength can also be constrained by large-scale structure surveys (LSS), sometimes denoted $G_{\rm eff}$, $G_{\rm matter}$ or μ. The quantities $G_{\rm GW}$ and $G_{\rm eff}$ can be the same under some conditions, which allows for a comparison of GW and LSS results (Bellini & Sawicki 2014; Gleyzes et al. 2015; Perenon et al. 2015; Beltran Jimenez et al. 2016; Romano 2025).

3. DATA

3.1. *GW Events*

The analyses presented here use GWTC-5.0 and are based on the detection of GW candidates produced by merging compact binaries between O1 and the end of O4b. To reduce the noise contamination of the datasets used in cosmological studies, we select a subset of GW events with the lowest FAR among all search pipelines, ensuring all events have FAR $< 0.25\,{\rm yr}^{-1}$.

A total of 236 CBC GW candidates with FARs below this threshold have been detected by our search pipelines: cWB-BBH (Klimenko et al. 2005, 2008, 2016; Mishra et al. 2025), GstLAL (Messick et al. 2017; Sachdev et al. 2019; Tsukada et al. 2023; Sakon et al. 2024; Joshi et al. 2025), MBTA (Alléné et al. 2025), and PyCBC (Allen et al. 2012; Dal Canton et al. 2014; Usman et al. 2016; Nitz et al. 2017). Following the GWTC-5.0 classification of candidates into potential BBHs or NS-binaries (Abac et al. 2026c), 231 out of 236 events are believed to originate from the coalescence of BBH candidates and 5 from binaries where at least one component could have been a NS. This analysis includes the 141 dark siren events considered in our previous cosmological analysis of GWTC-4.0 (Abac et al. 2025b). As in the GWTC-4.0 analysis, we exclude GW231123_135430 (Abac et al. 2025e), as some of its inferred properties, such as the binary masses or its luminosity distance, vary dramatically with different waveforms, and the reason for these differences is not well understood. Added to the 235 dark sirens is the special case of the multi-messenger event GW170817, which is again treated differently from the others and will be used in the rest of the paper as a bright siren.

Figure 2 shows the cumulative distribution of the 90% credible region (CR) of the sky localization of CBC events observed in all LVK observing runs since O1, as well as that of the O4b events only. The sky localization of the GW events detected during the O4b observing run is, on average, better than previous events and markedly more precise than O4a events (see Figures 2 and 3). This improvement can be attributed to the participation of Virgo in O4b (which was not observing in O4a), resulting in better triangulation from three detectors (Essick et al. 2015; Ouzriat et al. 2025). A full list of luminosity distances and sky uncertainties of the GW candidates considered in our study can be found in Appendix G.

Different waveform models have been used to perform the parameter estimation (PE) for each GW candidate across the observing runs (Abac et al. 2026b). For our analysis, we use posterior samples produced with a single waveform approximant rather than a mixture of samples from different waveforms (Abac et al. 2026b,c) to mitigate potential systematics. In particular, for candidates from the O1, O2, and O3 runs, we use the posterior samples based on the IMRPhenomXPHM waveform model (Pratten et al. 2021), where for GW200115_042309 (Abbott et al. 2021d) we use the large-spin magnitude prior posterior samples, while for the BNS mergers GW190425_081805 (Abbott et al. 2020) and GW170817 (Abbott et al. 2021a) we use the large-spin magnitude prior posterior samples obtained with the IMRPhenomPv2_NRTidal (Dietrich et al. 2017, 2019) and a prior allowing for high-spin and low-spin magnitudes, respectively. For events from both the O4a and O4b observing runs, we use the posterior samples produced with the IMRPhenomXPHM_SpinTaylor model (Colleoni et al. 2025), except for GW230529_181500, for which we use posterior samples produced using the IMRPhenomXPHM waveform model and released in Abac et al. (2024). In this study we do not consider the impact of waveform systematics, as they are expected to be relevant only in population analyses of GW events with signal-to-noise ratio (SNR) above 100 (Kapil et al. 2024; Dhani et al. 2025).

Finally, we estimate the GW detection probability in denominator of Eq. (1) by using a set of simulated GW signals (called injections) (Essick et al. 2025; Abac et al. 2026b). More details on how the injections are used to compute this expression can be found in Appendix A of Abac et al. (2025b).

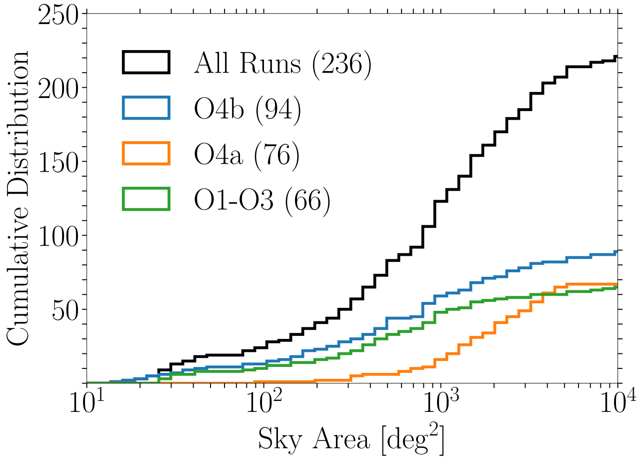

Figure 2. Cumulative distribution of the size of the 90% CR of the sky localization of CBC candidates observed during O1+O2+O3+O4a+O4b in black (236 total events including GW170817), O1-O3 in green (66 events), O4a in orange (76 events), and O4b in blue (94 events). The exclusion of Virgo in O4a greatly increased the sky localization uncertainty.

3.2. *Galaxy Catalogs*

We use two galaxy catalogs for our dark siren analysis, each with unique properties for cosmological inference. We describe them in more detail below. As the approach uses pixelation to correlate galaxy catalog information with GW localization (Gray et al. 2023), we adopt the `healpix` scheme (Górski et al. 2005; Zonca et al. 2019) with `nside` = 128 for all catalogs, chosen so that a minimum of 25 pixels are able to cover the 99.9% credible localization region of every event.

The first galaxy catalog used in this analysis is the K_s-band selection from GLADE+, exactly the same as used previously with GWTC-3.0 (Abbott et al. 2023a) and GWTC-4.0 (Abac et al. 2025b). GLADE+ (Dálya et al. 2018, 2022) is combined from six previous catalogs: the Gravitational Wave Galaxy Catalog (GWGC, White et al. 2011), HyperLEDA (Makarov et al. 2014), the 2 Micron All-Sky Survey Extended Source Catalog (2MASS XSC, Skrutskie et al. 2006), the 2MASS Photometric Redshift Catalog (2MPZ, Bilicki et al. 2014), the WISExSCOS Photometric Redshift Catalog (WISExSCOSPZ, Bilicki et al. 2016) and the Sloan Digital Sky Survey quasar catalog from the 16th data release (SDSS-DR16Q, Lyke et al. 2020). Before masking, this dataset covers almost the entire sky except for the Milky Way area, where dust and stars obscure background galaxies.

The catalog includes all galaxies in GLADE+ with measurements in the near-infrared $K_{\rm s}$-band, numbering ~ 1 million galaxies with median redshift $\langle z \rangle \sim 0.08$ and covering 37,201 deg^2. About 77% of the objects have photometric redshift estimates (photo-zs), originating mainly from 2MPZ (Bilicki et al. 2014) with a typical accuracy of $\sigma_z/(1+z) < 1.5\%$. The remaining $\sim 23\%$ of the objects have more precise spectroscopic redshifts (spec-zs) from other input datasets with errors of order $\sigma_z < 10^{-3}$. Objects with $z \leq 0.05$ were also corrected for peculiar velocities using the framework of Mukherjee et al. (2021a), relying on the Bayesian Origin Reconstruction from Galaxies (BORG) approach (Jasche & Wandelt 2013). We use a coarse `nside` = 32 to compute the magnitude threshold $m_{\rm thr}$ and normalization maps. Further details of all choices and methodology for GLADE+ K_s-BAND can be found in Sec. 3.2 of both Abbott et al. (2023a) and Abac et al. (2025b).

The second catalog we employ is the Dark Energy Survey (DES, Abbott et al. 2005) Year 6 Gold catalog (Bechtol et al. 2025), a cosmology-focused photometric survey of 4923 deg^2 in the southern sky, which gathered 669 million objects using the Dark Energy Camera (DECam) at the 4-m Blanco telescope at Cerro Tololo Inter-American Observatory in Chile. Typical photometric redshift errors for each galaxy are of the order $\sigma_z/(1+z) < 10\%$. We choose to use r-band photometry because the average photometric magnitude errors in this filter are smaller than in the other three bands (giz). The 10σ magnitude depth of the survey in r-band is 23.9. We use magnitudes which are corrected for Galactic extinction, apply photometric quality cuts, and use the XGBoost object classification score included in the catalog to mitigate stellar contamination (Chen & Guestrin 2016). The number of galaxies remaining after these quality cuts is 350 million. We use K-corrections from Chilingarian et al. (2010). Further details of all choices and methodology for using the DES Year 6 catalog can be found in McMahon et al. (2026). We adopt the measured r-band Schechter parameters from that analysis ($M_r^* = -20.9$, $\alpha = -1.01$, $M_{\rm max} = -24.29$, $M_{\rm min} = -16.33$). We use a coarse `nside` = 128 to compute the $m_{\rm thr}$ and normalization maps.

As bright nearby objects saturate in the camera CCDs, these are not present in the catalog. For this reason, we apply a low-end redshift cut at $z_{\rm min} = 0.05$ for the in-catalog part of the DES r-BAND redshift prior (Eq. 2). This cut also removes the need for peculiar velocity corrections at low redshift. At the large redshift end, we adopt a conservative cut $z_{\rm max} = 0.35$ on the in-catalog part of the prior, as this is the highest value at which the galaxy redshift distribution is consistent with the comoving volume distribution assumption within less than 1σ. The out-of-catalog term compensates for catalog incompleteness outside of the redshift cuts. For our faint-end Schechter absolute magnitude limit of $M_{\rm min} = -16.33$ and average apparent magnitude threshold $m_{\rm thr} = 23.8$, DES r-BAND is 99.9% complete at $z = 0.35$.

A summary of the characteristics of the galaxy catalogs is given in Table 1. The left-hand side panels of Figure 3 present the catalog footprints, overlaid with the sky localizations of the twenty best-localized GWTC-5.0 events included in our analysis. These GW events have

Galaxy Catalog	Sky Coverage [deg^2]	Num. of Galaxies	$z_{\rm med}$	$\frac{\sigma_z}{1+z}_{\rm med}$	$f_{\rm cov,all}$	$f_{\rm cov,20}$
GLADE+ K_s-BAND	37201	9.9×10^5	0.08	0.014	5%	23%
DES r-BAND	5169	3.5×10^8	0.85	0.096	7%	17%

Table 1. Summary and comparison of the galaxy redshift catalogs used in this analysis after all relevant cuts have been applied. Here, $f_{\rm cov,all}$ and $f_{\rm cov,20}$ the percentage of localization volume of all GW events and the twenty events with the smallest volume, respectively (see Eq. B.1).

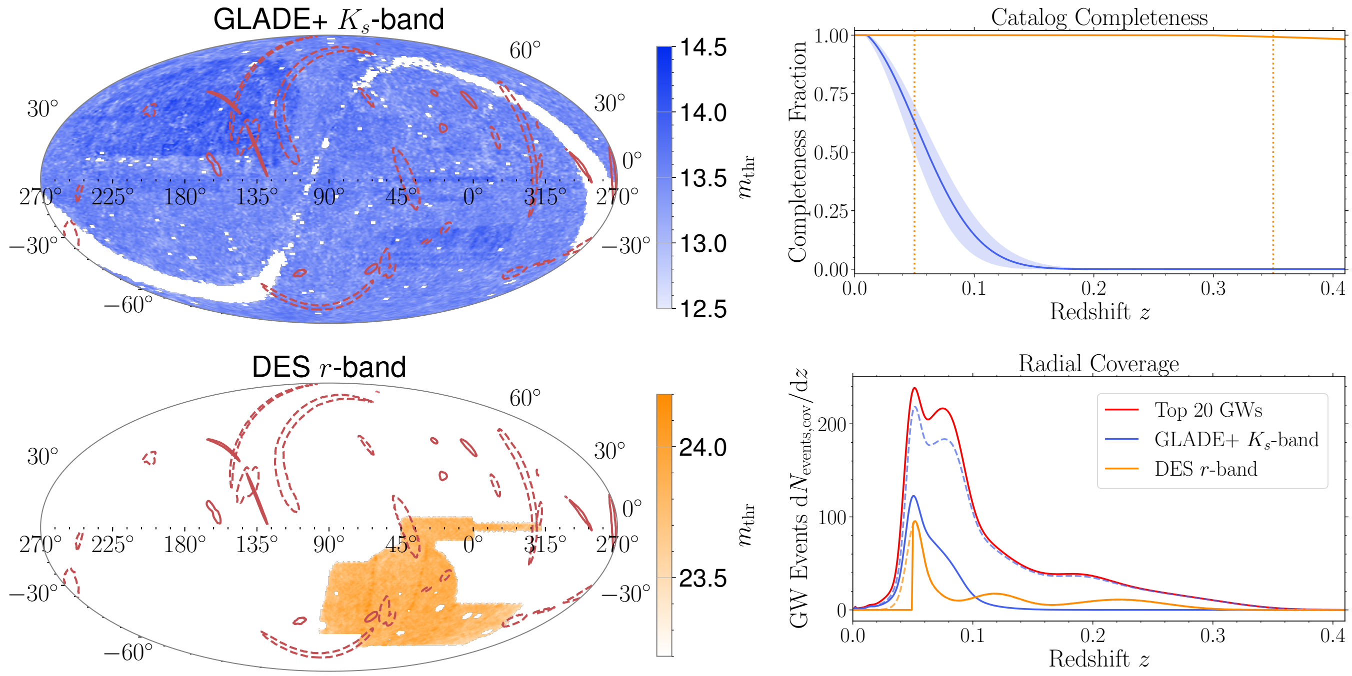

Figure 3. Left column: survey footprints of the GLADE+ K_s-BAND (top) and DES r-BAND (bottom) galaxy catalogs. Contours of the 90% credible areas for the twenty GW events with the smallest localization volume are overlaid in red. O4b (pre-O4b) events are shown with solid (dashed) contours. Right column: (top) The completeness fraction as a function of redshift of each catalog as defined as the difference between a uniform in comoving volume distribution of galaxies and the out-of-catalog term defined in Section 2.2. The completeness fraction computed with the median magnitude threshold $m_{\rm thr}$ over all pixels is shown with solid lines, with 1σ credible regions overlaid. The redshift cuts of $z_{\rm min} = 0.05$ and $z_{\rm max} = 0.35$ on the in-catalog term used for DES r-BAND are shown with dotted lines (GLADE+ K_s-BAND does not cut on redshift). (Bottom) Radial coverage of both catalogs (blue and orange) with respect to the skymaps of the twenty GW events with the smallest localization volume (red). The dashed lines correspond to the overlap of areas between the events and the catalogs, and the solid lines correspond to the overlap of volumes (see Appendix B).

the smallest overlap with possible potential host galaxies and therefore are expected to be the most cosmologically informative. We propose a useful statistic, $f_{\rm cov}$, for the GW coverage of each of the catalogs, defined as the percentage of the total localization volume of the GW events that overlap with the three-dimensional completeness fraction of the catalog. Further details about the derivation of $f_{\rm cov}$ can be found in Appendix B.

The redshift distribution of the twenty best-localized events and their overlap with the catalogs is shown in the right-hand side panel of Fig. 3. While the majority of the GW sample distribution is not covered by either catalog, the best-localized events are better covered by both catalogs compared to the rest of the events (see Table 1). While GLADE+ K_s-BAND is wide and shallow in coverage and DES r-BAND is comparatively narrow and deep, they both cover a similar fraction of the GW distribution and therefore are expected to provide similar constraints on H_0.

4. RESULTS

In this section, we present our cosmological results based on the spectral and dark siren analyses, which deliver joint inference of cosmological and population hyperparameters. These include parameters that describe the assumed mass and spin distributions, and merger rate models, as well as different parametrizations for deviations of GR on cosmological scales. For the H_0 results, we will also combine our dark siren constraints with those from the bright siren GW170817, similarly to the analysis presented by Abac et al. (2025b).

We sample the posterior in Equation (1) with the normalizing-flows-enhanced nested-sampling package `nessai` (Williams et al. 2021; Williams 2021) via the `bilby` package (Ashton et al. 2019). For spectral siren analyses we present combined results from `icarogw` and `gwcosmo` as posterior distributions built from an equal-weighted mixture of samples (50% from each pipeline), except for the analyses considering alternative spin parametrizations, and modified gravitational wave propagation results, which rely on `icarogw` samples only. For dark siren analyses our results are instead based solely on posterior distributions obtained with `gwcosmo`.

Section 4.1 focuses on the measurement of H_0 in a flat-ΛCDM model, obtained with either spectral sirens or dark sirens with galaxy catalog data from GLADE+ K_s-BAND or DES r-BAND, as well as exploring the impact of a number of modeling assumptions. Section 4.2 presents constraints on modified GW propagation. When quoting results, we report the median value plus its 68% symmetric credible interval (CI). We use the relative decrease in average uncertainty, computed from the 68% CI, as a metric to measure the improvement of our results.

4.1. *ΛCDM Cosmology*

Table 2 reports the Bayes factors obtained by fitting the data with different population and galaxy catalog model assumptions, assuming a flat-ΛCDM cosmology. These Bayes factors are computed using the evidence from each nested sampling process, which is a direct product of the hierarchical inference.

According to this table, the spectral siren analyses show a mild preference for the FULLPOP 3 PEAKS mass model over the FULLPOP-4.0. Despite this, we choose to adopt the FULLPOP-4.0 as our fiducial model in the rest of our analyses, as this means our analyses are more directly comparable to those in Abac et al. (2025b), which also used the FULLPOP-4.0 mass model as a fiducial choice. The inclusion of galaxy catalog information yields marginally worse Bayes factors with the FULLPOP-4.0, except in the case of GLADE+ K_s-BAND with $\epsilon = 0$. In the case of the FULLPOP 3 PEAKS model, the inclusion of galaxy catalog information is mildly disfavored relative to the FULLPOP 3 PEAKS spectral analysis in all cases and with both catalogs. However, an important consideration for inclusion of galaxy catalog Bayes factors is that a number of choices, such as those detailed in Section 3.2, are made in the construction of the galaxy catalog prior which may impact the overall Bayes factors. In effect, we are not just comparing the inclusion of galaxy catalog information against the spectral result, but also the specific choices made in the construction of the galaxy catalog prior.

When considering only BBHs - which we parametrize with the MLTP mass model - we compare spin models. The preferred spin distribution is the TRANSITION model, which is favored significantly over the GAUSSIAN spin model. However, since the scope of the TRANSITION and GAUSSIAN models is restricted to BBHs, we do not use these spin models as fiducial models, as the fiducial analyses assume the FULLPOP-4.0 and FULLPOP 3 PEAKS mass models that probe the mass distribution of the full population of CBCs.

In the following, we choose as our fiducial model the FULLPOP-4.0 mass distribution, augmented by the DES r-BAND galaxy catalog using $\epsilon = 1$ luminosity weights to infer cosmological parameters. We justify this choice as no catalog is significantly favored or disfavored by the data, and we see a clear improvement in the H_0 constraint when including the DES r-BAND catalog with luminosity weighting over the other catalog.

Figure 4 presents the marginalized posterior distributions of the Hubble constant for the different standard siren methodologies, assuming our fiducial model for spectral and dark siren analyses. When combined with the posteriors of the bright siren result of GW170817, we find $H_0 = 71.0^{+9.0}_{-7.1}\,\mathrm{km\,s^{-1}\,Mpc^{-1}}$. Spectral and dark siren constraints alone, i.e. when not combined with GW170817, provide $H_0 = 70.1^{+15.1}_{-13.3}\,\mathrm{km\,s^{-1}\,Mpc^{-1}}$ and $H_0 = 67.6^{+13.6}_{-12.7}\,\mathrm{km\,s^{-1}\,Mpc^{-1}}$, respectively. These constraints are now tighter than the constraint obtained with the only confidently identified bright siren available, namely GW170817, which gives $H_0 = 79.1^{+27.6}_{-12.4}\,\mathrm{km\,s^{-1}\,Mpc^{-1}}$ (Figure 4, yellow curve). In particular, the dark sirens analysis excludes the tail of high H_0 values present in the bright siren result. We compute our GW170817 posterior analogously to Abac et al. (2025b), by taking the inferred parameters of a spectral siren run with the fiducial FULLPOP-4.0 mass model and using these as fixed in order to perform a bright siren analysis.

With the current set of data, the main driver of the Hubble constant measurement remains the presence of features in the mass distribution. We assess this by comparing the case where galaxy-catalog information is not included and constraints on H_0 are solely driven by our population assumptions, which corresponds to the spectral siren result (Figure 4, orange curve), to our fiducial dark siren scenario (Figure 4, blue curve). From Figure 4 we see an improvement of 7.4% in the H_0 constraint when including the DES r-band galaxy catalog information compared to the spectral siren result. The spectral siren analysis is further discussed in Appendix D.

Figure 5 summarizes our findings alongside previous measurements from the LVK. We adopt the

Mass Models & Luminosity Weighting						Spin Models	
		GLADE+ K_s-BAND		DES r-BAND			
Mass Model	**Spectral**	$\epsilon = 0$	$\epsilon = 1$	$\epsilon = 0$	$\epsilon = 1$	**Spin Model**	
FullPop-4.0	0.00 ± 0.14	0.26 ± 0.10	-0.22 ± 0.10	-0.08 ± 0.10	-0.18 ± 0.10	Gaussian	0.00 ± 0.15
FullPop 3 Peaks	0.61 ± 0.14	0.24 ± 0.10	0.23 ± 0.10	0.37 ± 0.10	0.05 ± 0.10	Transition	3.16 ± 0.10

Table 2. Bayesian evidence comparison: logarithmic Bayes factors (BF) using base-10 logarithms for different mass and spin population models, as well as galaxy catalog choices. The mass model and luminosity weighting comparison (left) is restricted to full CBC models only (i.e. excluding the MLTP mass model) and all values are relative to the FullPop-4.0 model with no catalog information (i.e. spectral), while the spin model comparison (right) assumes a MLTP spectral analysis, normalizing the spin model BFs to the Gaussian model. In all cases a positive value indicates a preference for a given model over the reference model. The full CBC models used in the mass model and luminosity weighting columns implicitly assume a uniform spin distribution. Overall for the mass and galaxy catalog comparison, the FullPop 3 Peaks spectral analysis is the most preferred, while for the spin model comparison the Transition model is preferred over the Gaussian one.

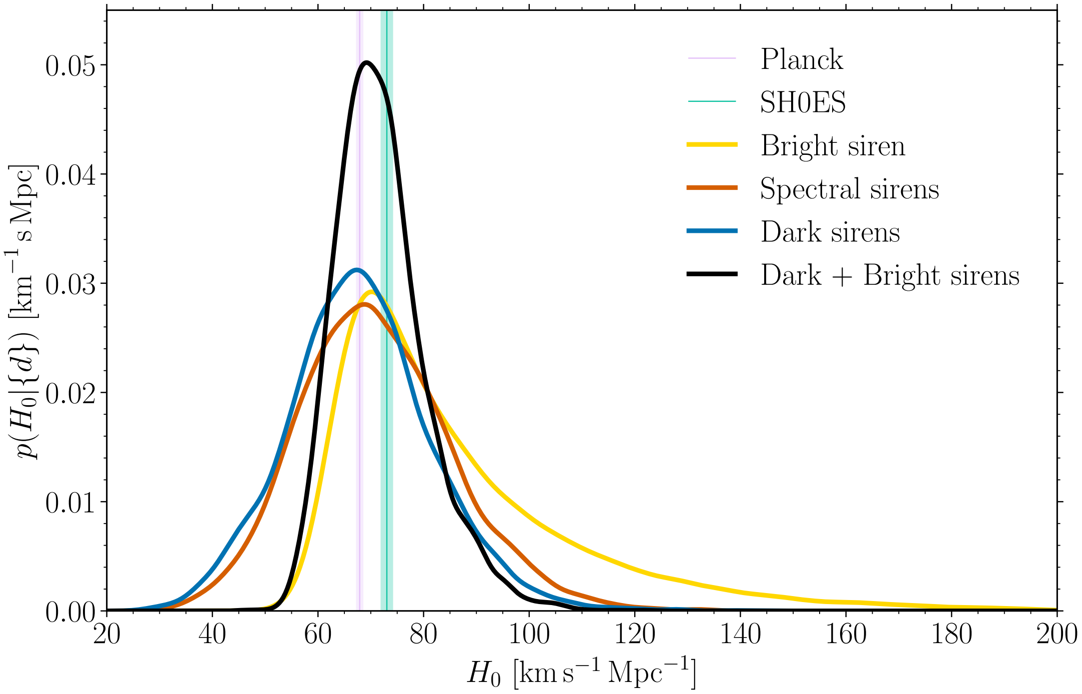

Figure 4. Hubble constant posterior for different cases. Yellow curve: posterior obtained from the bright siren GW170817 and its EM counterpart. Orange curve: posterior obtained with the spectral siren method and the FullPop-4.0 mass model. Blue curve: posterior obtained using all dark sirens with DES r-band in the luminosity-weighting case ($\epsilon = 1$) and spectral siren information from the FullPop-4.0 mass model. Black curve: posterior after combining the dark and bright siren results. The pink and green shaded areas identify the 68% CI constraints on H_0 inferred from CMB anisotropies (Ade et al. 2016) and in the local Universe from SH0ES (Riess et al. 2022), respectively. Our fiducial result using both bright and dark sirens produced a constraint of $H_0 = 71.0^{+9.0}_{-7.1}$ km s^{-1} Mpc^{-1}, while the spectral and dark analyses produced constraints of $H_0 = 70.1^{+15.1}_{-13.3}$ km s^{-1} Mpc^{-1} and $H_0 = 67.6^{+13.6}_{-12.7}$ km s^{-1} Mpc^{-1}, respectively.

same methodology used in the previous LVK measurement (Abac et al. 2025b), fully marginalizing over the CBC mass distribution and merger rate parameters. This approach is more statistically robust than assuming fixed population parameters, but complicates direct comparison with previous studies which constrain H_0 with standard sirens.

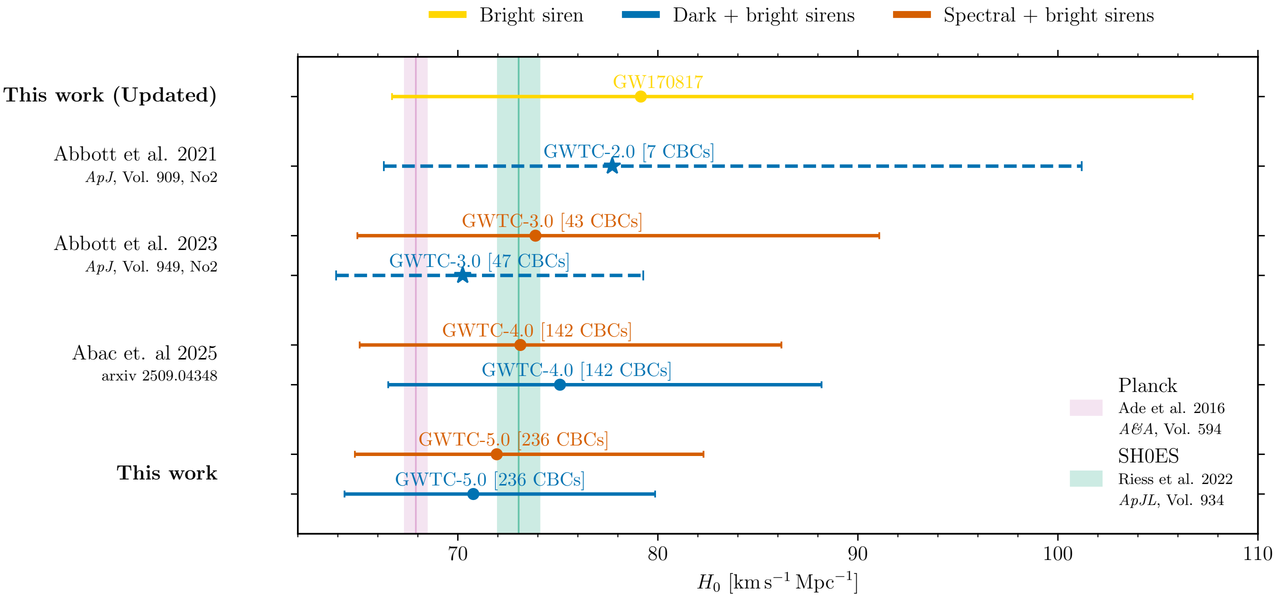

Figure 5. Summary of H_0 measurements from GW detections, combining bright with dark or spectral siren analyses conducted by LVK pipelines from O1 up to O4b. In yellow, we report the bright siren result that was recalculated in O4a and combined with the results from O4a and this analysis. All other previous combined results use the bright siren samples from Abbott et al. (2021a). We report the dark siren results in blue and spectral siren results in orange, including the bright siren in both cases. The capped errorbar covers the symmetric 68.3% CI. Studies that assumed a fixed population model are marked with a dashed line style, and a star as a marker for the median value. The total number of CBC events used in the analysis is indicated in square brackets on top of each result. For details on the analysis settings, see the respective publications. The pink and green vertical bands indicate the Planck (Ade et al. 2016) and SH0ES (Riess et al. 2022) median and 1σ values, respectively. The error bars obtained in this work are based on our fiducial mass model FullPop-4.0.

ΛCDM – Dark sirens			
Population model	GW candidates	H_0 (Dark sirens) [km s^{-1} Mpc^{-1}]	H_0 (Dark + bright sirens) [km s^{-1} Mpc^{-1}]
Multi Peak	231	$69.6^{+19.3}_{-16.1}$ ($69.6^{+34.2}_{-25.6}$)	$72.7^{+11.7}_{-8.4}$ ($72.7^{+22.0}_{-12.5}$)
FullPop-4.0	235	$67.6^{+13.6}_{-12.7}$ ($67.6^{+24.0}_{-21.8}$)	$71.0^{+9.0}_{-7.1}$ ($71.0^{+17.2}_{-11.0}$)
FullPop 3 Peaks	235	$70.6^{+12.7}_{-11.3}$ ($70.6^{+22.5}_{-19.1}$)	$72.0^{+8.8}_{-7.3}$ ($72.0^{+16.9}_{-11.1}$)

Table 3. Constraints on the Hubble constant obtained in this work under the ΛCDM cosmological model, assuming a uniform prior $H_0 \in \mathrm{U}(10, 200)\,\mathrm{km\,s^{-1}\,Mpc^{-1}}$. The first column lists the mass model adopted in the analysis. The second column gives the number of GW events included in the dark-siren analysis. The third column reports the H_0 measurement obtained using only dark sirens and the fiducial DES r-band galaxy catalog with luminosity weighting, quoted as the median together with the symmetric 68.3% and 90% CIs, with the latter in parentheses. The fourth column shows the corresponding constraints after combining the dark-siren analysis with the bright-siren posterior of GW170817.

In Table 3 and Figure 6 we illustrate the impact of population models, both mass and spin distributions, and galaxy weighting on the marginalized posteriors of H_0. All curves in the top (bottom) panels of Figure 6 are from spectral (dark) siren analyses, while the event GW170817 is excluded from the dark and spectral siren inferences, as it is treated solely as a bright siren in this paper (this choice is validated and discussed in detail in Section 5.2). The top-left panel of Figure 6 presents results based on the three different source mass models in the galaxy luminosity-weighting case: the MLTP, the FullPop-4.0 and the FullPop 3 Peaks models. The top-right panel shows the impact of spin modeling between an implicit uniform spin-magnitude prior, the Gaussian spin model and the Transition spin model. The bottom panels explore the difference between the no-weighting (right) and luminosity-weighting (left) cases for the galaxy catalogs considered in our analysis, namely GLADE+ K_s-band and DES r-band (cf. Section 3.2), while keeping the source mass model fixed to our fiducial mass model FullPop-4.0.

From the top-left panel of Figure 6, we find some differences in the measurements of H_0 due to assumptions about the shape of the mass spectrum. The MLTP model provides a broader posterior with respect to the other two mass models as it cannot properly account for all the substructures of the mass function which appear preferred by the data (see Table 2). The FullPop 3 Peaks model instead shows a very mild preference for higher H_0 values. Such a behavior is connected to the appearance of an additional reconstructed feature in the FullPop 3 Peaks mass distribution with respect to the FullPop-4.0 one. The Hubble constant is strongly degenerate with population parameters determining the position of sharp features in the mass function. As a consequence, a shift of the inferred value of H_0 can lead to a shift of the value of some of these parameters, in particular the position of features and the low and high end cuts of the mass functions. A mass model will compensate for any missing features by adjusting the other parameters of the model. If the inferred source frame distribution has a dearth of higher black hole masses, the analysis will compensate by adjusting the redshifts of the sources upwards, and hence shift the recovered H_0 to higher values. As shown in the left panel of Figure 8 in the Appendix, the FullPop 3 Peaks shifts the inferred minimum and maximum masses of the mass function, thus affecting the retrieved value of H_0.

The top-right panel of Figure 6 shows that there are almost negligible differences on the inference of H_0 between the two spin models, with the Gaussian model producing a constraint of $H_0 = 72.4^{+22.5}_{-18.3}\,\mathrm{km\,s^{-1}\,Mpc^{-1}}$, while the Transition model prefers slightly lower values, $H_0 = 67.0^{+21.9}_{-17.6}\,\mathrm{km\,s^{-1}\,Mpc^{-1}}$. However, the Gaussian model is strongly disfavored by the data when compared to the Transition model (see Table 2). In contrast with our other analyses, the spin results are evaluated using a threshold on the log-likelihood variance of < 1, rather than a cut on the effective number of posterior samples. This is a more robust threshold for analyses including spin parameters, as discussed in Talbot & Golomb (2023) and Abac et al. (2025b).

The bottom panels of Figure 6 show the effect of the choice of different luminosity weights—either $\epsilon = 0$ or $\epsilon = 1$ (see Equation (3)), which is demonstrated for both galaxy catalogs considered. The two choices of luminosity weighting balance computational cost and avoid inaccuracies that may arise when large choices of ϵ cause a very small number of the most luminous galaxies to dominate enough to cause numerical precision issues in the evaluation of the likelihood. Although fixing these weights introduces a potential systematic uncertainty (Perna et al. 2024; Hanselman et al. 2025), the results for the no-weighting and luminosity-weighting cases are in good agreement, with differences well within statistical error. The ability to constrain luminosity weights would be of astrophysical value, but we find no strong evidence based on Bayes factors to favor uniform weighting over luminosity-based weighting (see Table 2). This outcome reflects the relatively limited impact of the galaxy catalogs on the inference with the datasets used here. The bottom panels of Figure 6 indicate that although small differences appear between the use of different galaxy catalogs, the resulting H_0 posteriors are still in agreement with one another. We expect that these differences will become significant with larger datasets and better-localized events, in which case marginalizing over the weighting power-law index may be more robust.

The inclusion of GLADE+ K_s-band information improves over the spectral siren constraints on the Hubble constant by approximately 4.2%, while the inclusion of DES r-band information provides a 7.4% improvement.

All constraints obtained in this section assume a fixed value of $\Omega_\mathrm{m} = 0.3065$ as well as a fixed dark energy equation-of-state parameter $w_0 = -1$. Inferring the values of these parameters independently is not possible at present using our dark siren methods, due to the computational cost of constructing redshift priors with varying Ω_m and w_0. However, in Appendix E we performed a spectral siren analysis with varying Ω_m and w_0 and found that the posterior distributions of these parameters are consistent with the priors, due to the limited constraining power of our data at high redshift, while the uncertainties on other parameters of interest are only marginally affected. This confirms that allowing these parameters to vary does not influence our main results.

4.2. *Modified Gravity*

In this section we present the results obtained by introducing parameterized deviations from GR that affect the luminosity distance ratio, $D_\mathrm{L}^\mathrm{GW}/D_\mathrm{L}^\mathrm{EM}$, as described in Section 2.4.2. The analysis is carried out using our fiducial mass model (FullPop-4.0 spectral siren analysis without explicitly modeling the spin distribution, equivalent to a uniform prior on the spin magnitudes).[3]

For each modified gravity (MG) model, we consider two different uniform priors for the Hubble constant: a wide prior, $H_0 \in \mathrm{U}(10, 120)\ \mathrm{km\,s^{-1}\,Mpc^{-1}}$, and a narrow prior, $H_0 \in \mathrm{U}(65, 77)\ \mathrm{km\,s^{-1}\,Mpc^{-1}}$. This choice is motivated by the following considerations. In general, H_0 and any parameter governing modified GW propagation are correlated to some extent, as both affect the luminosity distance–redshift relation. Consequently, the most agnostic approach to constraining deviations

---

[3] At a late stage in the preparation of this work, we discovered an issue in the robustness of the dark siren results for the MG analysis. Therefore, we solely use the spectral siren analysis when constraining the MG parameters, differing from Abac et al. (2025b) where the dark siren method was applied.

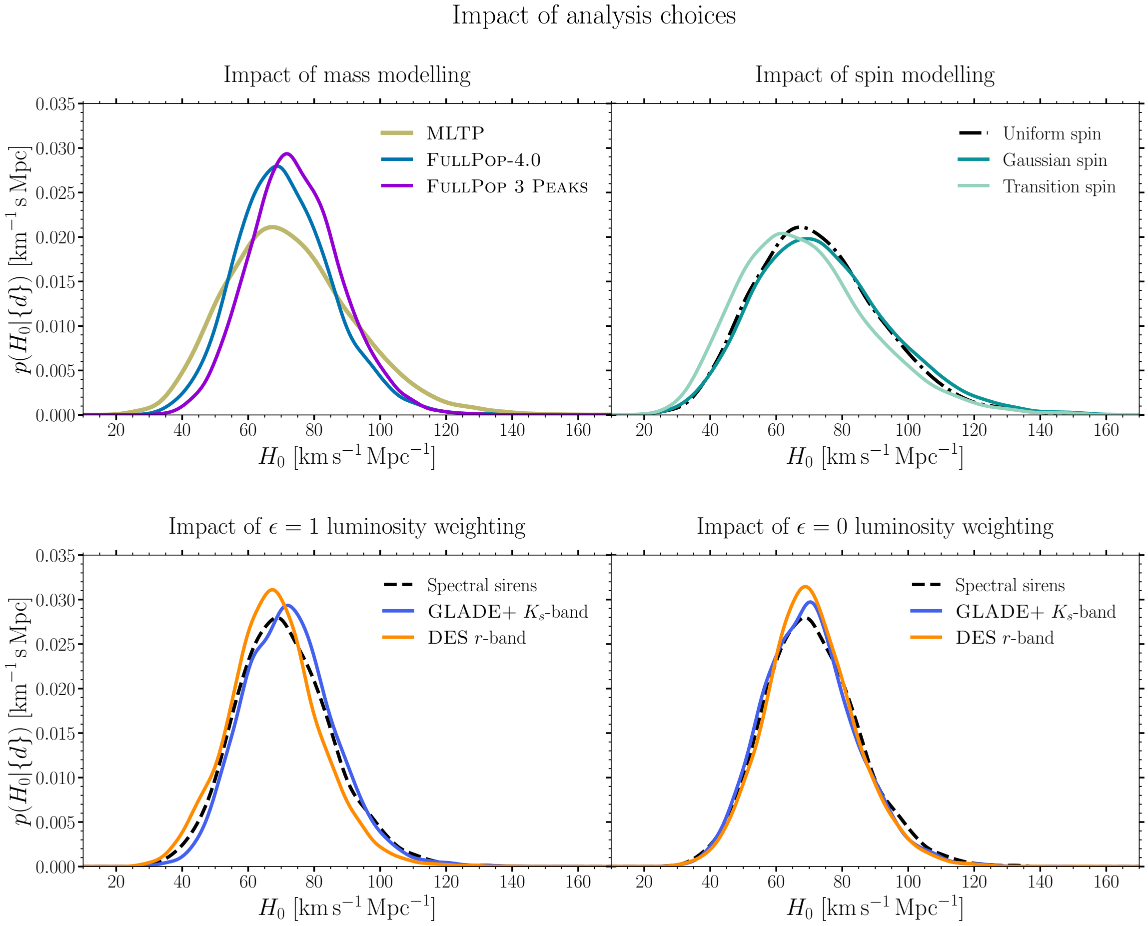

Figure 6. Left top panel: Hubble constant posteriors with the spectral siren method, assuming three different mass models, one BBHs-only and two for all CBCs. See Section 2.3 and Appendix A for definitions of these models. Right top panel: Hubble constant posteriors comparing the effects of two different assumed spin models, compared to a case where no spin information is taken into account. All analyses in this panel assume the MLTP mass model and are BBHs-only. Left bottom panel: Hubble constant posteriors for dark siren analysis with two different galaxy catalogs, assuming that host weighting is proportional to luminosity. The bottom two panels both assume the FullPop-4.0 mass model. Right bottom panel: Hubble constant posteriors for dark siren analysis with different galaxy catalogs, assuming that host weighting is uniform with respect to luminosity.

from GR involves marginalizing over H_0 using a broad enough prior—hence the adoption of the wider range. The broad prior adopted for H_0 in this section is narrower than the one used for the ΛCDM case. This is because, for certain extreme combinations of H_0 and Ξ_0, a wider prior on H_0 would lead to assigning very high redshifts—beyond $z \gtrsim 10$—to the GW sources in the sample. Our redshift priors, by construction, do not cover these redshifts as we assume this case to be highly improbable. Furthermore, this would cause instability in our treatment of selection effects because at these very high redshifts the stability criterion for Monte Carlo (MC) integration could fail (see Appendix A of Abac et al. (2025b)). To avoid these issues, we restrict the H_0 prior accordingly. Conversely, it is also valuable to explore constraints on GR under the assumption of prior knowledge of other cosmological parameters, which motivates our second choice of a narrower prior which encompasses the region of the current Hubble tension at approximately 4σ (Aghanim et al. 2020; Riess et al. 2022; Di Valentino & Brout 2024).

First, we discuss results for the MG parametrizations, see Equations (11), (12) and (13). The uniform priors used in the Ξ_0–n analysis are $\Xi_0 \in \mathrm{U}(0.435, 10)$ and $n \in \mathrm{U}(0.1, 10)$. Adopting a wide H_0-prior, we find $\Xi_0 = 1.1^{+0.6}_{-0.3}$, while with the narrow H_0-prior we obtain $\Xi_0 = 1.0^{+0.3}_{-0.2}$. This result is consistent with GR, recovered in the limit $\Xi_0 = 1$.

For the α_M parametrization we use the prior $c_M \in \mathrm{U}(-2.95, 10)$. We find $c_M = -0.4^{+1.6}_{-1.3}$ with a wide H_0-prior, and $c_M = -0.1^{+1.0}_{-0.8}$ with a narrow H_0-prior. This is also consistent with GR, recovered in the limit

$c_M = 0$. In the case of both the wide and narrow H_0 priors, we find that additionally inferring MG parameters slightly worsens the constraints on H_0 with respect to the ΛCDM case, as expected due to the correlation between H_0 and MG parameters.

Both MG analyses display a strong correlation between the parameters describing deviations from GR and the merger rate model parameter γ (see Equation A.2), consistent with the findings of Mancarella et al. (2022); Leyde et al. (2022); Chen et al. (2024a). This correlation can be seen in Figure 13 of Appendix F. The correlation occurs because the MG parameters modify the relationship between $D_{\rm L}^{\rm GW}$ and z, therefore affecting the observability of GW sources as a function of redshift. A similar change could be reproduced by adjusting the merger rate of CBCs as a function of redshift, which is what γ controls, leading to degeneracy.

Figure 7 presents the reconstructed relation between redshift and GW luminosity distance ratio $D_{\rm L}^{\rm GW}/D_{\rm L}^{\rm EM}$ for the two modified gravity models, obtained with our fiducial dark siren analysis. The reconstructions for each analysis are derived from their respective posterior distributions provided in Appendix F. In GR, the distance ratio plotted in Figure 7 is always one. The slight asymmetry of the contours around $D_{\rm L}^{\rm GW}/D_{\rm L}^{\rm EM} = 1$ is inherited from the asymmetry of the marginalized posteriors on Ξ_0 and c_M visible in Figure 13. The additional right-hand y-axis for the α_M results enables their interpretation in terms of an effective gravitational coupling that can be derived from GW propagation (see Section 2.4.2). At low redshifts our results correspond to a few percent constraint on the ratio of this coupling at the source and the observer; the constraints inflate to order unity at $z \sim 1$ due to the lack of events at higher redshifts.

5. DISCUSSION AND PERSPECTIVES

In this section, we compare our results to the literature, and discuss possible improvements and future developments which constitute negligible systematics at present.

5.1. *Comparison with Existing Results*

We begin by discussing our constraints on the Hubble constant. All our results remain statistically consistent with the values reported by the Planck (Ade et al. 2016; Aghanim et al. 2020) and SH0ES (Riess et al. 2021, 2022) collaborations at the 68% CI. Our new spectral siren measurement yields a 14.6% improvement with respect to Abac et al. (2025b), driven by the increased number of events. Including our best dark siren result from the galaxy catalogs, we find a 25.7% improvement from O4a when using the DES r-BAND catalog. For comparison, the GLADE+ K_s-BAND dark siren constraint shows an improvement of 18.3% from O4a.

We also report constraints on GW propagation parameters for GWTC-5.0 with the FULLPOP-4.0 mass model, which is comparable with the results from Abac et al. (2025b). Our new measurement yields a 35.7% improvement in Ξ_0 over GWTC-4.0 with a wide H_0 prior, and a 50% improvement in constraint with a narrow H_0 prior. We find a 27.5% improvement for c_M compared to O4a with a wide H_0 prior and a 45.5% improvement with a narrow H_0 prior. Previously, modified gravity parameters were also constrained using GWTC-2.0 (Ezquiaga 2021) and GWTC-3.0 (Mancarella et al. 2022; Leyde et al. 2022; Mastrogiovanni et al. 2023; Chen et al. 2024a).

Assuming α_M is sourced by a scalar degree of freedom within the effective field theory (EFT) framework, and in the class of Horndeski-type theories, our constraints from GW observations can be compared to those from LSS and the CMB. When analyzing LSS and CMB data, it is essential to ensure that the scalar sector remains free from ghost and gradient instabilities. These theoretical consistency requirements further restrict the allowed parameter space. Recent LSS analyses that assume luminal tensor propagation (Noller & Nicola 2019; Baker & Harrison 2021; Seraille et al. 2024; Ishak et al. 2024) impose such constraints. In a GW-only analysis, we assume that stability can be enforced by appropriate choices of additional EFT operators—particularly the braiding parameter α_B—which influence only the scalar sector. For theories with $\alpha_B = 0$, regions with $\alpha_M < 0$ are typically ruled out by stability arguments.

The latest available LSS bounds correspond to the clustering measurements from DESI 2024 (Ishak et al. 2024). This work finds the bound $c_M < 1.14$ (95% CI), assuming vanishing braiding and a ΛCDM background. Relaxing the braiding assumption and marginalizing over it yields a constraint of $c_M = 1.05 \pm 0.96$ at 68% CI. More stringent constraints can be obtained by combining different LSS observables. In particular, the integrated Sachs–Wolfe (ISW) effect from galaxy–CMB cross-correlations has been shown to provide significant improvements (Renk et al. 2017; Seraille et al. 2024). Combining LSS and CMB observables to ISW, Seraille et al. (2024) find $c_M = 0.54^{+0.90}_{-0.60}$ at 95% CI after marginalization over the braiding parameter. While consistent with these bounds, our best result is approximately ∼6% stronger and ∼20% weaker relative to the latter two, respectively. Despite this, our results are based on an entirely independent dataset with different systematics.

5.2. *Perspectives*

Considerations on the Spectral Siren Analysis—Spectral siren information is dependent on the shape of the mass distribution of compact objects, and thus can be sensitive to choices of priors for the hyperparameters. We do not change our priors from previous studies (Abbott et al. 2023a,c; Abac et al. 2025b). Even if the analytical formulation of the underlying mass model is the same, significantly extending the prior range of the population parameters could alter the reconstructed mass

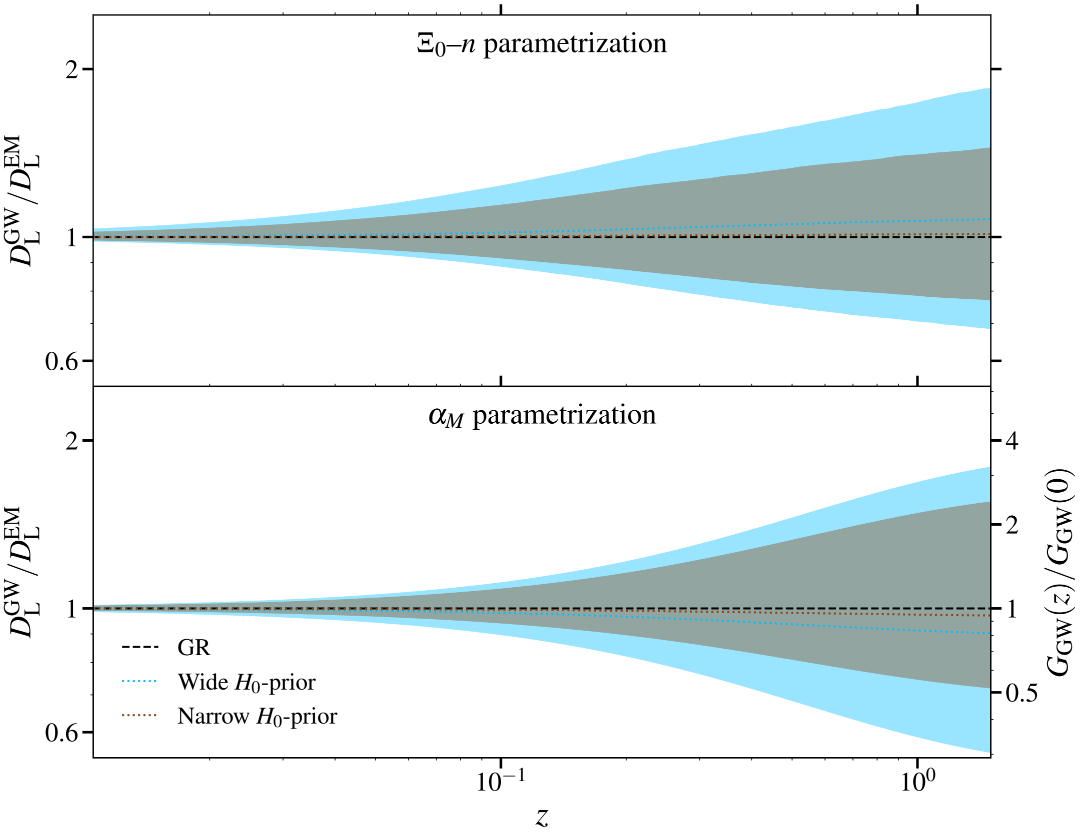

Figure 7. Reconstructed ratio D_L^{GW}/D_L^{EM} as a function of cosmological redshift z, for the two modified gravity parametrizations considered, Ξ_0–n and α_M. The blue (brown) bands indicate wide and narrow H_0-prior results, respectively (see Table 4 for details). In all cases the contours show the 90% CI with median (dotted curve) reconstructed from spectral siren analyses with the FullPop-4.0 mass model. The black dashed curve represents the GR limit. Note that the reconstructed distance ratio is asymmetric at higher redshifts. The additional righthand y-axis on the lower panel converts the constraints on the α_M parametrization into an effective gravitational coupling, which is discussed in section 2.4.2 and Appendix F. This interpretation is not applicable to the $\Xi_0 - n$ parametrization.

spectra (Gennari et al. 2025). We do not consider this possibility here.

The choice of mass model formulation and corresponding priors alters the resulting cosmological constraints. Using a mass model which includes all CBCs improves the H_0 constraint due to the additional mass features in the FullPop-4.0 and FullPop 3 Peaks models when compared to the BBH-only MLTP model. From Table 2, we find a slight preference for the FullPop 3 Peaks model, however we continue to use the FullPop-4.0 model for our fiducial result, so our results remain comparable to those in Abac et al. (2025b).

We consider the impact of modeling mass–spin evolution (Abac et al. 2026e; Biscoveanu et al. 2022; Li et al. 2024b,a; Pierra et al. 2024a; Tong et al. 2025). While this analysis is performed only for the MLTP model, we find that including spin information increases the H_0 uncertainty by 8.8% and 5.3% for the Gaussian and Transition models, respectively, relative to the default spectral MLTP analysis. Additionally, we find that the Transition model is significantly favored by Bayes factor ($\log_{10}\mathcal{B} = 3.16 \pm 0.10$) relative to the Gaussian model, motivating the inclusion of more complex spin modeling in the future.

Similarly, while current data do not robustly support evolution of the mass distribution with redshift (Heinzel et al. 2025; Lalleman et al. 2025; Gennari et al. 2025; Abac et al. 2026e), considering this effect may become important as GW detector sensitivity improves. Such evolution could introduce biases if not properly modeled (Pierra et al. 2024b; Agarwal et al. 2025; Roy et al. 2025). Nevertheless, because cosmological effects imprint a coherent and predictable modulation on the mass spectrum observed across different redshifts, it is expected that appropriate modeling should allow disentanglement of these from astrophysical evolution (Ezquiaga & Holz 2022; Chen et al. 2024b; Mali & Essick 2025a). In future studies, it would be valuable to incorporate comprehensive correlation modeling or adopt data-driven approaches (Farah et al. 2025), which offer increased flexibility and robustness by reconstructing features directly from the observations, without strong parametric assumptions.

Combination with Bright Sirens—When combining dark siren events with bright sirens such as GW170817, particularly within a sample that includes both BNS mergers with and without EM counterparts, the correct approach would be to model the joint GW and EM detection probabilities and perform a unified hierarchical inference. At present, while our pipelines fully account for GW selection effects, they do not yet model the EM detection probability (potential systematics related to EM selection effects, and related mitigation strategies, can be found in Chen 2020; Chen et al. 2024c; Mancarella et al. 2024; Müller et al. 2024; Salvarese & Chen 2024). Consequently, we exclude GW170817 from the dark siren inference and instead combine its posterior with that of the dark sirens a posteriori. Abac et al. (2025b) verified that this choice does not introduce any bias in the inferred mass spectrum. This effect will need to be included in expectation of more bright siren events.

Considerations on the Analysis with Galaxy Catalogs—Our reported results suggest that the information gained from galaxy catalogs is subdominant to spectral siren constraints. Many of the events which have significant overlap with either galaxy catalog contain $\mathcal{O}(10^{3-5})$ galaxies within their volume (See Table 12). Improvements to the GW detector sensitivity will improve the distance precision and future spectroscopic surveys will improve the galaxy redshift precision, both of which will have a large impact on the constraint from galaxy catalog dark sirens (Borghi et al. 2024; Cross-Parkin et al. 2025).

Our galaxy catalogs have different optical filters and unique systematic considerations (see Section 3.2). We model the expected number density with a redshift-independent Schechter function and assume that missing galaxies are uniformly distributed in comoving volume and isotropically in sky position. While the latter is the most conservative choice, viable alternative assumptions include having them trace the distribution of cataloged galaxies (Finke et al. 2021a) or follow prior knowledge of large-scale structure (Dalang & Baker 2024; Leyde et al. 2024; Dalang et al. 2024; Leyde et al. 2025). With deeper catalogs such as DES r-BAND, redshift evolution of the Schechter function may have an effect on the expected number of galaxies, but we do not model this effect in this analysis.

Furthermore, in this work, we model the uncertainty on galaxy redshift using a Gaussian distribution. However, this assumption likely represents an oversimplification, as photometric redshift error distributions can be more complex and even vary on a galaxy-by-galaxy basis. More comprehensive approaches, such as the use of full photo-z PDFs, have been explored in the literature (e.g., Palmese et al. 2020; Bom et al. 2024; Alfradique et al. 2024, 2026). Redshift uncertainties can propagate into derived quantities that depend on redshift, such as K-corrections and absolute magnitudes (or luminosities). Turski et al. (2023) investigated two common error models (Gaussian and modified Lorentzian) and found that, under current levels of uncertainty, the choice of redshift error model does not significantly affect constraints on the Hubble constant. Nonetheless, this conclusion may not hold as future catalogs become more complete and systematic uncertainties are reduced, potentially making the choice of redshift uncertainty model more consequential.

Additionally, both catalogs present unique assumptions and challenges which have a large effect on the resulting measurement. GLADE+ K_s-BAND is a combination of independent catalogs from different instruments and incongruent magnitude limits, mixing photometric and spectroscopic redshifts. The effect of combining catalogs in this way is not yet fully understood. Further issues can arise if the galaxy catalog deviates from the given Schechter function parametrization, which can be caused by residual stellar contamination, for example.

DES r-BAND, while it avoids many of the above issues by consisting of a single photometric catalog, does show overdensities in the redshift distribution of galaxies which are persistent across the entire footprint. While some of these features can be explained by real astrophysical clustering and overdensities (McMahon et al. 2026), they may also originate from biased spectroscopic training data which may project spurious features across the entire galaxy distribution. This effect will be mitigated in the future with better photometric observations across more filters and wavelengths.

Considerations on Modified Gravity—The considerations in the previous paragraphs apply also to modified-gravity analyses. The possible evolution of mass features with redshift could be potentially more impactful in this case, due to the redshift dependence of modified GW propagation.

A specific point to address is the flexibility of parametrizations used here. Our parameterized forms in Equations (11) and (12) enforce upon the distance ratio $D_{\rm L}^{\rm GW}/D_{\rm L}^{\rm EM}$ a limited range of redshift-dependent shapes. If these are a poor match for the behavior of an underlying modified gravity theory, constraints on Ξ_0 and c_M may not sufficiently capture a mismodelled deviation from GR. There remains scope for further model-independent methods to agnostically constrain the distance ratio.

We note that in full Horndeski gravity, the function α_M can also be constrained through its effects on the CMB. However, in this work we have fixed $\Omega_{\rm m}$ to a value inferred in a flat-ΛCDM analysis of Planck data (Ade et al. 2016). This may introduce a small bias in constraints on c_M, which we do not expect to be significant given the order-of-magnitude of the constraints obtained here. A fully correct approach would be to jointly analyze the Planck data alongside our GW events, which is beyond the scope of the present work; a related discussion is found in Lagos et al. (2019).

6. CONCLUSIONS

We have presented cosmological constraints obtained from the GWTC-5.0 catalog of GW events identified by the LVK detectors. Our headline results are updated bounds on the Hubble constant: $H_0 = 71.0^{+9.0}_{-7.1}\,\mathrm{km\,s^{-1}\,Mpc^{-1}}$, combining 235 dark siren events with the bright siren GW170817. This fiducial result uses the FullPop-4.0 mass model and redshift priors constructed from the DES Year 6 Gold galaxy catalog, with the GW host probability proportional to the galaxy luminosity. A summary of the different H_0 values obtained using various data sets and model assumptions can be found in Table 3.

The H_0 bounds obtained from our fiducial dark siren analysis are, for the first time, tighter than the single bright siren constraint ($H_0 = 67.6^{+13.6}_{-12.7}\,\mathrm{km\,s^{-1}\,Mpc^{-1}}$ vs. $H_0 = 79.1^{+27.6}_{-12.4}\,\mathrm{km\,s^{-1}\,Mpc^{-1}}$). This represents a turning point in the chronology of dark sirens cosmology; it has taken $\sim \mathcal{O}(200)$ dark sirens to stand favorably beside one bright siren. The change between the headline results of GWTC-5.0 and GWTC-4.0 is 25.7% in terms of reduced uncertainty, though we highlight that these use different galaxy catalogs (DES r-BAND and GLADE+ K_s-BAND respectively). Note that dark siren constraints from GWTC-2.0 and GWTC-3.0 shown in Figure 5 are not marginalized over mass distribution or merger rate parameters, due to methodological restrictions affecting analyses prior to GWTC-4.0. The bounds indicated by a star in Figure 5 should be considered as artificially tight for this reason. It remains true that our dark siren analyses are dominated by their spectral siren components, with galaxy catalog information improving the constraint on H_0 by 7.4% in the fiducial case. This is similar to the improvement of 8% reported in Abac et al. (2025b).

We have considered here a range of parameterized models for the mass distribution of compact objects. The tightest constraints on H_0 are obtained using the FullPop-4.0 and FullPop 3 Peaks models, which enable the NS and BH distributions to be jointly analyzed. For the first time we have also considered the impact of different spin distributions on cosmological constraints. We find strong evidence favoring the Transition spin model over the Gaussian spin model, although the impact of spin modeling on H_0 is relatively modest at this time. In a similar vein, we investigate the choice of luminosity weight applied to the galaxy catalog. We find that weighting of $\epsilon = 1$ significantly widens the variation in the H_0 posterior between the different galaxy catalogs. This is understandable physically, as luminosity weighting increases the effective catalog coverage of the event. This upweights the catalog's constraining power relative to the spectral sirens contribution.

For the first time, this work has investigated how galaxy catalogs of different sky area, completeness and redshift error distribution impact cosmological constraints. Although the DES Year 6 Gold galaxy catalog has only a moderate footprint at $\sim$5000 deg^2, and hence overlaps with only a fraction of events ($\sim$ 6%, see Table 1), this is compensated for by its substantially higher completeness at redshifts up to $z \sim 0.8$ than in the GLADE+ dataset (see Figure 3). As a result, the constraints obtained on H_0 with DES r-BAND are very similar to those using the K_s-band of the GLADE+ catalog, which is nearly full-sky but highly incomplete above $z = 0.1$. This finding bodes well for future analyses with Stage IV survey data, which will have depths broadly similar to DES Year 6 Gold but over larger fractions of the sky. For the present, however, many events are only weakly informed by the distribution of potential galaxy hosts; instead, features in the mass distribution of CBCs dominate the constraints. The DES catalog was chosen for our fiducial analysis due to a lack of strong preference for any catalog against the FullPop-4.0 spectral analysis in our Bayesian model comparison (see Table 2), however it does mildly improve the H_0 constraint when including it, relative to the spectral case.

In addition to placing constraints on the Hubble constant, we have presented bounds on parameterized deviations from GR affecting the GW luminosity distance. A summary of these constraints can be seen in Table 4. Using two commonly-employed parametrizations, we obtain the dark siren bounds of $\Xi_0 = 1.1^{+0.6}_{-0.3}$, $n = 3.4^{+4.2}_{-2.6}$ and $c_M = -0.4^{+1.6}_{-1.3}$, where the GR limit is recovered in the cases $\Xi_0 = 1$ and $c_M = 0$, respectively. Hence, our results show good consistency with GR on cosmological distance scales. The improvement in constraints on these parameters vary between $\sim$45.5% and $\sim$50% (when using a narrow H_0 prior) relative to previous GW analyses. This is because these constraints in particular utilize higher-redshift GW events and are scarcely impacted by galaxy catalog information; rather, they benefit from the $\sim$1.7-fold increase in GW event number in GWTC-5.0 over GWTC-4.0. While not on an equal footing with EM constraints (for parameters where these are available), this work demonstrates the potential of LVK events to act as an independent probe of cosmological modified gravity.

The next few years will also see further data releases from Stage IV galaxy surveys such as the Dark Energy Spectroscopic Instrument (Aghamousa et al. 2016), Euclid (Laureijs et al. 2011; Mellier et al. 2025), and the start of observations by the Vera Rubin Observatory (Ivezić et al. 2019). Using data from these EM campaigns is expected to strengthen the informativeness of the galaxy catalog component of the dark siren method. Forecasts using simulations of the 100 highest SNR events in O5 with a spectroscopic galaxy catalog

Modified gravity – Spectral sirens

Parametrization Ξ_0–n	Ξ_0	n
Wide H_0-prior	$1.1^{+0.6}_{-0.3}$ $(1.1^{+1.7}_{-0.5})$	$3.4^{+4.2}_{-2.6}$ $(3.4^{+5.9}_{-3.1})$
Narrow H_0-prior	$1.0^{+0.3}_{-0.2}$ $(1.0^{+0.6}_{-0.3})$	$3.8^{+3.8}_{-2.8}$ $(3.8^{+5.4}_{-3.4})$

Parametrization α_M	c_M
Wide H_0-prior	$-0.4^{+1.6}_{-1.3}$ $(-0.4^{+2.7}_{-2.0})$
Narrow H_0-prior	$-0.1^{+1.0}_{-0.8}$ $(-0.1^{+1.9}_{-1.2})$

Table 4. Values of the modified-gravity parameters Ξ_0, n and c_M constrained assuming two different models of modified GW propagation. All analyses are carried out assuming our fiducial population model FullPop-4.0 (235 GW candidates) in a spectral siren analysis. The prior on H_0 is $H_0 \in \mathrm{U}(10, 120)\,\mathrm{km\,s^{-1}\,Mpc^{-1}}$ in the wide case and $H_0 \in \mathrm{U}(65, 77)\,\mathrm{km\,s^{-1}\,Mpc^{-1}}$ in the narrow case. We adopt uniform priors for $\Xi_0 \in \mathrm{U}(0.435, 10)$ and $n \in \mathrm{U}(0.1, 10)$, and a uniform prior for $c_M \in \mathrm{U}(-10, 50)$. Columns are: H_0 prior chosen for the analysis (first column), modified gravity parameter measurement reported as a median with 68.3% (second column, first value) and 90% (second column, second value) symmetric CI. Note that, in contrast to Table 3, the bright siren GW170817 is not used as it is uninformative in this analysis.

are presented in Borghi et al. (2024, 2026); these indicate bounds on H_0 of $\sim 2\%$ are achievable for catalogs with an average of 50% completeness or higher inside the GW horizon. Having this kind of galaxy data in hand will accelerate the progress towards competitive GW constraints on the Hubble constant presented in Figure 5.

Future runs of the LVK detectors presumably will yield further bright siren detections, although these are rare. Such an event would likely give GW measurements of H_0 a rapid boost in constraining power. However, with or without such events, the methods and analyses of this paper demonstrate that dark and spectral sirens can provide steady progress towards the goals of precision GW cosmology.

Data Availability: All strain data analyzed as part of GWTC-5.0 are publicly available through Gravitational Wave Open Science Center (GWOSC). The details of this data release and information about the digital version of the GWTC are described in detail in Abac et al. (2026f). The data products generated by the methods described within this work are available from Zenodo (LIGO Scientific Collaboration et al. 2026).

ACKNOWLEDGEMENTS

This material is based upon work supported by NSF's LIGO Laboratory, which is a major facility fully funded by the National Science Foundation. The authors also gratefully acknowledge the support of the Science and Technology Facilities Council (STFC) of the United Kingdom, the Max-Planck-Society (MPS), and the State of Niedersachsen/Germany for support of the construction of Advanced LIGO and construction and operation of the GEO 600 detector. Additional support for Advanced LIGO was provided by the Australian Research Council. The authors gratefully acknowledge the Italian Istituto Nazionale di Fisica Nucleare (INFN), the French Centre National de la Recherche Scientifique (CNRS) and the Netherlands Organization for Scientific Research (NWO) for the construction and operation of the Virgo detector and the creation and support of the EGO consortium. The authors also gratefully acknowledge research support from these agencies as well as by the Council of Scientific and Industrial Research of India, the Department of Science and Technology, India, the Science & Engineering Research Board (SERB), India, the Ministry of Human Resource Development, India, the Spanish Agencia Estatal de Investigación (AEI), the Spanish Ministerio de Ciencia, Innovación y Universidades, the European Union NextGenerationEU/PRTR (PRTR-C17.I1), the ICSC - CentroNazionale di Ricerca in High Performance Computing, Big Data and Quantum Computing, funded by the European Union NextGenerationEU, the Comunitat Autonòma de les Illes Balears through the Conselleria d'Educació i Universitats, the Conselleria d'Innovació, Universitats, Ciència i Societat Digital de la Generalitat Valenciana and the CERCA Programme Generalitat de Catalunya, Spain, the Polish National Agency for Academic Exchange, the National Science Centre of Poland and the European Union - European Regional Development Fund; the Foundation for Polish Science (FNP), the Polish Ministry of Science and Higher Education, the Swiss National Science Foundation (SNSF), the Russian Science Foundation, the European Commission, the European Social Funds (ESF), the European Regional Development Funds (ERDF), the Royal Society, the Scottish Funding Council, the Scottish Universities Physics Alliance, the Hungarian Scientific Research Fund (OTKA), the French Lyon Institute of Origins (LIO), the Belgian Fonds de la Recherche Scientifique (FRS-FNRS), Actions de Recherche Concertées (ARC) and Fonds Wetenschappelijk Onderzoek - Vlaanderen (FWO), Belgium, the Paris Île-de-France Region, the National Research, Development and Innovation Office of Hungary (NKFIH), the National Research Foundation of Korea, the Natural Sciences and Engineering Research Council of Canada (NSERC), the Canadian

Foundation for Innovation (CFI), the Brazilian Ministry of Science, Technology, and Innovations, the International Center for Theoretical Physics South American Institute for Fundamental Research (ICTP-SAIFR), the Research Grants Council of Hong Kong, the National Natural Science Foundation of China (NSFC), the Israel Science Foundation (ISF), the US-Israel Binational Science Fund (BSF), the Leverhulme Trust, the Research Corporation, the National Science and Technology Council (NSTC), Taiwan, the United States Department of Energy, and the Kavli Foundation. The authors gratefully acknowledge the support of the NSF, STFC, INFN and CNRS for provision of computational resources.

This work was supported by MEXT, the JSPS Leading-edge Research Infrastructure Program, JSPS Grant-in-Aid for Specially Promoted Research 26000005, JSPS Grant-in-Aid for Scientific Research on Innovative Areas 2402: 24103006, 24103005, and 2905: JP17H06358, JP17H06361 and JP17H06364, JSPS Core-to-Core Program A. Advanced Research Networks, JSPS Grants-in-Aid for Scientific Research (S) 17H06133 and 20H05639, JSPS Grant-in-Aid for Transformative Research Areas (A) 20A203: JP20H05854, the joint research program of the Institute for Cosmic Ray Research, University of Tokyo, the National Research Foundation (NRF), the Computing Infrastructure Project of the Global Science experimental Data hub Center (GSDC) at KISTI, the Korea Astronomy and Space Science Institute (KASI), the Ministry of Science and ICT (MSIT) in Korea, Academia Sinica (AS), the AS Grid Center (ASGC) and the National Science and Technology Council (NSTC) in Taiwan under grants including the Science Vanguard Research Program, the Advanced Technology Center (ATC) of NAOJ, the Mechanical Engineering Center of KEK and Vietnam National Foundation for Science and Technology Development (NAFOSTED) 103.01-2025.147.

Additional acknowledgements for support of individual authors may be found in the following document: https://dcc.ligo.org/LIGO-M2300033/public. For the purpose of open access, the authors have applied a Creative Commons Attribution (CC BY) license to any Author Accepted Manuscript version arising. We request that citations to this article use 'A. G. Abac *et al.* (LIGO-Virgo-KAGRA Collaboration), ...' or similar phrasing, depending on journal convention.

Software: Calibration of the LIGO strain data was performed with GstLAL-based calibration software pipeline (Viets et al. 2018). Data-quality products and event-validation results were computed using the DMT (John Zweizig 2006), DQR (LIGO Scientific Collaboration and Virgo Collaboration 2018), DQSEGDB (Fisher et al. 2020), gwdetchar (Urban et al. 2021), hveto (Smith et al. 2011), iDQ (Essick et al. 2020), Omicron (Robinet et al. 2020) and PythonVirgoTools (Virgo Collaboration 2021) software packages and contributing software tools. Analyses in this catalog relied upon the LALSuite software library (LIGO Scientific Collaboration et al. 2018; Wette 2020). The detection of the signals and subsequent significance evaluations in this catalog were performed with the GstLAL-based inspiral software pipeline (Messick et al. 2017; Sachdev et al. 2019; Hanna et al. 2020; Cannon et al. 2020), with the MBTA pipeline (Adams et al. 2016; Aubin et al. 2021), and with the PyCBC (Usman et al. 2016; Nitz et al. 2017; Davies et al. 2020) and the cWB (Klimenko & Mitselmakher 2004; Klimenko et al. 2011, 2016) packages. Estimates of the noise spectra and glitch models were obtained using BayesWave (Cornish & Littenberg 2015; Littenberg et al. 2016; Cornish et al. 2021). Source-parameter estimation was performed with the Bilby library (Ashton et al. 2019; Romero-Shaw et al. 2020) using the Dynesty nested sampling package (Speagle 2020). PESummary was used to post-process and collate parameter-estimation results (Hoy & Raymond 2021). The various stages of the parameter-estimation analysis were managed with the Asimov library (Williams et al. 2023). Plots were prepared with Matplotlib (Hunter 2007), seaborn (Waskom 2021) and GWpy (Macleod et al. 2021). NumPy (Harris et al. 2020) and SciPy (Virtanen et al. 2020) were used in the preparation of the manuscript. We made use of the software packages `gwcosmo`, see https://git.ligo.org/lscsoft/gwcosmo and `icarogw`, see https://github.com/simone-mastrogiovanni/icarogw.

APPENDIX

A. MASS, MERGER RATE AND SPIN MODELS

In this appendix, we describe the population models that we have considered in this paper, both in terms of mass and merger rate of CBCs. All the adopted population models are composed of various simple mathematical functions which are described in the GWTC-4.0 cosmology paper (Abac et al. 2025b).

The MLTP model (Abbott et al. 2021c) is the direct extension of the PLP model used in the GWTC-4.0 cosmology paper. The equations describing the primary and secondary mass distributions for this model are given in Appendix C of the GWTC-4.0 cosmology paper. We report the parameter priors of the MLTP model in Table 5.

Multi Peak

Parameter	Description	Prior
α	Spectral index of primary-mass power law	$\mathrm{U}(1.5, 12)$
β	Spectral index of secondary-mass power law	$\mathrm{U}(-4, 12)$
m_{min}	Minimum primary mass $[M_\odot]$	$\mathrm{U}(2, 10)$
m_{max}	Maximum primary mass $[M_\odot]$	$\mathrm{U}(50, 200)$
δ_{m}	Smoothing parameter $[M_\odot]$	$\mathrm{U}(10^{-3}, 10)$
$\mu_{\mathrm{g}}^{\mathrm{low}}$	Location of the first peak $[M_\odot]$	$\mathrm{U}(5, 100)$
$\sigma_{\mathrm{g}}^{\mathrm{low}}$	Width of the first peak $[M_\odot]$	$\mathrm{U}(0.4, 10)$
$\mu_{\mathrm{g}}^{\mathrm{high}}$	Location of the second peak $[M_\odot]$	$\mathrm{U}(5, 100)$
$\sigma_{\mathrm{g}}^{\mathrm{high}}$	Width of the second peak $[M_\odot]$	$\mathrm{U}(0.4, 15)$
λ_{g}	Fraction of sources in the peaks	$\mathrm{U}(0, 1)$
$\lambda_{\mathrm{g}}^{\mathrm{low}}$	Fraction of sources in the first peak	$\mathrm{U}(0, 1)$

Table 5. Summary of the hyperparameters priors used for the MLTP model. U stands for uniform prior.

The FullPop-4.0 model (Abac et al. 2025d) spans the full mass distribution of CBCs and therefore includes BNSs, NSBHs, and BBHs. It consists of a broken power-law continuum, Gaussian peaks, and smoothing at the edges of the distribution. It additionally includes notch filters to allow for both lower and upper mass gaps (Ozel et al. 2010; Farr et al. 2011; Fryer et al. 2012; Belczynski et al. 2012; Mali & Essick 2025b). The depth of these mass gaps is a free parameter: the data can determine whether the rate goes to zero within the gap or if the gap is partially or totally filled. This model is an extension of the PowerLaw–Dip–Break model described in Fishbach et al. (2020); Farah et al. (2022), and is the same as the FullPop-4.0 model described in Abac et al. (2025d). The equations describing the primary and secondary mass distributions of FullPop-4.0 can be found also in Appendix C of the GWTC-4.0 cosmology paper. The full set of parameter priors, descriptions and notations, are shown in Table 6.

Additionally, we include an extended version of the FullPop-4.0 model, named the FullPop 3 Peaks, which incorporates an additional Gausssian peak (bringing the total number of peaks to three) to better capture potential features in the mass distribution. The primary and secondary mass distributions of the FullPop 3 Peaks model are of the form

$$\begin{aligned} p(m|\mathbf{\Lambda}) = \Bigg[& (1-\lambda_{\mathrm{g}})\mathcal{B}(m|m_{\mathrm{min}}, m_{\mathrm{max}}, \alpha_1, \alpha_2, b) \\ & + \lambda_{\mathrm{g}}\lambda_{\mathrm{g}}^{(1)}\mathcal{G}(m|\mu_{\mathrm{g}}^{(1)}, \sigma_{\mathrm{g}}^{(1)}, m_{\mathrm{min}}, m_{\mathrm{max}}) \\ & + \lambda_{\mathrm{g}}(1-\lambda_{\mathrm{g}}^{(1)})\lambda_{\mathrm{g}}^{(2)}\mathcal{G}(m|\mu_{\mathrm{g}}^{(2)}, \sigma_{\mathrm{g}}^{(2)}, m_{\mathrm{min}}, m_{\mathrm{max}}) \\ & + \lambda_{\mathrm{g}}(1-\lambda_{\mathrm{g}}^{(1)})(1-\lambda_{\mathrm{g}}^{(2)})\mathcal{G}(m|\mu_{\mathrm{g}}^{(3)}, \sigma_{\mathrm{g}}^{(3)}, m_{\mathrm{min}}, m_{\mathrm{max}}) \Bigg], \end{aligned} \tag{A.1}$$

which also retains the smoothing functions at the edges of the distribution and the notch filter as in the FullPop-4.0 model.

The notation for the Gaussian components has been updated to reflect the presence of three peaks, with means $\mu_{\mathrm{g}}^{(1,2,3)}$ and standard deviations $\sigma_{\mathrm{g}}^{(1,2,3)}$. The fractions of events in each peak are governed by λ_{g}, $\lambda_{\mathrm{g}}^{(1)}$, and $\lambda_{\mathrm{g}}^{(2)}$. The rest of the model components, including the broken power law $\mathcal{B}$ and the smoothing functions, remain unchanged from the FullPop-4.0 model. In this construction, to have an equal prior weight on each peak, we employ Beta priors on $\lambda_{\mathrm{g}}^{(1)}$ and $\lambda_{\mathrm{g}}^{(2)}$ such that its equivalent to a symmetric Dirichlet prior. Table 7 summarizes hyperparameters and prior distributions for the FullPop 3 Peaks model where they differ from the FullPop-4.0 model.

Moreover, we describe the merger rate evolution as a function of the redshift, modeled with a Madau–Dickinson parametrization (Madau & Dickinson 2014), which is characterized by parameters $\{\gamma, \kappa, z_{\mathrm{p}}\}$, where γ and κ are the power-law slopes respectively before and after the redshift turning point between the two power-law regimes, z_{p}. Explicitly,

$$\psi\left(z|\gamma, \kappa, z_{\mathrm{p}}\right) = \left[1 + (1+z_{\mathrm{p}})^{-\gamma-\kappa}\right] \frac{(1+z)^{\gamma}}{1 + \left[(1+z)/\left(1+z_{\mathrm{p}}\right)\right]^{\gamma+\kappa}}, \tag{A.2}$$

FullPop-4.0

Parameter	Description	Prior
α_1	Spectral index of the power law before b	$\mathrm{U}(-4, 12)$
α_2	Spectral index of the power law after b	$\mathrm{U}(-4, 12)$
β_1	Spectral index of the pairing function before m_{break}	$\mathrm{U}(-4, 12)$
β_2	Spectral index of the pairing function after m_{break}	$\mathrm{U}(-4, 12)$
m_{min}	Minimum primary and secondary mass $[M_\odot]$	$\mathrm{U}(0.4, 1.4)$
m_{max}	Maximum primary and secondary mass $[M_\odot]$	$\mathrm{U}(50, 200)$
$\delta_{\mathrm{m}}^{\mathrm{min}}$	1st smoothing parameter of the low mass $[M_\odot]$	$\mathrm{LU}(10^{-2}, 1)$
$\delta_{\mathrm{m}}^{\mathrm{max}}$	2nd smoothing parameter of the low mass $[M_\odot]$	$\mathrm{LU}(10^{-3}, 1)$
$\mu_{\mathrm{g}}^{\mathrm{low}}$	Location of the first peak $[M_\odot]$	$\mathrm{U}(5, 150)$
$\sigma_{\mathrm{g}}^{\mathrm{low}}$	Width of the first peak $[M_\odot]$	$\mathrm{U}(0.4, 10)$
$\mu_{\mathrm{g}}^{\mathrm{high}}$	Location of the second peak $[M_\odot]$	$\mathrm{U}(5, 150)$
$\sigma_{\mathrm{g}}^{\mathrm{high}}$	Width of the second peak $[M_\odot]$	$\mathrm{U}(0.4, 15)$
λ_{g}	Fraction of sources in peaks	$\mathrm{U}(0, 1)$
$\lambda_{\mathrm{g}}^{\mathrm{low}}$	Fraction of sources in the first peak	$\mathrm{U}(0, 1)$
$m_{\mathrm{d}}^{\mathrm{low}}$	Left side of the dip $[M_\odot]$	$\mathrm{U}(1.5, 3)$
$m_{\mathrm{d}}^{\mathrm{high}}$	Right side of the dip $[M_\odot]$	$\mathrm{U}(5, 9)$
$\delta_{\mathrm{d}}^{\mathrm{min}}$	Smoothing of the left side of the dip $[M_\odot]$	$\mathrm{LU}(0.01, 2)$
$\delta_{\mathrm{d}}^{\mathrm{max}}$	Smoothing of the right side of the dip $[M_\odot]$	$\mathrm{LU}(0.01, 2)$
A	Amplitude of the dip ($A = 1$; completely empty gap)	$\mathrm{U}(0, 1)$

Table 6. Summary of the hyperparameters priors used for the FullPop-4.0 mass model. U (LU) stands for uniform (log-uniform) prior.

FullPop 3 Peaks

Parameter	Description	Prior
$\lambda_{\mathrm{g}}^{(1)}$	Gaussian peak fraction one	$\mathrm{Beta}(1, 2)$
$\lambda_{\mathrm{g}}^{(2)}$	Gaussian peak fraction two	$\mathrm{Beta}(1, 1)$
$\mu_{\mathrm{g}}^{(1)}$	Location of the first peak $[M_\odot]$	$\mathrm{U}(5, 150)$
$\sigma_{\mathrm{g}}^{(1)}$	Width of the first peak $[M_\odot]$	$\mathrm{U}(0.4, 10)$
$\mu_{\mathrm{g}}^{(2)}$	Location of the second peak $[M_\odot]$	$\mathrm{U}(5, 150)$
$\sigma_{\mathrm{g}}^{(2)}$	Width of the second peak $[M_\odot]$	$\mathrm{U}(0.4, 15)$
$\mu_{\mathrm{g}}^{(3)}$	Location of the third peak $[M_\odot]$	$\mathrm{U}(5, 150)$
$\sigma_{\mathrm{g}}^{(3)}$	Width of the third peak $[M_\odot]$	$\mathrm{U}(0.4, 15)$

Table 7. Summary of the new hyperparameters priors used in the FullPop 3 Peaks model. U (LU) stands for uniform (log-uniform) prior.

with the parameter priors shown in Table 8. This parametrization is more complex than the one adopted in studies that focus solely on GW population properties, where usually it takes the form of simple power–laws, $\psi(z) \propto (1+z)^\gamma$ (Abbott et al. 2023c; Abac et al. 2026e). Our choice is motivated by the fact that, when varying the cosmology, a GW event at given distance can be associated with a redshift which is significantly higher than the one corresponding to the fiducial cosmology. The model in Equation (A.2) ensures that the merger rate decays after a peak at $z = z_{\mathrm{p}}$, consistently with astrophysical expectations. The Madau–Dickinson distribution is typically used to describe the cosmic star formation rate, while the CBC merger rate is then obtained by convolving this with a time-delay distribution. In practice, this

Merger rate model

Parameter	Description	Prior
γ	Slope of the power law before the point z_{p}	$\mathrm{U}(0, 12)$
κ	Slope of the power law after the point z_{p}	$\mathrm{U}(0, 6)$
z_{p}	Redshift turning point between the power laws	$\mathrm{U}(0, 4)$

Table 8. Summary of the hyperpriors used in the merger rate evolution model. Ustands for uniform prior.

is equivalent to using the same functional form with different values of γ and κ, and by adopting wide priors on these parameters we effectively account for a broad range of possible delay times.

Finally, the hyperparameters prior ranges used for the Gaussian and Transition spin model, described in Section 2.3 are shown in Tables 9 and 10.

Gaussian Spin model

Parameter	Description	Prior
μ_χ	Mean of the spin magnitude distribution	U(0, 1)
σ_χ	Variance of the spin magnitude distribution	U(0.05, 5)
σ_t	Width of the Gaussian component of the $\cos\theta$ distribution	U(0.1, 0.5)
ζ_{spin}	Mixing fraction for the spin components	U(0, 1)

Table 9. Summary of the hyperpriors used in the Gaussian spin model.

B. CATALOG DIAGNOSTIC DERIVATION

We propose a useful diagnostic statistic for galaxy catalogs f_{cov}, defined as the percentage of the total localization volume of N_{events} GW events that overlap with the three-dimensional completeness fraction of the catalog:

$$f_{\mathrm{cov}} = N_{\mathrm{events}}^{-1} \int \mathrm{d}D_L \, \frac{\mathrm{d}N_{\mathrm{events,cov}}}{\mathrm{d}D_L}. \tag{B.1}$$

The number of GW events, denoted by $\mathrm{d}N_{\mathrm{events,cov}}/\mathrm{d}D_L$, covered by a galaxy catalog per luminosity distance is given by

$$\frac{\mathrm{d}N_{\mathrm{events,cov}}}{\mathrm{d}D_L} = \sum_{j=1}^{N_{\mathrm{events}}} \sum_{i=1}^{N_{\mathrm{pix}}} p_{\mathrm{cat}}(D_L,\, \Omega_{i,j})\, p_{\mathrm{pix}}(\Omega_{i,j})\, \mathcal{N}(D_L,\, \mu(\Omega_{i,j}),\, \sigma(\Omega_{i,j}))\,, \tag{B.2}$$

where N_{events} is the number of events, N_{pix} is the number of pixels in the event skymap, and p_{cat} is the fraction of galaxies which are observable at the threshold magnitude of a given pixel, as a function of distance. $\mathcal{N}$ is a normalized Gaussian function of the mean μ and standard deviation σ distance given in each pixel of an event's skymap with sky location Ω, and p_{pix} is the localization probability assigned to that pixel. The variable p_{cat} is an adaptation of the out-of-catalog term in Eq. 2:

$$p_{\mathrm{cat}}(D_L,\, \Omega_{i,j}) = 1 - \Big(\int_{x_{\mathrm{thr}}(D_L,\, \Omega_{i,j})}^{x_{\mathrm{max}}} \mathrm{d}x \; x^{\alpha+\epsilon}\; e^{-x} \Big) \Big/ \Big(\int_{x_{\mathrm{min}}}^{x_{\mathrm{max}}} \mathrm{d}x \; x^{\alpha+\epsilon}\; e^{-x} \Big)\,, \tag{B.3}$$

where

$$x_{\mathrm{thr}}(D_L,\, \Omega_{i,j}) = 10^{0.4[M^* - M_{\mathrm{thr}}(D_L,\, m_{\mathrm{thr}}(\Omega_{i,j}))]}, \tag{B.4}$$

and

$$x_{\mathrm{max}} = 10^{0.4(M^* - M_{\mathrm{max}})}\,, \qquad x_{\mathrm{min}} = 10^{0.4(M^* - M_{\mathrm{min}})}\,. \tag{B.5}$$

The Schechter parameters α, M^*, M_{min}, and M_{max} are identical to parameters used when constructing the line-of-sight priors for each catalog. We choose the luminosity weighting factor $\epsilon = 1$ for diagnostic purposes. M_{thr} is the absolute magnitude at a given distance and apparent magnitude threshold for each pixel m_{thr}. Further details about the derivation of p_{cat} can be found in Appendix B of Abac et al. (2025b).

Spin Transition model

Parameter	Description	Prior
$\mu_{\chi 1}$	Mean of the spin magnitude distribution before the transition.	$\mathrm{U}(0,1)$
$\mu_{\chi 2}$	Mean of the spin magnitude distribution after the transition.	$\mathrm{U}(0,1)$
$\sigma_{\chi 1}$	Variance of the spin magnitude distribution before the transition.	$\mathrm{U}(0.05,5)$
$\sigma_{\chi 2}$	Variance of the spin magnitude distribution after the transition.	$\mathrm{U}(0.05,5)$
m_{t}	Transition mass between the first and second spin distribution $[M_\odot]$.	$\mathrm{U}(10,120)$
$\delta_{m_{\mathrm{t}}}$	Steepness of the spin transition $[M_\odot]$.	$\mathrm{U}(1,25)$
λ_{f}	Mixing fraction at between first and second spin distributions at mass=0.	$\mathrm{U}(0.8,1)$

Table 10. Summary of the hyperpriors used in the spin transition model.

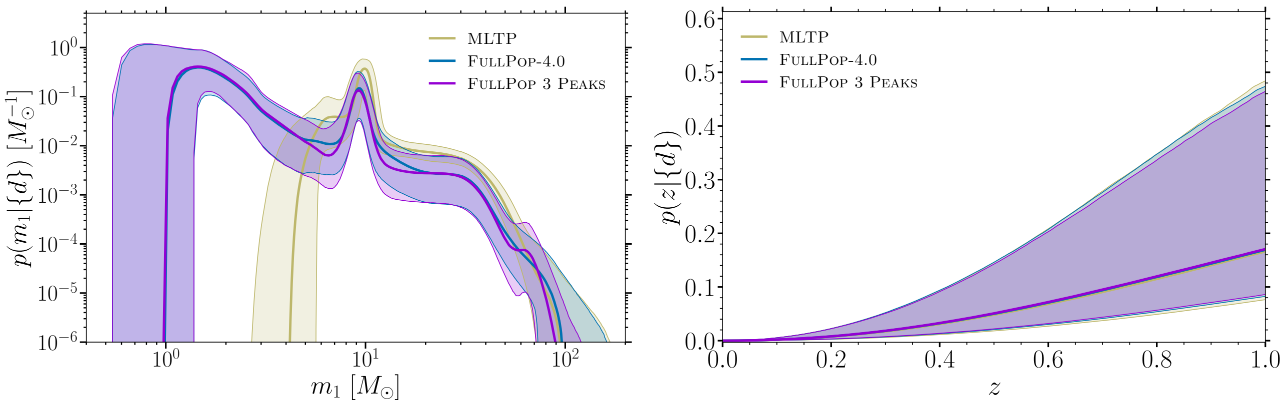

Figure 8. Left panel: Reconstructed source-frame primary-mass distribution (solid curve: median; shaded region: 90% CI). Right panel: reconstructed CBC merger rate as defined in the main text. Results in both panels are obtained from spectral siren analyses using the MLTP, FullPop-4.0 and FullPop 3 Peaks mass models.

C. JOINT POPULATION AND COSMOLOGICAL INFERENCE DETAILS

This appendix provides supplementary information regarding selected results from the joint astrophysical and cosmological analyses discussed in this paper. We show how the source population is reconstructed in the three different population models considered here. The left panel of Figure 8 shows the reconstructed primary mass spectrum using the MLTP, FullPop-4.0 and FullPop 3 Peaks mass models in the spectral siren analysis. The reconstructed mass distribution clearly presents different features. A markedly distinct peak around $10M_\odot$ as well as an overdensity at around $35M_\odot$ is captured by all three mass models, while an additional peak at higher masses is present in the BLPL+3P model. The high-end cut-off, at around 80-90 $M_\odot$ is similar for all three models, while the low-end cut-off of the BBH population is found around 5 $M_\odot$, identified by the MLTP model. With the use of the FullPop-4.0 and FullPop 3 Peaks models, we also gain access to the NS mass range. In particular, we find support for a minimum mass value around $1M_\odot$, though the FullPop 3 Peaks model prefers a slightly higher value. Overall, both FullPop-4.0 and FullPop 3 Peaks mass model reconstructs features in agreement with our single-population model, namely the MLTP. The right panel of Figure 8 presents the reconstruction of the CBC merger rate, defined as $p(z|\{d\}) \propto (\mathrm{d}V_{\mathrm{c}}/\mathrm{d}z)\psi(z|\boldsymbol{\Lambda})/(1+z)$, (see Section 2 for definitions of these quantities) as derived in the same spectral siren scenarios of the left panel. We find that the reconstructed redshift distributions are consistent across the three mass models considered in our analysis. We also note that uncertainty on the merger rate grows rapidly in redshift due to the bulk of observations being located at low redshift. Moreover in the absence of observations falling in the region around or above the expected peak of Madau-Dickinson function, any conclusion about the shape of the redshift distribution at the corresponding redshifts ($z \gtrsim 1$) is driven by the assumed parametric form of the merger rate and by the prior range of the associated parameters.

Finally, Figure 9 shows a reduced corner plot highlighting a subset of the population and cosmological hyperparameters inferred using our fiducial mass model in the dark siren analysis and luminosity-weighting case. We observe a correlation between H_0 and the locations of the two BH mass peaks, $\mu_{\mathrm{g}}^{\mathrm{low}}$ and $\mu_{\mathrm{g}}^{\mathrm{high}}$ (see Table 6), consistent with

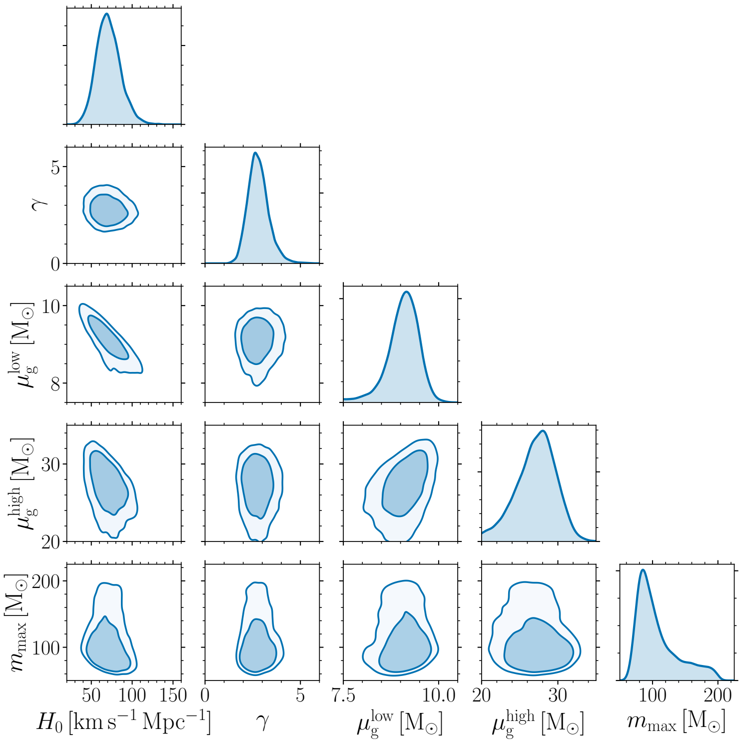

Figure 9. Corner plot showing H_0 and a subset of population parameters assuming the FullPop-4.0 mass model. The parameter γ is the low redfshift index of the Madau–Dickinson distribution, $\mu_{\rm g}^{\rm low}$ and $\mu_{\rm g}^{\rm high}$ are the central locations of the two peaks in the mass model, while $m_{\rm max}$ is the maximum allowed mass for either binary component. The solid contours indicate the 68.3% and 90% CR.

trends seen in our previous analysis (Abbott et al. 2023a; Abac et al. 2025b). Changing H_0 shifts the inferred redshift of the sources, which in turn rescales their intrinsic masses, so the mass spectrum shifts alongside H_0 to match the observed signals. In contrast, the maximum mass parameter $m_{\rm max}$ shows only a marginal correlation with H_0.

Overall, the Hubble constant appears to correlate only with certain mass scales, showing no significant correlation with merger-rate parameters such as the power-law index γ.

D. SPECTRAL SIREN RESULTS

In this appendix we report details on results using the spectral sirens method. Figure 10 displays the marginalized posteriors for the Hubble constant estimated with each of the three mass models considered. As for the galaxy catalog results (see Figure 4), we show the marginalized posterior for H_0 from the spectral siren analysis, with different mass models, as well as the posterior for the FullPop-4.0 model combined with the bright siren GW170817 (blue curve). The analyses using the MLTP, FullPop-4.0 and FullPop 3 Peaks mass models yield $H_0 = 71.0^{+21.0}_{-17.5}\,{\rm km\,s^{-1}\,Mpc^{-1}}$, $H_0 = 70.1^{+15.1}_{-13.3}\,{\rm km\,s^{-1}\,Mpc^{-1}}$ and $H_0 = 73.6^{+14.5}_{-13.0}\,{\rm km\,s^{-1}\,Mpc^{-1}}$, respectively. We observe that, as for the dark siren analysis, the best precision is also achieved using the FullPop-4.0 population mass model, which benefits from a larger number of GW events and more mass features. Our most precise estimate is obtained by combining the FullPop-4.0 model with GW170817, which leads to a value of $H_0 = 72.2^{+10.2}_{-7.8}\,{\rm km\,s^{-1}\,Mpc^{-1}}$, similar to the dark sirens results.

Figure 11 shows the reconstructed primary mass spectrum from the spectral analysis using the MLTP, FullPop-4.0 and FullPop 3 Peaks mass models. As for the dark siren analysis, the MLTP and FullPop-4.0 models identify two peaks at $9.1^{+0.4}_{-0.5}M_\odot$ and $27.1^{+2.4}_{-3.0}M_\odot$. For the NS region, the results are again consistent with the galaxy catalog analysis, supporting the presence of a shallow dip between $2.3^{+0.4}_{-0.5}M_\odot$ and $6.9^{+1.7}_{-1.5}M_\odot$.

Figure 11 presents the reduced corner plot showing the most interesting population and cosmological parameters derived from the spectral siren analysis with the FullPop-4.0 mass model, as in Figure 9. In addition, in Figure 11 we display results obtained with our two pipelines separately, to show explicitly their consistency. These results are consistent with those obtained from the dark siren analysis.

Finally, in addition to constraints on the Hubble constant, with the spectral siren approach in principle we are able to infer the present-day matter density of the Universe, $\Omega_{\rm m}$ and the dark energy equation-of-state parameter w_0. To

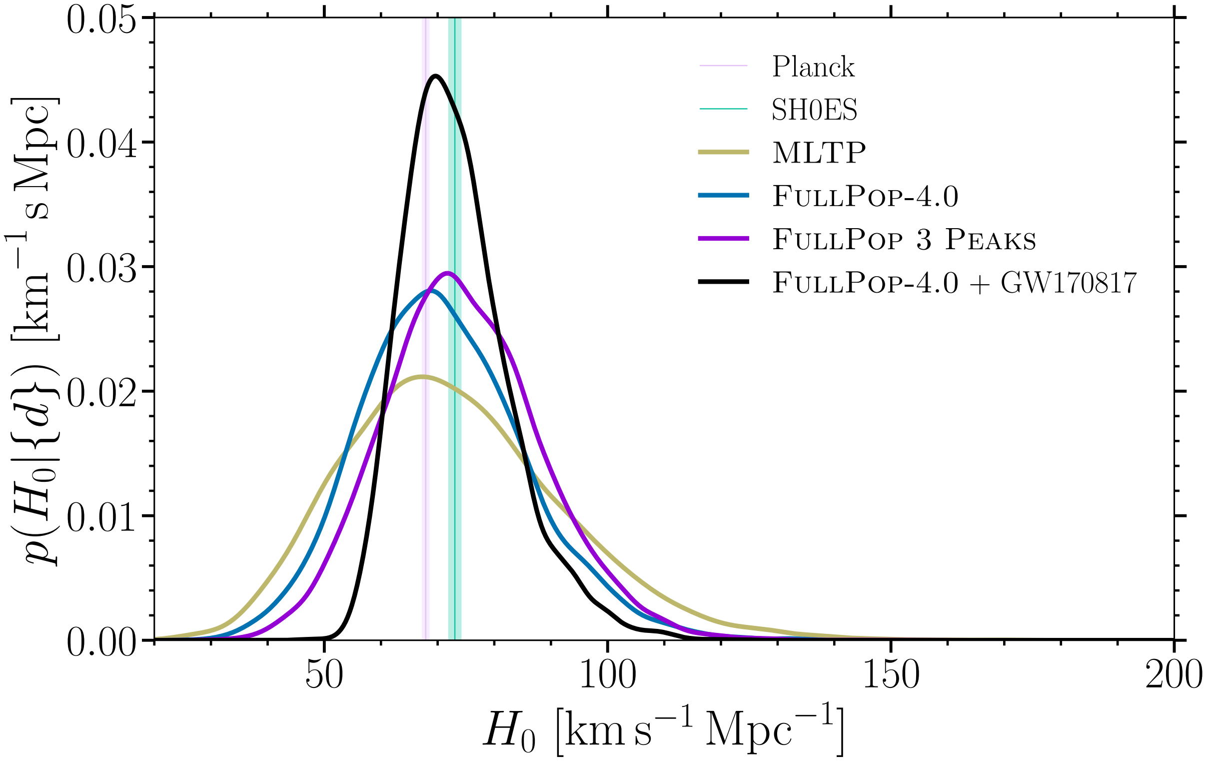

Figure 10. Hubble constant posteriors with the spectral sirens method assuming different population mass models, namely the MLTP (gold curve), FullPop-4.0 (blue curve) and FullPop 3 Peaks (purple curve). The black curve corresponds to the combined posterior between the FullPop-4.0 result and the bright siren posterior measured with GW170817. The pink and green shaded areas identify the 68% CI constraints on H_0 inferred from CMB anisotropies (Ade et al. 2016) and in the local Universe from SH0ES (Riess et al. 2022) respectively.

ΛCDM – Spectral sirens

Population model	**GW sources**	H_0 (Spectral sirens) [km s^{-1} Mpc^{-1}]	H_0 (Spectral + bright sirens) [km s^{-1} Mpc^{-1}]
Multi Peak	231 (232)	$71.0^{+21.0}_{-17.5}\,(71.0^{+36.0}_{-26.5})$	$73.4^{+12.5}_{-8.8}\,(73.4^{+24.1}_{-13.0})$
FullPop-4.0	235 (236)	$70.1^{+15.1}_{-13.3}\,(70.1^{+26.8}_{-21.5})$	$72.2^{+10.2}_{-7.8}\,(72.2^{+19.1}_{-11.8})$
FullPop 3 Peaks	235 (236)	$73.6^{+14.5}_{-13.0}\,(73.6^{+25.0}_{-20.9})$	$73.6^{+10.5}_{-8.0}\,(73.6^{+19.1}_{-12.1})$

Table 11. Constraints on the Hubble constant obtained in this work under the ΛCDM cosmological model, assuming a uniform prior $H_0 \in \mathrm{U}(10, 200)\,\mathrm{km\,s^{-1}\,Mpc^{-1}}$. The first column lists the mass model adopted in the analysis. The second column gives the number of GW events included in the dark-siren analysis. The third column reports the H_0 measurement obtained using only spectral sirens and the FullPop-4.0 mass model, quoted as the median together with the symmetric 68.3% and 90% CIs, with the latter in parentheses. The fourth column shows the corresponding constraints after combining the dark-siren analysis with the bright-siren posterior of GW170817.

facilitate comparison with the results of Section 4.1, the main results of this section keep Ω_m fixed. See Section 4.1 and Figure 12 for a discussion of the impact of varying Ω_m and w_0.

A summary of the different H_0 values obtained using different data sets and model assumptions can be seen in Table 11.

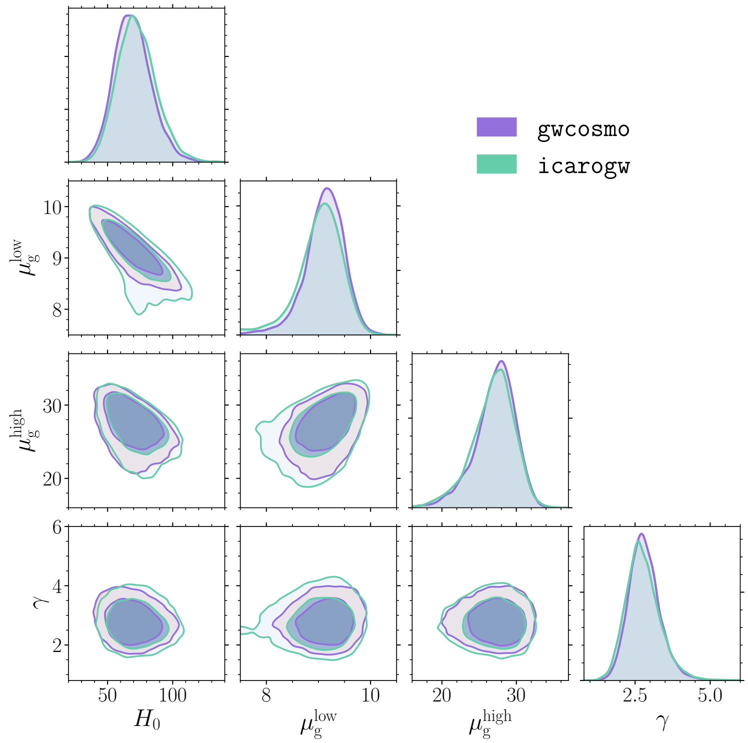

Figure 11. Spectral siren reduced corner plot of the Hubble constant and a subset of the FullPop-4.0 model mass parameters obtained with `gwcosmo` and `icarogw`. The contours indicate the 68.3% and 90% CR.

E. ROBUSTNESS CHECKS

In this appendix, we summarize checks conducted to ensure robustness of our results. Figure 12 shows a summary of the constraints on H_0 varying several assumptions discussed in Sections 4.1 and 4.2, with additional numerical stability checks that we discuss below. In particular, we display the effects of luminosity weighting, varying mass models and varying other parameters of the cosmic expansion history - specifically $\Omega_{\rm m,0}$. For these tests, we used the dark siren approach with the FullPop-4.0 mass model and a luminosity-weighting scheme for both the DES and GLADE+ K_s-band galaxy catalogs. For all of the analyses shown in Figure 12, we find that the medians of each posterior are consistent with the 68% CI of the others, with the exception of the IFAR (inverse false alarm rate) $> 1\,{\rm yr}^{-1}$ case, which is consistent with the others at the 90% CI level. The posteriors shown in this plot do not include constraints from GW170817. These results were obtained using only `gwcosmo` with the exception of the varying $\Omega_{\rm m,0}$ test, which was performed only with `icarogw`.

We do not repeat the additional numerical stability tests on the effective number of injections and PE samples which were included in (Abac et al. 2025b), as they were already shown to have a negligible impact on the results.

As mentioned in Section 2.1, our population models implicitly assume that the CBC spin distribution is isotropic with uniform distribution in the spin magnitudes (Abac et al. 2026c). However, we verified that including spin distributions for the BBH population using the Default model (Abbott et al. 2023c; Abac et al. 2026e) has no significant impact on the current cosmological constraints (see Section 5). For the spin-informed tests, we adopted the MLTP mass model, as this model better fits the BBH mass spectrum of the GW candidates used in our analysis (Abac et al. 2026e).

F. FURTHER COMMENTS ON MODIFIED-GRAVITY ANALYSES

Connection between α_M parametrization and gravitational coupling.—Here we supply further details on the connection between the Horndeski function $\alpha_M(z)$ and effective gravitational coupling strength, referenced in Section 2.4.2. In GR, the Planck mass enters via the constant factor appearing in the Einstein-Hilbert Lagrangian density: $\mathcal{L}_{\rm GR} = (M_P^2/2)\,R$. In Horndeski gravity this factor is generalised to be a function of the scalar field, i.e. $\mathcal{L}_{\rm Hd} = G_4(\phi)R + \dots$, where the dots indicate additional terms and we restricted the propagation speed of GWs to be luminal. α_M is then defined by the derivative:

$$\alpha_M(a) = \frac{\rm d\ln G_4(\phi[a])}{\rm d\ln a} \tag{F.1}$$

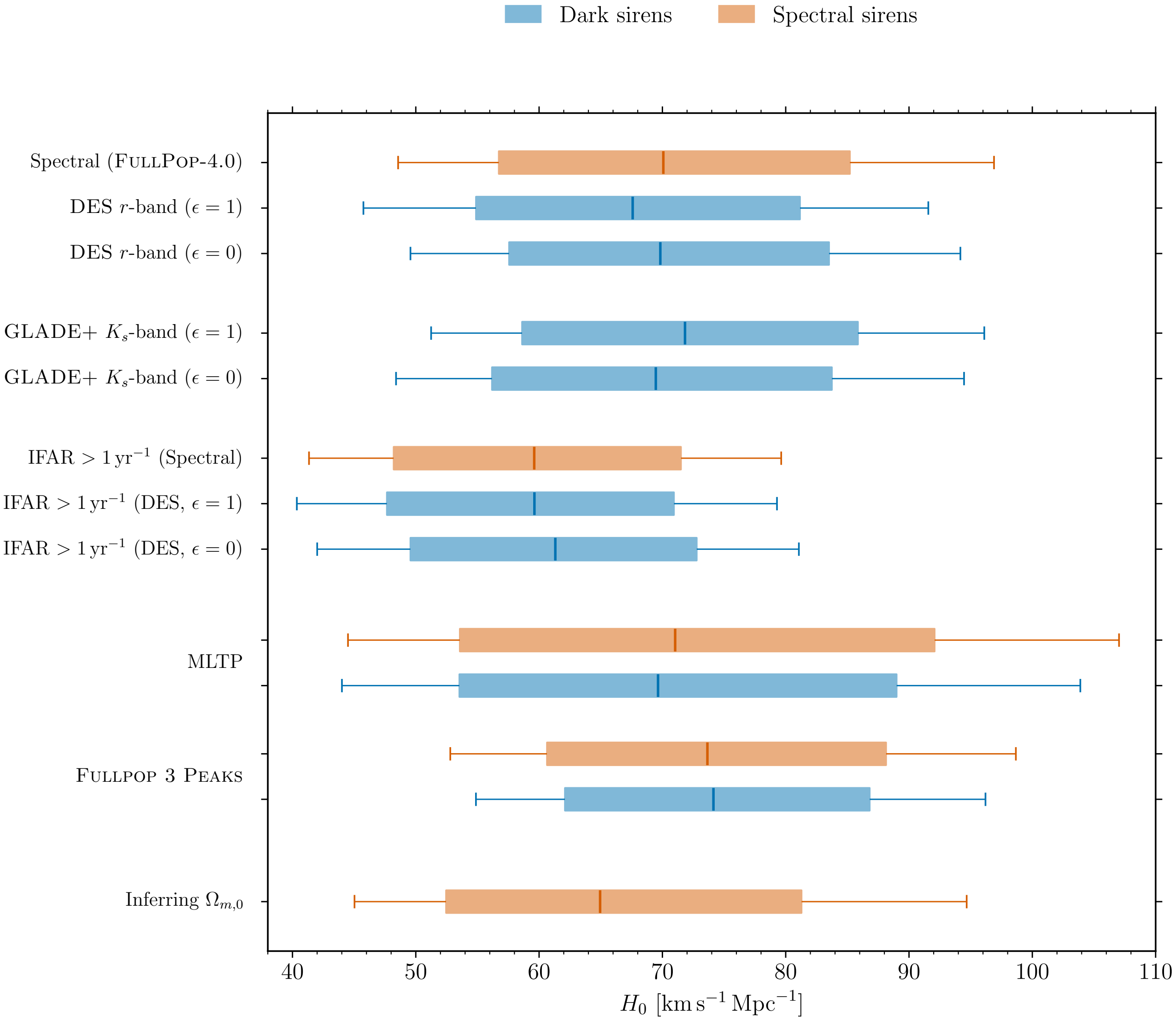

Figure 12. Robustness checks against various systematics discussed in Section 4, compared to the fiducial results (ΛCDM, FullPop-4.0, and luminosity-weighting case for the dark sirens case). The box-plots show the median value as a vertical segment. The colored boxes stretch to the 68.3% CI, while the whiskers extend to encompass the 90% CI. The labels indicate variations with respect to the fiducial results. The posteriors shown in this plot do *not* include bounds from GW170817. In the analysis with varying Ω_m the prior used was U$(0, 1)$.

Using Equation (F.1) in Equation (12), and restricting to theories where matter is minimally coupled to the metric, one reaches Equation (14).

Here the effective gravitational coupling G_GW is associated with the effective Planck mass, that is $G_\mathrm{GW} = 1/(16\pi G_4)$. As stressed in the main text, G_GW is not necessarily the same gravitational coupling strength constrained by large-scale structure surveys (commonly parameterized as μ), although it can be under certain conditions.

In short, by squaring our constraints on the GW–EM distance ratio in the α_M parametrization, we can obtain constraints on redshift evolution of an effective gravitational coupling strength for a large class of modified gravity models. This interpretation is displayed in the additional y-axis on the right-hand side of the middle panel in Figure 7.

Physically, the origin of Equation (14) can be understood as a requirement to ensure the conservation of gravitons, which is respected in most gravity theories – see Belgacem et al. (2018a) for details. We note that here we considered only the linear, homogeneous part of GW propagation; further deviations from GR may arise through propagation on inhomogeneous spacetimes (e.g. GW lensing) or in the nonlinear regime.

Results and corner plots of selected parameters—Figure 13 shows the marginalised posterior contours for the MG parameters and the low-redshift power-law slope of the merger rate, γ, for each of our three MG analyses. As discussed in the main text, γ is the parameter showing greatest degeneracy with MG parameters at present, an effect well-known in the literature (Mancarella et al. 2022; Leyde et al. 2022; Chen et al. 2024a). The priors and marginalised constraints on the MG parameters are reported in Table 4.

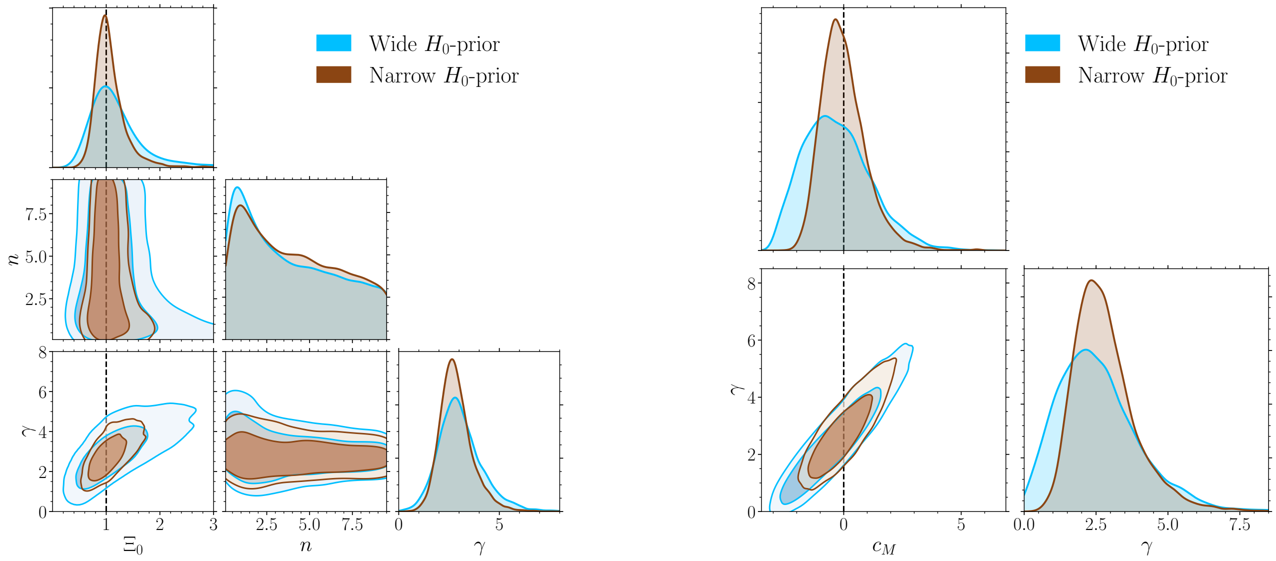

Figure 13. Corner plots of the modified gravity parametrizations Ξ_0–n (left), and c_M (right), and the merger rate parameter γ. These were obtained with the spectral siren method assuming the FullPop-4.0 mass model. Vertical dashed lines indicate the GR limit. Contours indicate the 68.3% and 90% CR.

All of the results show consistency with GR, marked for the MG parameters by the black dashed vertical lines in Figure 13.

As expected, for each alternative cosmological model we find a correlation between modified gravity parameters and the Hubble constant. c_M is positively correlated with H_0, with Pearson correlation coefficient 0.74, respectively. This explains the narrower error-bars on c_M when restricting H_0 with a narrower prior. For the $\Xi_0 - n$ parametrization more subtle effects are at play, as remarked upon in Section 4.2.

G. EVENT LIST

In this appendix we provide a list of the events used in our analyses with their main properties relevant for our analysis. For the details on the PE and waveform models used, see Sec. 3.1. For each of the events used in our analyses, Table 12 reports the following properties:

- D_L, and z: luminosity distance to the source and the corresponding redshift, calculated from the distance samples assuming Planck-15 (Ade et al. 2016) cosmology. We give the median of the samples and the 90% CI, cutting away 5% of samples at the edges of the posterior distribution
- Sky localization $\Delta\Omega$: the localization area of the event calculated from the skymap as a fraction of pixels containing the 90% of the probability
- Localization volume ΔV: localization volume of the event at 90% CI, calculated as the fraction corresponding to the 90% of the sky area (see above) of the spherical shell, at the 90% CI of the event's redshift distribution
- N_gal, over(under)-density and incompleteness: the number of galaxies inside the 90% localization volume, the over(under)-density fraction, and the catalog (K-band of the GLADE+ catalog) incompleteness percentage.

Table 12. List of the 236 CBC events selected with FAR $< 0.25\,\mathrm{yr}^{-1}$. Columns with a '*' have been computed assuming the reference cosmology in Ade et al. (2016), i.e. $H_0 = 67.9\,\mathrm{km\,s^{-1}\,Mpc^{-1}}$ and $\Omega_\mathrm{m} = 0.3065$. This table reports all of the GW events considered in this work and summarizes some of their properties reported with their median values and 90% symmetric CI (Abbott et al. 2019, 2021b, 2024, 2023b; Abac et al. 2026c). First, second and third columns: GW event label, luminosity distance and redshift. Fourth and fifth columns: sky localization area, and 3D localization comoving volume. The remaining columns list the number of galaxies inside the localization volume for each event, the under(over)-density of galaxies and the incompleteness fraction of the catalog for each event, for both the DES r-BAND and GLADE+ K_s-BAND catalogs. The under(over)-density is computed as the fraction between the number of galaxies (in the K and r-bands respectively) corrected for incompleteness, and the effective number expected from the Schechter function. We report the minimum and maximum values, respectively. The lower and upper bounds on the incompleteness probabilities, instead, are derived from the incompleteness fractions at the boundaries of the 90% localization volume. These columns, number of galaxies, under(over)-density, and incompleteness fraction, do not apply to the GW170817 event. We report these values using a distance prior proportional to D_L^2. For events released with GWTC-3.0, we use the first data release associated with Abbott et al. (2023b).

Name	D_L [Mpc]	z^*	$\Delta\Omega$ [deg^2]	ΔV^* [Gpc^3]	$N_\mathrm{gal}^\mathrm{DES}$	$N_\mathrm{gal}^\mathrm{GLADE+}$	Under(over)$^\mathrm{DES}$	Under(over)$^\mathrm{GLADE+}$	Incompleteness$^\mathrm{DES}$ (%)	Incompleteness$^\mathrm{GLADE+}$ (%)
GW150914	463^{+132}_{-142}	$0.10^{+0.03}_{-0.03}$	157	1.9×10^{-3}	182	1.5×10^3	0.84–∼1	1.05–1.17	100–100	60–95
GW151012	1056^{+621}_{-493}	$0.21^{+0.10}_{-0.09}$	1.5×10^3	0.30	5.6×10^3	6.7×10^3	0.92–0.96	∼1–1.05	100–100	94–100
GW151226	471^{+158}_{-196}	$0.10^{+0.03}_{-0.04}$	984	0.01	0	9.8×10^3	∼1–∼1	0.96–1.16	100–100	50–97
GW170104	1126^{+385}_{-466}	$0.22^{+0.07}_{-0.09}$	950	0.14	7.7×10^4	5.7×10^3	0.93–1.04	∼1–1.07	0–0	97–100
GW170608	334^{+123}_{-117}	$0.07^{+0.03}_{-0.02}$	387	2.5×10^{-3}	0	3.0×10^3	∼1–∼1	0.72–1.11	100–100	32–81
GW170729	2874^{+1630}_{-1474}	$0.49^{+0.22}_{-0.23}$	1.1×10^3	1.8	8.0×10^4	100	0.85–∼1	∼1–∼1	0–100	100–100
GW170809	1117^{+298}_{-352}	$0.22^{+0.05}_{-0.06}$	269	0.03	3.8×10^5	992	0.86–1.04	∼1–1.07	0–0	99–100
GW170814	600^{+165}_{-226}	$0.12^{+0.03}_{-0.04}$	86	2.2×10^{-3}	3.2×10^4	1.3×10^3	1.03–1.43	1.03–1.31	0–0	69–99
GW170817	42^{+6}_{-13}	$0.01^{+0.00}_{-0.00}$	-	-	-	-	-	-	-	-
GW170818	1178^{+408}_{-422}	$0.23^{+0.07}_{-0.08}$	28	4.4×10^{-3}	0	40	∼1–∼1	∼1–1.02	100–100	99–100
GW170823	2115^{+836}_{-910}	$0.38^{+0.12}_{-0.15}$	1.6×10^3	1.1	0	316	∼1–∼1	∼1–∼1	100–100	100–100
GW190408_181802	1575^{+439}_{-595}	$0.30^{+0.07}_{-0.10}$	267	0.07	0	215	∼1–∼1	∼1–1.01	100–100	100–100
GW190412	700^{+167}_{-187}	$0.14^{+0.03}_{-0.04}$	33	1.0×10^{-3}	0	115	∼1–∼1	0.89–1.06	100–100	85–99
GW190413_134308	4607^{+2384}_{-2202}	$0.73^{+0.29}_{-0.30}$	552	2.0	0	0	∼1–∼1	∼1–∼1	100–100	100–100
GW190421_213856	2958^{+1450}_{-1359}	$0.51^{+0.20}_{-0.21}$	1.2×10^3	1.9	0	0	∼1–∼1	∼1–∼1	100–100	100–100
GW190425	143^{+75}_{-61}	$0.03^{+0.02}_{-0.01}$	9.0×10^3	7.9×10^{-3}	0	9.2×10^3	∼1–∼1	0.67–1.04	100–100	5–34
GW190503_185404	1596^{+658}_{-640}	$0.30^{+0.10}_{-0.11}$	104	0.04	1.2×10^5	46	0.69–∼1	∼1–1.01	0–100	100–100
GW190512_180714	1534^{+470}_{-621}	$0.29^{+0.07}_{-0.11}$	293	0.08	0	173	∼1–∼1	∼1–1.01	100–100	100–100
GW190513_205428	2283^{+934}_{-772}	$0.41^{+0.14}_{-0.12}$	470	0.35	0	11	∼1–∼1	∼1–∼1	100–100	100–100
GW190517_055101	1920^{+1846}_{-976}	$0.35^{+0.27}_{-0.16}$	411	0.50	0	201	∼1–∼1	∼1–1.01	100–100	100–100
GW190519_153544	3057^{+2027}_{-1343}	$0.52^{+0.27}_{-0.20}$	617	1.3	0	0	∼1–∼1	∼1–∼1	100–100	100–100
GW190521	4527^{+2265}_{-2635}	$0.72^{+0.28}_{-0.37}$	919	3.4	6.8×10^3	25	0.92–∼1	∼1–∼1	1–100	100–100
GW190521_074359	961^{+498}_{-420}	$0.19^{+0.09}_{-0.08}$	445	0.06	0	1.6×10^3	∼1–∼1	∼1–1.04	100–100	93–100
GW190527_092055	3221^{+4197}_{-1686}	$0.54^{+0.53}_{-0.25}$	3.7×10^3	16	4.2×10^5	54	0.84–∼1	∼1–∼1	0–100	100–100
GW190602_175927	3274^{+2026}_{-1438}	$0.55^{+0.27}_{-0.21}$	782	1.8	8.7×10^4	0	0.89–∼1	∼1–∼1	1–100	100–100
GW190620_030421	3418^{+1670}_{-1556}	$0.57^{+0.22}_{-0.23}$	5.6×10^3	11	1.6×10^4	33	0.97–∼1	∼1–∼1	1–100	100–100
GW190630_185205	908^{+550}_{-380}	$0.18^{+0.10}_{-0.07}$	1.1×10^3	0.15	1.3×10^4	9.3×10^3	0.86–0.98	∼1–1.07	100–100	89–100
GW190701_203306	2217^{+807}_{-762}	$0.40^{+0.12}_{-0.12}$	42	0.03	8.5×10^4	0	0.98–1.07	∼1–∼1	0–100	100–100
GW190706_222641	4420^{+2678}_{-2328}	$0.70^{+0.33}_{-0.33}$	2.4×10^3	9.4	0	31	∼1–∼1	∼1–∼1	100–100	100–100

Table 12 *continued*

Table 12 *(continued)*

Name	$D_{\rm L}$ [Mpc]	z^*	$\Delta\Omega$ [deg^2]	ΔV^* [Gpc^3]	$N_{\rm gal}^{\rm DES}$	$N_{\rm gal}^{\rm GLADE+}$	Under(over)$^{\rm DES}$	Under(over)$^{\rm GLADE+}$	Incompleteness$^{\rm DES}$ (%)	Incompleteness$^{\rm GLADE+}$ (%)
GW190707_093326	842^{+320}_{-366}	$0.17^{+0.06}_{-0.07}$	890	0.07	0	3.0×10^3	∼1–∼1	∼1–1.07	100–100	89–100
GW190708_232457	963^{+304}_{-386}	$0.19^{+0.05}_{-0.07}$	1.1×10^4	1.0	9.1×10^4	4.9×10^4	0.87–0.96	∼1–1.05	0–0	93–100
GW190720_000836	775^{+571}_{-243}	$0.16^{+0.10}_{-0.05}$	95	0.01	0	459	∼1–∼1	∼1–1.12	100–100	90–100
GW190727_060333	3235^{+1210}_{-1184}	$0.55^{+0.16}_{-0.17}$	112	0.16	0	0	∼1–∼1	∼1–∼1	100–100	100–100
GW190728_064510	907^{+247}_{-399}	$0.18^{+0.04}_{-0.07}$	342	0.03	0	1.8×10^3	∼1–∼1	∼1–1.05	100–100	90–100
GW190803_022701	3573^{+1676}_{-1520}	$0.59^{+0.22}_{-0.22}$	974	2.1	0	18	∼1–∼1	∼1–∼1	100–100	100–100
GW190814	233^{+43}_{-46}	$0.05^{+0.01}_{-0.01}$	26	3.2×10^{-5}	201	72	0.72–∼1	0.55–1.57	100–0	25–47
GW190828_063405	2191^{+599}_{-925}	$0.39^{+0.09}_{-0.15}$	323	0.18	0	20	∼1–∼1	∼1–∼1	100–100	100–100
GW190828_065509	1646^{+674}_{-660}	$0.31^{+0.10}_{-0.11}$	564	0.22	0	181	∼1–∼1	∼1–∼1	100–100	100–100
GW190910_112807	1878^{+986}_{-873}	$0.34^{+0.15}_{-0.15}$	8.0×10^3	5.3	0	3.0×10^3	∼1–∼1	∼1–1.01	100–100	100–100
GW190915_235702	1886^{+705}_{-681}	$0.35^{+0.11}_{-0.11}$	452	0.22	0	416	∼1–∼1	∼1–1.01	100–100	100–100
GW190924_021846	556^{+205}_{-225}	$0.12^{+0.04}_{-0.04}$	387	0.01	0	4.4×10^3	∼1–∼1	0.90–1.12	100–100	57–99
GW190925_232845	937^{+377}_{-337}	$0.19^{+0.07}_{-0.06}$	1.0×10^3	0.10	0	5.0×10^3	∼1–∼1	∼1–1.05	100–100	95–100
GW190929_012149	3769^{+3147}_{-1692}	$0.62^{+0.40}_{-0.24}$	1.7×10^3	6.2	0	0	∼1–∼1	∼1–∼1	100–100	100–100
GW190930_133541	790^{+318}_{-325}	$0.16^{+0.06}_{-0.06}$	1.5×10^3	0.11	0	4.7×10^3	∼1–∼1	∼1–1.03	100–100	86–100
GW191105_143521	1203^{+404}_{-474}	$0.23^{+0.07}_{-0.09}$	672	0.11	2.2×10^5	2.7×10^3	0.79–0.99	∼1–1.03	0–0	98–100
GW191109_010717	1318^{+1378}_{-666}	$0.25^{+0.21}_{-0.12}$	1.5×10^3	0.90	0	4.5×10^3	∼1–∼1	∼1–1.04	100–100	98–100
GW191127_050227	4595^{+3459}_{-2627}	$0.73^{+0.42}_{-0.37}$	1.0×10^3	5.1	0	1	∼1–∼1	∼1–∼1	100–100	100–100
GW191129_134029	803^{+237}_{-320}	$0.16^{+0.04}_{-0.06}$	848	0.05	4.6×10^4	8.8×10^3	0.90–1.05	1.01–1.07	0–0	85–100
GW191204_171526	644^{+180}_{-219}	$0.13^{+0.03}_{-0.04}$	254	7.6×10^{-3}	3.4×10^4	2.2×10^3	0.79–0.89	1.02–1.11	0–0	80–100
GW191215_223052	2102^{+866}_{-935}	$0.38^{+0.13}_{-0.15}$	577	0.40	0	110	∼1–∼1	∼1–∼1	100–100	100–100
GW191216_213338	343^{+109}_{-129}	$0.07^{+0.02}_{-0.03}$	223	1.4×10^{-3}	0	1.2×10^3	∼1–∼1	0.79–1.52	100–100	34–83
GW191222_033537	3382^{+1623}_{-1768}	$0.57^{+0.21}_{-0.26}$	1.9×10^3	3.8	0	5	∼1–∼1	∼1–∼1	100–100	100–100
GW191230_180458	4841^{+2194}_{-2099}	$0.76^{+0.27}_{-0.28}$	1.1×10^3	3.8	0	0	∼1–∼1	∼1–∼1	100–100	100–100
GW200112_155838	1299^{+427}_{-458}	$0.25^{+0.07}_{-0.08}$	3.2×10^3	0.61	6.6×10^5	5.5×10^3	0.83–0.98	∼1–1.02	0–0	100–100
GW200115_042309	292^{+133}_{-92}	$0.06^{+0.03}_{-0.02}$	416	2.2×10^{-3}	4.4×10^3	2.0×10^3	0.65–1.08	0.86–1.39	100–0	30–79
GW200128_022011	3871^{+2131}_{-1972}	$0.63^{+0.27}_{-0.28}$	2.1×10^3	6.2	0	8	∼1–∼1	∼1–∼1	100–100	100–100
GW200129_065458	973^{+219}_{-341}	$0.19^{+0.04}_{-0.06}$	30	2.2×10^{-3}	571	154	0.77–0.91	∼1–1.22	100–100	97–100
GW200202_154313	422^{+146}_{-160}	$0.09^{+0.03}_{-0.03}$	157	1.9×10^{-3}	0	1.1×10^3	∼1–∼1	0.58–1.01	100–100	38–88
GW200208_130117	2371^{+1029}_{-912}	$0.42^{+0.15}_{-0.14}$	33	0.03	0	0	∼1–∼1	∼1–∼1	100–100	100–100
GW200209_085452	3935^{+1972}_{-1875}	$0.64^{+0.25}_{-0.27}$	849	2.3	0	1	∼1–∼1	∼1–∼1	100–100	100–100
GW200219_094415	3830^{+1677}_{-1735}	$0.63^{+0.22}_{-0.25}$	682	1.6	0	18	∼1–∼1	∼1–∼1	100–100	100–100
GW200224_222234	1772^{+473}_{-658}	$0.33^{+0.07}_{-0.11}$	42	0.01	0	21	∼1–∼1	∼1–1.08	100–100	100–100
GW200225_060421	1157^{+505}_{-492}	$0.23^{+0.08}_{-0.09}$	482	0.09	0	1.6×10^3	∼1–∼1	∼1–1.04	100–100	98–100
GW200302_015811	1582^{+1028}_{-733}	$0.30^{+0.16}_{-0.13}$	5.6×10^3	3.1	0	4.0×10^3	∼1–∼1	∼1–1.01	100–100	100–100
GW200311_115853	1203^{+277}_{-388}	$0.23^{+0.05}_{-0.07}$	34	4.2×10^{-3}	1.2×10^4	89	0.60–0.91	∼1–1.02	0–0	99–100
GW200316_215756	1134^{+434}_{-429}	$0.22^{+0.07}_{-0.08}$	209	0.03	0	321	∼1–∼1	∼1–1.03	100–100	99–100

Table 12 *continued*

Table 12 *(continued)*

Name	$D_{\rm L}$ [Mpc]	z^*	$\Delta\Omega$ [deg^2]	ΔV^* [Gpc^3]	$N_{\rm gal}^{\rm DES}$	$N_{\rm gal}^{\rm GLADE+}$	Under(over)$^{\rm DES}$	Under(over)$^{\rm GLADE+}$	Incompleteness$^{\rm DES}$ (%)	Incompleteness$^{\rm GLADE+}$ (%)
GW230529_181500	206^{+100}_{-98}	$0.04^{+0.02}_{-0.02}$	2.4×10^4	0.06	9	8.5×10^3	∼1–1.04	0.83–1.21	100–100	10–58
GW230601_224134	3642^{+2137}_{-1802}	$0.60^{+0.28}_{-0.26}$	3.0×10^3	8.0	7.9×10^4	15	0.91–∼1	∼1–∼1	1–100	100–100
GW230605_065343	1059^{+620}_{-477}	$0.21^{+0.10}_{-0.09}$	1.0×10^3	0.20	0	1.7×10^3	∼1–∼1	∼1–1.03	100–100	96–100
GW230606_004305	2743^{+1531}_{-1407}	$0.47^{+0.21}_{-0.22}$	1.4×10^3	2.1	0	236	∼1–∼1	∼1–∼1	100–100	100–100
GW230608_205047	3491^{+2242}_{-1732}	$0.58^{+0.29}_{-0.26}$	2.2×10^3	5.9	0	23	∼1–∼1	∼1–∼1	100–100	100–100
GW230609_064958	3362^{+1927}_{-1761}	$0.56^{+0.25}_{-0.26}$	1.6×10^3	3.7	0	24	∼1–∼1	∼1–∼1	100–100	100–100
GW230624_113103	2014^{+1249}_{-1012}	$0.37^{+0.18}_{-0.17}$	1.1×10^3	0.99	0	364	∼1–∼1	∼1–1.01	100–100	100–100
GW230627_015337	308^{+62}_{-136}	$0.07^{+0.01}_{-0.03}$	98	3.6×10^{-4}	0	569	∼1–∼1	0.69–1.10	100–100	19–62
GW230628_231200	2290^{+812}_{-1067}	$0.41^{+0.12}_{-0.17}$	637	0.48	0	308	∼1–∼1	∼1–1.01	100–100	100–100
GW230630_125806	5536^{+5171}_{-3094}	$0.85^{+0.60}_{-0.42}$	4.0×10^3	32	0	0	∼1–∼1	∼1–∼1	100–100	100–100
GW230630_234532	1082^{+521}_{-482}	$0.21^{+0.09}_{-0.09}$	1.3×10^3	0.23	7.8×10^4	7.2×10^3	0.84–0.94	∼1–1.03	0–0	95–100
GW230702_185453	2482^{+1940}_{-1148}	$0.44^{+0.27}_{-0.18}$	2.4×10^3	4.0	0	277	∼1–∼1	∼1–∼1	100–100	100–100
GW230704_021211	2713^{+1889}_{-1464}	$0.47^{+0.26}_{-0.23}$	1.6×10^3	2.9	9.7×10^5	282	0.85–∼1	∼1–1.01	0–100	100–100
GW230706_104333	1941^{+918}_{-985}	$0.35^{+0.14}_{-0.16}$	1.4×10^3	0.91	0	878	∼1–∼1	∼1–1.01	100–100	100–100
GW230707_124047	4525^{+2335}_{-2287}	$0.72^{+0.29}_{-0.32}$	3.0×10^3	11	0	0	∼1–∼1	∼1–∼1	100–100	100–100
GW230708_053705	3307^{+2077}_{-1685}	$0.56^{+0.27}_{-0.25}$	1.9×10^3	4.5	0	84	∼1–∼1	∼1–∼1	100–100	100–100
GW230708_230935	3482^{+2287}_{-1623}	$0.58^{+0.30}_{-0.24}$	2.4×10^3	6.6	0	0	∼1–∼1	∼1–∼1	100–100	100–100
GW230709_122727	4716^{+3482}_{-2489}	$0.74^{+0.42}_{-0.34}$	3.2×10^3	16	0	0	∼1–∼1	∼1–∼1	100–100	100–100
GW230712_090405	2105^{+2552}_{-1075}	$0.38^{+0.36}_{-0.18}$	1.5×10^3	2.8	0	746	∼1–∼1	∼1–1.00	100–100	100–100
GW230723_101834	1610^{+682}_{-919}	$0.30^{+0.11}_{-0.16}$	1.1×10^3	0.45	0	2.5×10^3	∼1–∼1	∼1–1.03	100–100	98–100
GW230726_002940	2068^{+1289}_{-1064}	$0.37^{+0.19}_{-0.17}$	2.9×10^4	28	9.3×10^5	8.1×10^3	0.87–∼1	∼1–1.01	0–100	100–100
GW230729_082317	1650^{+811}_{-777}	$0.31^{+0.13}_{-0.13}$	2.1×10^3	0.98	0	1.5×10^3	∼1–∼1	∼1–1.01	100–100	100–100
GW230731_215307	1103^{+353}_{-458}	$0.22^{+0.06}_{-0.08}$	671	0.09	9.5×10^4	4.1×10^3	0.88–1.05	∼1–1.04	0–0	96–100
GW230805_034249	3357^{+2479}_{-1648}	$0.56^{+0.32}_{-0.24}$	2.3×10^3	6.4	0	9	∼1–∼1	∼1–∼1	100–100	100–100
GW230806_204041	5472^{+3719}_{-2865}	$0.84^{+0.44}_{-0.38}$	4.2×10^3	25	0	0	∼1–∼1	∼1–∼1	100–100	100–100
GW230811_032116	2108^{+1187}_{-1116}	$0.38^{+0.17}_{-0.18}$	915	0.83	0	429	∼1–∼1	∼1–1.01	100–100	100–100
GW230814_061920	4141^{+3495}_{-2104}	$0.67^{+0.43}_{-0.30}$	4.7×10^3	21	0	0	∼1–∼1	∼1–∼1	100–100	100–100
GW230814_230901	282^{+167}_{-127}	$0.06^{+0.03}_{-0.03}$	2.5×10^4	0.17	3.3×10^4	8.2×10^4	0.75–1.05	0.83–1.08	100–0	19–82
GW230819_171910	4104^{+3727}_{-2224}	$0.66^{+0.46}_{-0.32}$	4.6×10^3	22	6.4×10^3	21	0.94–∼1	∼1–∼1	1–100	100–100
GW230820_212515	3975^{+3008}_{-2071}	$0.65^{+0.38}_{-0.30}$	2.1×10^3	8.1	0	0	∼1–∼1	∼1–∼1	100–100	100–100
GW230824_033047	4735^{+2864}_{-2331}	$0.75^{+0.35}_{-0.32}$	3.9×10^3	17	0	2	∼1–∼1	∼1–∼1	100–100	100–100
GW230825_041334	5218^{+4252}_{-3024}	$0.81^{+0.50}_{-0.41}$	3.2×10^3	21	0	0	∼1–∼1	∼1–∼1	100–100	100–100
GW230904_051013	1042^{+589}_{-448}	$0.21^{+0.10}_{-0.08}$	1.8×10^3	0.33	0	6.6×10^3	∼1–∼1	∼1–1.04	100–100	95–100
GW230911_195324	1355^{+1183}_{-710}	$0.26^{+0.19}_{-0.13}$	2.7×10^4	15	9.7×10^5	4.8×10^4	0.86–∼1	∼1–1.04	0–100	97–100
GW230914_111401	2647^{+1668}_{-1205}	$0.46^{+0.23}_{-0.19}$	1.9×10^3	3.0	0	55	∼1–∼1	∼1–∼1	100–100	100–100
GW230919_215712	1336^{+796}_{-521}	$0.26^{+0.13}_{-0.09}$	699	0.23	1.6×10^5	1.1×10^3	0.76–∼1	∼1–1.04	0–100	100–100
GW230920_071124	2886^{+1764}_{-1354}	$0.50^{+0.24}_{-0.21}$	2.0×10^3	3.7	0	16	∼1–∼1	∼1–∼1	100–100	100–100

Table 12 *continued*

Table 12 *(continued)*

Name	$D_{\rm L}$ [Mpc]	z^*	$\Delta\Omega$ [deg^2]	ΔV^* [Gpc^3]	$N_{\rm gal}^{\rm DES}$	$N_{\rm gal}^{\rm GLADE+}$	Under(over)$^{\rm DES}$	Under(over)$^{\rm GLADE+}$	Incompleteness$^{\rm DES}$ (%)	Incompleteness$^{\rm GLADE+}$ (%)
GW230922_020344	1581^{+740}_{-687}	$0.30^{+0.12}_{-0.12}$	316	0.13	0	901	∼1–∼1	∼1–1.04	100–100	100–100
GW230922_040658	6396^{+4111}_{-3466}	$0.95^{+0.47}_{-0.45}$	4.9×10^3	37	0	0	∼1–∼1	∼1–∼1	100–100	100–100
GW230924_124453	2395^{+1012}_{-1024}	$0.42^{+0.14}_{-0.16}$	1.2×10^3	1.1	4.1×10^4	157	0.89–∼1	∼1–∼1	0–100	100–100
GW230927_043729	3189^{+1807}_{-1649}	$0.54^{+0.24}_{-0.25}$	1.4×10^3	2.9	0	9	∼1–∼1	∼1–∼1	100–100	100–100
GW230927_153832	1209^{+368}_{-547}	$0.23^{+0.06}_{-0.10}$	344	0.06	7.9×10^4	1.2×10^3	0.80–0.88	∼1–1.06	0–0	98–100
GW230928_215827	4624^{+3958}_{-2291}	$0.73^{+0.48}_{-0.32}$	3.5×10^3	19	0	0	∼1–∼1	∼1–∼1	100–100	100–100
GW230930_110730	4883^{+3133}_{-2486}	$0.77^{+0.38}_{-0.34}$	3.2×10^3	16	0	0	∼1–∼1	∼1–∼1	100–100	100–100
GW231001_140220	4428^{+3910}_{-2401}	$0.71^{+0.47}_{-0.34}$	3.9×10^3	21	0	12	∼1–∼1	∼1–∼1	100–100	100–100
GW231004_232346	4260^{+3674}_{-2232}	$0.68^{+0.45}_{-0.32}$	3.4×10^3	17	0	0	∼1–∼1	∼1–∼1	100–100	100–100
GW231005_021030	6345^{+4760}_{-3242}	$0.95^{+0.54}_{-0.42}$	5.4×10^3	44	0	0	∼1–∼1	∼1–∼1	100–100	100–100
GW231005_091549	3713^{+2518}_{-1843}	$0.61^{+0.32}_{-0.27}$	2.6×10^3	8.2	0	10	∼1–∼1	∼1–∼1	100–100	100–100
GW231008_142521	3001^{+2587}_{-1369}	$0.51^{+0.34}_{-0.21}$	3.1×10^3	7.9	2.6×10^5	55	0.88–∼1	∼1–∼1	0–100	100–100
GW231014_040532	2289^{+1392}_{-1169}	$0.41^{+0.20}_{-0.19}$	1.7×10^3	1.9	0	582	∼1–∼1	∼1–1.01	100–100	100–100
GW231020_142947	1225^{+516}_{-642}	$0.24^{+0.09}_{-0.12}$	1.4×10^3	0.30	0	9.5×10^3	∼1–∼1	∼1–1.08	100–100	94–100
GW231028_153006	4484^{+1210}_{-1916}	$0.71^{+0.15}_{-0.26}$	1.3×10^3	2.9	0	0	∼1–∼1	∼1–∼1	100–100	100–100
GW231029_111508	3083^{+2431}_{-1662}	$0.52^{+0.32}_{-0.25}$	2.9×10^4	75	1.5×10^4	781	0.97–∼1	∼1–∼1	100–100	100–100
GW231102_071736	3782^{+2151}_{-1769}	$0.62^{+0.28}_{-0.26}$	2.7×10^3	7.6	0	49	∼1–∼1	∼1–∼1	100–100	100–100
GW231104_133418	1469^{+541}_{-658}	$0.28^{+0.09}_{-0.12}$	925	0.27	2.4×10^5	2.5×10^3	0.83–1.08	∼1–1.03	0–100	99–100
GW231108_125142	2058^{+741}_{-890}	$0.37^{+0.11}_{-0.14}$	1.0×10^3	0.61	1.2×10^5	305	0.82–∼1	∼1–1.00	0–100	100–100
GW231110_040320	1872^{+864}_{-902}	$0.34^{+0.13}_{-0.15}$	765	0.45	4.3×10^3	638	0.94–∼1	∼1–1.01	100–100	100–100
GW231113_200417	1160^{+643}_{-528}	$0.23^{+0.11}_{-0.10}$	1.6×10^3	0.37	0	6.7×10^3	∼1–∼1	∼1–1.04	100–100	96–100
GW231114_043211	1365^{+864}_{-606}	$0.26^{+0.14}_{-0.11}$	1.5×10^3	0.58	0	2.5×10^3	∼1–∼1	∼1–1.02	100–100	99–100
GW231118_005626	2139^{+948}_{-942}	$0.39^{+0.14}_{-0.15}$	1.0×10^3	0.76	0	195	∼1–∼1	∼1–1.01	100–100	100–100
GW231118_071402	4302^{+3540}_{-2287}	$0.69^{+0.43}_{-0.32}$	3.5×10^3	17	0	1	∼1–∼1	∼1–∼1	100–100	100–100
GW231118_090602	1372^{+539}_{-625}	$0.26^{+0.09}_{-0.11}$	1.1×10^3	0.28	4.5×10^4	2.0×10^3	0.82–1.05	∼1–1.03	0–1	99–100
GW231119_075248	6689^{+5315}_{-3728}	$0.99^{+0.60}_{-0.48}$	5.5×10^3	52	0	0	∼1–∼1	∼1–∼1	100–100	100–100
GW231127_165300	4455^{+3608}_{-2472}	$0.71^{+0.44}_{-0.35}$	4.1×10^3	21	0	12	∼1–∼1	∼1–∼1	100–100	100–100
GW231129_081745	3796^{+3666}_{-2105}	$0.62^{+0.46}_{-0.31}$	3.5×10^3	16	8.2×10^4	56	0.87–∼1	∼1–∼1	0–100	100–100
GW231206_233134	3310^{+1784}_{-1833}	$0.56^{+0.24}_{-0.28}$	2.3×10^3	5.0	0	26	∼1–∼1	∼1–∼1	100–100	100–100
GW231206_233901	1495^{+350}_{-501}	$0.28^{+0.06}_{-0.09}$	338	0.07	2.6×10^4	286	0.79–0.90	∼1–1.01	0–1	100–100
GW231213_111417	4046^{+2332}_{-2033}	$0.66^{+0.29}_{-0.29}$	2.3×10^3	7.5	0	26	∼1–∼1	∼1–∼1	100–100	100–100
GW231223_032836	4137^{+3100}_{-2105}	$0.67^{+0.39}_{-0.30}$	3.8×10^3	16	0	0	∼1–∼1	∼1–∼1	100–100	100–100
GW231223_202619	889^{+486}_{-441}	$0.18^{+0.09}_{-0.08}$	2.7×10^4	3.3	2.0×10^5	7.4×10^4	0.86–0.95	∼1–1.06	0–0	83–100
GW231224_024321	944^{+283}_{-399}	$0.19^{+0.05}_{-0.07}$	368	0.03	0	2.0×10^3	∼1–∼1	∼1–1.12	100–100	93–100
GW231226_101520	1187^{+237}_{-353}	$0.23^{+0.04}_{-0.06}$	196	0.02	0	473	∼1–∼1	∼1–1.02	100–100	100–100
GW231231_154016	1067^{+599}_{-526}	$0.21^{+0.10}_{-0.10}$	2.7×10^4	5.3	1.0×10^6	6.3×10^4	0.84–0.96	∼1–1.05	0–0	92–100
GW240104_164932	1927^{+1121}_{-971}	$0.35^{+0.17}_{-0.16}$	2.9×10^4	22	9.8×10^5	1.0×10^4	0.86–∼1	∼1–1.01	0–100	100–100

Table 12 *continued*

Table 12 *(continued)*

Name	D_{L} [Mpc]	z^*	$\Delta\Omega$ [deg^2]	ΔV^* [Gpc^3]	$N_{\mathrm{gal}}^{\mathrm{DES}}$	$N_{\mathrm{gal}}^{\mathrm{GLADE+}}$	Under(over)$^{\mathrm{DES}}$	Under(over)$^{\mathrm{GLADE+}}$	Incompleteness$^{\mathrm{DES}}$ (%)	Incompleteness$^{\mathrm{GLADE+}}$ (%)
GW240107_013215	5876^{+4954}_{-3391}	$0.89^{+0.57}_{-0.45}$	4.4×10^3	36	0	0	∼1–∼1	∼1–∼1	100–100	100–100
GW240109_050431	1495^{+1021}_{-770}	$0.28^{+0.16}_{-0.14}$	2.8×10^4	14	0	2.3×10^4	∼1–∼1	∼1–1.02	100–100	99–100
GW240413_022019	572^{+109}_{-217}	$0.12^{+0.02}_{-0.04}$	37	6.6×10^{-4}	0	294	∼1–∼1	0.95–1.21	100–100	70–99
GW240414_054515	1525^{+683}_{-581}	$0.29^{+0.11}_{-0.10}$	279	0.10	0	110	∼1–∼1	∼1–∼1	100–100	100–100
GW240420_175625	2031^{+1550}_{-1077}	$0.37^{+0.23}_{-0.18}$	2.8×10^4	31	0	6.7×10^3	∼1–∼1	∼1–1.01	100–100	100–100
GW240426_031451	4000^{+2609}_{-1970}	$0.65^{+0.33}_{-0.28}$	3.1×10^3	11	0	0	∼1–∼1	∼1–∼1	100–100	100–100
GW240428_225440	841^{+201}_{-284}	$0.17^{+0.04}_{-0.05}$	188	9.9×10^{-3}	0	1.0×10^3	∼1–∼1	1.01–1.08	100–100	93–100
GW240501_033534	4696^{+2675}_{-2198}	$0.74^{+0.33}_{-0.30}$	1.6×10^3	6.5	0	0	∼1–∼1	∼1–∼1	100–100	100–100
GW240505_133552	4693^{+2589}_{-2125}	$0.74^{+0.32}_{-0.29}$	2.0×10^3	7.8	0	0	∼1–∼1	∼1–∼1	100–100	100–100
GW240507_041632	1454^{+896}_{-501}	$0.28^{+0.14}_{-0.09}$	811	0.33	9.1×10^4	624	0.92–1.10	∼1–1.01	0–100	100–100
GW240511_031507	1991^{+746}_{-756}	$0.36^{+0.11}_{-0.12}$	119	0.07	0	18	∼1–∼1	∼1–∼1	100–100	100–100
GW240512_024139	1166^{+343}_{-485}	$0.23^{+0.06}_{-0.09}$	158	0.02	0	709	∼1–∼1	∼1–1.12	100–100	97–100
GW240513_183302	2247^{+687}_{-800}	$0.40^{+0.10}_{-0.13}$	37	0.02	0	0	∼1–∼1	∼1–∼1	100–100	100–100
GW240514_121713	2590^{+825}_{-1040}	$0.45^{+0.12}_{-0.16}$	193	0.17	1.4×10^5	8	0.84–∼1	∼1–∼1	0–100	100–100
GW240515_005301	3831^{+1839}_{-1900}	$0.63^{+0.24}_{-0.27}$	1.7×10^3	4.4	0	35	∼1–∼1	∼1–∼1	100–100	100–100
GW240519_012815	1743^{+1830}_{-820}	$0.32^{+0.27}_{-0.14}$	2.3×10^3	2.6	0	1.1×10^3	∼1–∼1	∼1–1.01	100–100	100–100
GW240520_213616	1402^{+525}_{-504}	$0.27^{+0.09}_{-0.09}$	373	0.09	246	447	0.91–∼1	∼1–1.03	100–100	100–100
GW240526_093944	1939^{+1103}_{-939}	$0.35^{+0.16}_{-0.16}$	996	0.76	0	301	∼1–∼1	∼1–∼1	100–100	100–100
GW240527_183429	6438^{+3473}_{-3089}	$0.96^{+0.40}_{-0.40}$	1.1×10^3	7.1	0	0	∼1–∼1	∼1–∼1	100–100	100–100
GW240527_230910	1193^{+325}_{-317}	$0.23^{+0.06}_{-0.06}$	20	2.5×10^{-3}	2.8×10^4	20	0.73–0.99	∼1–1.01	0–0	100–100
GW240530_012417	1007^{+634}_{-500}	$0.20^{+0.11}_{-0.09}$	579	0.11	2.7×10^4	4.8×10^3	0.72–0.95	∼1–1.07	0–1	89–100
GW240531_075248	4137^{+2792}_{-2236}	$0.67^{+0.35}_{-0.32}$	1.7×10^3	6.3	5.9×10^3	3	∼1–1.01	∼1–∼1	1–100	100–100
GW240601_061200	5086^{+4350}_{-2580}	$0.79^{+0.52}_{-0.35}$	2.4×10^3	16	0	0	∼1–∼1	∼1–∼1	100–100	100–100
GW240601_231004	1273^{+534}_{-537}	$0.25^{+0.09}_{-0.10}$	818	0.18	7.7×10^4	2.4×10^3	0.76–0.92	∼1–1.03	0–1	99–100
GW240615_113620	1565^{+294}_{-451}	$0.29^{+0.05}_{-0.08}$	7	1.3×10^{-3}	0	16	∼1–∼1	∼1–1.01	100–100	100–100
GW240615_160735	3971^{+1889}_{-1906}	$0.65^{+0.24}_{-0.27}$	1.1×10^3	3.1	0	0	∼1–∼1	∼1–∼1	100–100	100–100
GW240618_071627	5479^{+5112}_{-2909}	$0.84^{+0.59}_{-0.39}$	5.8×10^3	45	0	0	∼1–∼1	∼1–∼1	100–100	100–100
GW240621_195059	1208^{+256}_{-431}	$0.23^{+0.04}_{-0.08}$	33	4.1×10^{-3}	0	36	∼1–∼1	∼1–1.01	100–100	100–100
GW240621_200935	4788^{+2972}_{-2351}	$0.75^{+0.36}_{-0.32}$	1.6×10^3	7.3	0	0	∼1–∼1	∼1–∼1	100–100	100–100
GW240621_214041	6779^{+4791}_{-3433}	$1.00^{+0.54}_{-0.44}$	3.2×10^3	28	0	0	∼1–∼1	∼1–∼1	100–100	100–100
GW240622_004008	1472^{+598}_{-534}	$0.28^{+0.10}_{-0.09}$	247	0.07	0	664	∼1–∼1	∼1–1.05	100–100	100–100
GW240627_131622	1353^{+617}_{-572}	$0.26^{+0.10}_{-0.10}$	933	0.26	0	1.3×10^3	∼1–∼1	∼1–1.02	100–100	100–100
GW240629_145256	1275^{+339}_{-497}	$0.25^{+0.06}_{-0.09}$	281	0.05	0	418	∼1–∼1	∼1–1.04	100–100	100–100
GW240630_101703	3196^{+1535}_{-1363}	$0.54^{+0.21}_{-0.20}$	803	1.4	0	3	∼1–∼1	∼1–∼1	100–100	100–100
GW240703_191355	1882^{+1536}_{-856}	$0.34^{+0.23}_{-0.14}$	6.0×10^3	5.9	0	2.0×10^3	∼1–∼1	∼1–1.01	100–100	100–100
GW240705_053215	3734^{+1396}_{-1606}	$0.61^{+0.18}_{-0.23}$	287	0.57	0	0	∼1–∼1	∼1–∼1	100–100	100–100
GW240716_034900	1862^{+1388}_{-926}	$0.34^{+0.20}_{-0.15}$	1.1×10^4	9.5	6.7×10^5	4.8×10^3	0.84–∼1	∼1–1.01	0–100	100–100

Table 12 *continued*

Table 12 *(continued)*

Name	D_{L} [Mpc]	z^*	$\Delta\Omega$ [deg^2]	ΔV^* [Gpc^3]	$N_{\mathrm{gal}}^{\mathrm{DES}}$	$N_{\mathrm{gal}}^{\mathrm{GLADE+}}$	Under(over)$^{\mathrm{DES}}$	Under(over)$^{\mathrm{GLADE+}}$	Incompleteness$^{\mathrm{DES}}$ (%)	Incompleteness$^{\mathrm{GLADE+}}$ (%)
GW240824_205609	5277^{+5353}_{-3013}	$0.81^{+0.62}_{-0.41}$	2.6×10^3	21	0	0	∼1–∼1	∼1–∼1	100–100	100–100
GW240825_055146	1254^{+526}_{-547}	$0.24^{+0.09}_{-0.10}$	502	0.11	0	1.5×10^3	∼1–∼1	∼1–1.03	100–100	99–100
GW240830_211120	1143^{+499}_{-489}	$0.22^{+0.08}_{-0.09}$	511	0.09	9.9×10^4	2.6×10^3	0.83–0.98	∼1–1.05	0–0	97–100
GW240902_143306	2864^{+1733}_{-1328}	$0.49^{+0.24}_{-0.20}$	884	1.5	0	2	∼1–∼1	∼1–∼1	100–100	100–100
GW240907_153833	4483^{+3064}_{-2104}	$0.71^{+0.38}_{-0.29}$	1.6×10^3	6.8	0	0	∼1–∼1	∼1–∼1	100–100	100–100
GW240908_082628	3109^{+2573}_{-1314}	$0.53^{+0.34}_{-0.20}$	175	0.46	0	0	∼1–∼1	∼1–∼1	100–100	100–100
GW240910_103535	739^{+172}_{-312}	$0.15^{+0.03}_{-0.06}$	494	0.02	0	3.0×10^3	∼1–∼1	1.01–1.16	100–100	79–100
GW240915_001357	923^{+186}_{-289}	$0.18^{+0.03}_{-0.05}$	16	9.5×10^{-4}	0	36	∼1–∼1	∼1–1.01	100–100	98–100
GW240915_105151	630^{+256}_{-277}	$0.13^{+0.05}_{-0.06}$	5.2×10^3	0.21	0	2.4×10^4	∼1–∼1	1.01–1.10	100–100	68–100
GW240916_184352	1285^{+628}_{-637}	$0.25^{+0.10}_{-0.11}$	1.3×10^3	0.36	0	5.5×10^3	∼1–∼1	∼1–1.04	100–100	97–100
GW240919_061559	1869^{+819}_{-740}	$0.34^{+0.12}_{-0.12}$	25	0.01	0	12	∼1–∼1	∼1–∼1	100–100	100–100
GW240920_073424	1442^{+619}_{-548}	$0.27^{+0.10}_{-0.10}$	428	0.13	0	287	∼1–∼1	∼1–1.01	100–100	100–100
GW240920_124024	1091^{+216}_{-319}	$0.21^{+0.04}_{-0.06}$	158	0.01	0	443	∼1–∼1	∼1–1.15	100–100	99–100
GW240921_201835	918^{+765}_{-305}	$0.18^{+0.13}_{-0.06}$	1.9×10^3	0.38	0	6.6×10^3	∼1–∼1	∼1–1.05	100–100	95–100
GW240922_142106	1231^{+344}_{-498}	$0.24^{+0.06}_{-0.09}$	194	0.03	0	409	∼1–∼1	∼1–1.07	100–100	99–100
GW240923_204006	4025^{+1849}_{-1877}	$0.65^{+0.24}_{-0.27}$	453	1.2	0	0	∼1–∼1	∼1–∼1	100–100	100–100
GW240924_000316	3734^{+2633}_{-1737}	$0.61^{+0.34}_{-0.25}$	813	2.6	0	0	∼1–∼1	∼1–∼1	100–100	100–100
GW240925_005809	360^{+58}_{-166}	$0.08^{+0.01}_{-0.04}$	26	1.3×10^{-4}	0	0	∼1–∼1	∼1–∼1	100–100	100–100
GW240930_035959	954^{+488}_{-291}	$0.19^{+0.08}_{-0.05}$	361	0.05	0	720	∼1–∼1	∼1–1.03	100–100	98–100
GW240930_234614	3613^{+2558}_{-2002}	$0.60^{+0.33}_{-0.30}$	857	2.7	0	0	∼1–∼1	∼1–∼1	100–100	100–100
GW241002_030559	1456^{+947}_{-684}	$0.28^{+0.15}_{-0.12}$	697	0.32	1.7×10^5	1.5×10^3	0.80–∼1	∼1–1.02	0–100	99–100
GW241006_015333	1849^{+646}_{-710}	$0.34^{+0.10}_{-0.12}$	245	0.11	0	86	∼1–∼1	∼1–∼1	100–100	100–100
GW241007_082943	4035^{+2315}_{-2047}	$0.66^{+0.29}_{-0.29}$	957	3.1	0	0	∼1–∼1	∼1–∼1	100–100	100–100
GW241009_084816	1132^{+577}_{-482}	$0.22^{+0.10}_{-0.09}$	394	0.08	0	1.4×10^3	∼1–∼1	∼1–1.05	100–100	98–100
GW241009_220455	2932^{+2219}_{-1322}	$0.50^{+0.30}_{-0.20}$	76	0.17	0	0	∼1–∼1	∼1–∼1	100–100	100–100
GW241011_233834	212^{+43}_{-41}	$0.05^{+0.01}_{-0.01}$	50	4.9×10^{-5}	0	62	∼1–∼1	0.73–2.63	100–100	26–49
GW241101_220523	2179^{+1432}_{-1031}	$0.39^{+0.21}_{-0.17}$	7.7×10^3	8.4	1.6×10^4	1.4×10^3	0.94–1.02	∼1–∼1	100–100	100–100
GW241102_124058	390^{+59}_{-112}	$0.08^{+0.01}_{-0.02}$	23	1.2×10^{-4}	0	187	∼1–∼1	0.97–1.15	100–100	50–83
GW241102_144729	3446^{+1963}_{-1572}	$0.57^{+0.26}_{-0.23}$	873	2.0	3.4×10^3	13	0.90–∼1	∼1–∼1	1–100	100–100
GW241109_033317	2652^{+2036}_{-1520}	$0.46^{+0.28}_{-0.24}$	7.7×10^3	15	1.3×10^5	1.2×10^3	0.87–1.02	∼1–∼1	0–100	100–100
GW241109_115924	602^{+235}_{-288}	$0.12^{+0.04}_{-0.06}$	1.1×10^4	0.39	0	5.7×10^4	∼1–∼1	1.01–1.10	100–100	59–100
GW241110_124123	739^{+261}_{-256}	$0.15^{+0.05}_{-0.05}$	104	5.3×10^{-3}	0	892	∼1–∼1	∼1–1.16	100–100	89–100
GW241111_111552	1565^{+528}_{-742}	$0.29^{+0.08}_{-0.13}$	422	0.14	0	421	∼1–∼1	∼1–1.01	100–100	100–100
GW241113_163507	1355^{+667}_{-632}	$0.26^{+0.11}_{-0.11}$	1.3×10^4	4.1	1.2×10^6	2.6×10^4	0.84–∼1	∼1–1.03	0–100	98–100
GW241114_024711	2583^{+1590}_{-1010}	$0.45^{+0.22}_{-0.16}$	196	0.27	0	0	∼1–∼1	∼1–∼1	100–100	100–100
GW241114_235258	794^{+302}_{-347}	$0.16^{+0.05}_{-0.07}$	1.2×10^4	0.79	0	3.7×10^4	∼1–∼1	∼1–1.05	100–100	83–100
GW241116_151753	5738^{+5603}_{-2944}	$0.87^{+0.64}_{-0.39}$	3.4×10^3	29	0	0	∼1–∼1	∼1–∼1	100–100	100–100

Table 12 *continued*

Table 12 *(continued)*

Name	$D_{\rm L}$ [Mpc]	z^*	$\Delta\Omega$ [deg^2]	ΔV^* [Gpc^3]	$N_{\rm gal}^{\rm DES}$	$N_{\rm gal}^{\rm GLADE+}$	Under(over)$^{\rm DES}$	Under(over)$^{\rm GLADE+}$	Incompleteness$^{\rm DES}$ (%)	Incompleteness$^{\rm GLADE+}$ (%)
GW241125_010116	4722^{+3918}_{-2187}	$0.74^{+0.47}_{-0.30}$	2.4×10^3	13	0	0	$\sim$1–$\sim$1	$\sim$1–$\sim$1	100–100	100–100
GW241127_061008	1077^{+215}_{-177}	$0.21^{+0.04}_{-0.03}$	84	5.7×10^{-3}	0	44	$\sim$1–$\sim$1	$\sim$1–1.01	100–100	100–100
GW241129_021832	2552^{+742}_{-913}	$0.45^{+0.11}_{-0.14}$	354	0.27	0	0	$\sim$1–$\sim$1	$\sim$1–$\sim$1	100–100	100–100
GW241130_034908	1987^{+995}_{-928}	$0.36^{+0.15}_{-0.15}$	476	0.34	0	204	$\sim$1–$\sim$1	$\sim$1–$\sim$1	100–100	100–100
GW241130_110422	1315^{+527}_{-566}	$0.25^{+0.09}_{-0.10}$	1.3×10^3	0.31	0	3.0×10^3	$\sim$1–$\sim$1	$\sim$1–1.03	100–100	99–100
GW241210_060606	2596^{+1174}_{-1192}	$0.45^{+0.17}_{-0.19}$	959	1.1	0	21	$\sim$1–$\sim$1	$\sim$1–$\sim$1	100–100	100–100
GW241225_042553	664^{+192}_{-266}	$0.14^{+0.04}_{-0.05}$	3.8×10^3	0.13	0	5.9×10^3	$\sim$1–$\sim$1	1.01–1.07	100–100	80–100
GW241225_082815	1861^{+1099}_{-867}	$0.34^{+0.17}_{-0.14}$	966	0.69	0	664	$\sim$1–$\sim$1	$\sim$1–1.02	100–100	100–100
GW241229_155844	6777^{+5201}_{-3434}	$1.00^{+0.59}_{-0.44}$	3.4×10^3	31	0	0	$\sim$1–$\sim$1	$\sim$1–$\sim$1	100–100	100–100
GW241230_084504	2926^{+1396}_{-1337}	$0.50^{+0.19}_{-0.20}$	1.4×10^4	20	8.1×10^3	297	0.96–$\sim$1	$\sim$1–$\sim$1	100–100	100–100
GW241231_054133	914^{+187}_{-326}	$0.18^{+0.03}_{-0.06}$	131	7.9×10^{-3}	0	255	$\sim$1–$\sim$1	$\sim$1–1.01	100–100	97–100
GW250101_011205	3226^{+1743}_{-1525}	$0.54^{+0.23}_{-0.23}$	516	1.0	2.1×10^4	13	0.91–$\sim$1	$\sim$1–$\sim$1	0–100	100–100
GW250104_015122	4828^{+2503}_{-2308}	$0.76^{+0.31}_{-0.32}$	1.8×10^3	7.2	0	0	$\sim$1–$\sim$1	$\sim$1–$\sim$1	100–100	100–100
GW250108_152221	3839^{+2378}_{-1910}	$0.63^{+0.30}_{-0.28}$	820	2.5	0	0	$\sim$1–$\sim$1	$\sim$1–$\sim$1	100–100	100–100
GW250109_010541	3377^{+1693}_{-1680}	$0.56^{+0.22}_{-0.25}$	548	1.1	1.0×10^4	17	0.90–$\sim$1	$\sim$1–$\sim$1	2–100	100–100
GW250114_082203	405^{+84}_{-73}	$0.09^{+0.02}_{-0.01}$	41	2.4×10^{-4}	0	382	$\sim$1–$\sim$1	0.88–1.23	100–100	54–81
GW250116_015318	5159^{+3915}_{-2480}	$0.80^{+0.47}_{-0.33}$	2.9×10^3	17	0	0	$\sim$1–$\sim$1	$\sim$1–$\sim$1	100–100	100–100
GW250118_023225	5813^{+3814}_{-2928}	$0.88^{+0.45}_{-0.39}$	2.4×10^3	16	0	0	$\sim$1–$\sim$1	$\sim$1–$\sim$1	100–100	100–100
GW250118_055802	936^{+626}_{-380}	$0.19^{+0.11}_{-0.07}$	562	0.09	0	3.6×10^3	$\sim$1–$\sim$1	$\sim$1–1.11	100–100	93–100
GW250118_170523	1908^{+799}_{-741}	$0.35^{+0.12}_{-0.12}$	904	0.49	4.6×10^4	211	0.91–1.07	$\sim$1–$\sim$1	0–100	100–100
GW250119_025138	3078^{+1084}_{-1270}	$0.52^{+0.15}_{-0.19}$	555	0.73	0	9	$\sim$1–$\sim$1	$\sim$1–$\sim$1	100–100	100–100
GW250119_190238	311^{+289}_{-68}	$0.07^{+0.06}_{-0.01}$	14	2.0×10^{-4}	0	189	$\sim$1–$\sim$1	1.03–1.59	100–100	42–96

REFERENCES

Aasi, J., et al. 2015, Class. Quant. Grav., 32, 074001, doi: 10.1088/0264-9381/32/7/074001

Abac, A., et al. 2025a. https://arxiv.org/abs/2503.12263

Abac, A. G., Abouelfettouh, I., Acernese, F., et al. 2026a, To be published in this issue. https://dcc.ligo.org/LIGO-P2500701/public

—. 2026b, To be published in this issue. https://dcc.ligo.org/LIGO-P2600166/public

—. 2026c, To be published in this issue. https://dcc.ligo.org/LIGO-P2600152/public

—. 2026d, To be published in this issue

—. 2026e, To be published in this issue. https://dcc.ligo.org/LIGO-P2600045/public

—. 2026f, To be published in this issue. https://dcc.ligo.org/LIGO-P2600085/public

Abac, A. G., et al. 2024, Astrophys. J. Lett., 970, L34, doi: 10.3847/2041-8213/ad5beb

—. 2025b. https://arxiv.org/abs/2509.04348

—. 2025c. https://arxiv.org/abs/2508.18082

—. 2025d. https://arxiv.org/abs/2508.18083

—. 2025e, Astrophys. J. Lett., 993, L25, doi: 10.3847/2041-8213/ae0c9c

Abbott, B. P., et al. 2016, Phys. Rev. X, 6, 041015, doi: 10.1103/PhysRevX.6.041015

—. 2017a, Nature, 551, 85, doi: 10.1038/nature24471

—. 2017b, Phys. Rev. Lett., 119, 161101, doi: 10.1103/PhysRevLett.119.161101

—. 2017c, Astrophys. J. Lett., 848, L12, doi: 10.3847/2041-8213/aa91c9

—. 2017d, Astrophys. J. Lett., 848, L13, doi: 10.3847/2041-8213/aa920c

—. 2019, Phys. Rev. X, 9, 031040, doi: 10.1103/PhysRevX.9.031040

—. 2020, Astrophys. J. Lett., 892, L3, doi: 10.3847/2041-8213/ab75f5

—. 2021a, Astrophys. J., 909, 218, doi: 10.3847/1538-4357/abdcb7

Abbott, R., et al. 2021b, Phys. Rev. X, 11, 021053, doi: 10.1103/PhysRevX.11.021053

—. 2021c, Astrophys. J. Lett., 913, L7, doi: 10.3847/2041-8213/abe949

—. 2021d, Astrophys. J. Lett., 915, L5, doi: 10.3847/2041-8213/ac082e

—. 2023a, Astrophys. J., 949, 76, doi: 10.3847/1538-4357/ac74bb

—. 2023b, Phys. Rev. X, 13, 041039, doi: 10.1103/PhysRevX.13.041039

—. 2023c, Phys. Rev. X, 13, 011048, doi: 10.1103/PhysRevX.13.011048

—. 2024, Phys. Rev. D, 109, 022001, doi: 10.1103/PhysRevD.109.022001

Abbott, T., et al. 2005. https://arxiv.org/abs/astro-ph/0510346

Abdalla, E., et al. 2022, JHEAp, 34, 49, doi: 10.1016/j.jheap.2022.04.002

Acernese, F., et al. 2015, Class. Quant. Grav., 32, 024001, doi: 10.1088/0264-9381/32/2/024001

Adams, T., Buskulic, D., Germain, V., et al. 2016, Class. Quant. Grav., 33, 175012, doi: 10.1088/0264-9381/33/17/175012

Ade, P. A. R., et al. 2016, Astron. Astrophys., 594, A13, doi: 10.1051/0004-6361/201525830

Adhikari, S., Fishbach, M., Holz, D. E., Wechsler, R. H., & Fang, Z. 2020, Astrophys. J., 905, 21, doi: 10.3847/1538-4357/abbfb7

Afroz, S., & Mukherjee, S. 2024, Mon. Not. Roy. Astron. Soc., 534, 1283, doi: 10.1093/mnras/stae2139

Agarwal, A., et al. 2025, Astrophys. J., 987, 47, doi: 10.3847/1538-4357/adda3a

Aghamousa, A., et al. 2016. https://arxiv.org/abs/1611.00036

Aghanim, N., et al. 2020, Astron. Astrophys., 641, A6, doi: 10.1051/0004-6361/201833910

Akutsu, T., et al. 2021, PTEP, 2021, 05A101, doi: 10.1093/ptep/ptaa125

Alfradique, V., Bom, C. R., Teixeira, G., & Santos, A. 2026, Improved constraint on the Hubble constant from dark sirens with LIGO/Virgo/KAGRA O4a. https://arxiv.org/abs/2603.20195

Alfradique, V., Bom, C. R., Palmese, A., et al. 2024, Mon. Not. Roy. Astron. Soc., 528, 3249, doi: 10.1093/mnras/stae086

Allen, B., Anderson, W. G., Brady, P. R., Brown, D. A., & Creighton, J. D. E. 2012, Phys. Rev. D, 85, 122006, doi: 10.1103/PhysRevD.85.122006

Alléné, C., et al. 2025, Class. Quant. Grav., 42, 105009, doi: 10.1088/1361-6382/add234

Amendola, L., Sawicki, I., Kunz, M., & Saltas, I. D. 2018, JCAP, 08, 030, doi: 10.1088/1475-7516/2018/08/030

Artale, M. C., Mapelli, M., Giacobbo, N., et al. 2019, Mon. Not. Roy. Astron. Soc., 487, 1675, doi: 10.1093/mnras/stz1382

Ashton, G., et al. 2019, Astrophys. J. Suppl., 241, 27, doi: 10.3847/1538-4365/ab06fc

Aubin, F., et al. 2021, Class. Quant. Grav., 38, 095004, doi: 10.1088/1361-6382/abe913

Baker, T., & Harrison, I. 2021, JCAP, 01, 068, doi: 10.1088/1475-7516/2021/01/068

Bechtol, K., et al. 2025. https://arxiv.org/abs/2501.05739

Belczynski, K., Bulik, T., & Fryer, C. L. 2012. https://arxiv.org/abs/1208.2422

Belgacem, E., Dirian, Y., Foffa, S., et al. 2019a, JCAP, 08, 015, doi: 10.1088/1475-7516/2019/08/015

Belgacem, E., Dirian, Y., Foffa, S., & Maggiore, M. 2018a, Phys. Rev. D, 98, 023510, doi: 10.1103/PhysRevD.98.023510

—. 2018b, Phys. Rev. D, 97, 104066, doi: 10.1103/PhysRevD.97.104066

Belgacem, E., et al. 2019b, JCAP, 07, 024, doi: 10.1088/1475-7516/2019/07/024

Bellini, E., Cuesta, A. J., Jimenez, R., & Verde, L. 2016, JCAP, 02, 053, doi: 10.1088/1475-7516/2016/06/E01

Bellini, E., & Sawicki, I. 2014, JCAP, 07, 050, doi: 10.1088/1475-7516/2014/07/050

Beltran Jimenez, J., Piazza, F., & Velten, H. 2016, Phys. Rev. Lett., 116, 061101, doi: 10.1103/PhysRevLett.116.061101

Bilicki, M., Jarrett, T. H., Peacock, J. A., Cluver, M. E., & Steward, L. 2014, Astrophys. J. Suppl., 210, 9, doi: 10.1088/0067-0049/210/1/9

Bilicki, M., et al. 2016, Astrophys. J. Suppl., 225, 5, doi: 10.3847/0067-0049/225/1/5

Biscoveanu, S., Callister, T. A., Haster, C.-J., et al. 2022, Astrophys. J. Lett., 932, L19, doi: 10.3847/2041-8213/ac71a8

Bom, C. R., Alfradique, V., Palmese, A., et al. 2024, Mon. Not. Roy. Astron. Soc., 535, 961, doi: 10.1093/mnras/stae2390

Borghi, N., Mancarella, M., Moresco, M., et al. 2024, Astrophys. J., 964, 191, doi: 10.3847/1538-4357/ad20eb

Borghi, N., Moresco, M., Tagliazucchi, M., & Cuomo, G. 2026, Astron. Astrophys., 706, A199, doi: 10.1051/0004-6361/202557354

Branchesi, M., et al. 2023, JCAP, 07, 068, doi: 10.1088/1475-7516/2023/07/068

Broekgaarden, F. S., et al. 2022, Mon. Not. Roy. Astron. Soc., 516, 5737, doi: 10.1093/mnras/stac1677

Bull, P., et al. 2016, Phys. Dark Univ., 12, 56, doi: 10.1016/j.dark.2016.02.001

Camera, S., & Nishizawa, A. 2013, Phys. Rev. Lett., 110, 151103, doi: 10.1103/PhysRevLett.110.151103

Cannon, K., et al. 2020. https://arxiv.org/abs/2010.05082

Chatterjee, D., Hegade K R, A., Holder, G., et al. 2021, Phys. Rev. D, 104, 083528, doi: 10.1103/PhysRevD.104.083528

Chen, A., Gray, R., & Baker, T. 2024a, JCAP, 02, 035, doi: 10.1088/1475-7516/2024/02/035

Chen, H.-Y. 2020, Phys. Rev. Lett., 125, 201301, doi: 10.1103/PhysRevLett.125.201301

Chen, H.-Y., Ezquiaga, J. M., & Gupta, I. 2024b, Class. Quant. Grav., 41, 125004, doi: 10.1088/1361-6382/ad424f

Chen, H.-Y., Fishbach, M., & Holz, D. E. 2018, Nature, 562, 545, doi: 10.1038/s41586-018-0606-0

Chen, H.-Y., Talbot, C., & Chase, E. A. 2024c, Phys. Rev. Lett., 132, 191003, doi: 10.1103/PhysRevLett.132.191003

Chen, T., & Guestrin, C. 2016, doi: 10.1145/2939672.2939785

Cheng, A. Q., & Gair, J. 2026, A unified harmonic framework for dark siren cosmology. https://arxiv.org/abs/2603.13053

Chernoff, D. F., & Finn, L. S. 1993, Astrophys. J. Lett., 411, L5, doi: 10.1086/186898

Chilingarian, I. V., Melchior, A.-L., & Zolotukhin, I. Y. 2010, MNRAS, 405, 1409, doi: 10.1111/j.1365-2966.2010.16506.x

Clifton, T., Ferreira, P. G., Padilla, A., & Skordis, C. 2012, Phys. Rept., 513, 1, doi: 10.1016/j.physrep.2012.01.001

Colleoni, M., Vidal, F. A. R., García-Quirós, C., Akçay, S., & Bera, S. 2025, Phys. Rev. D, 111, 104019, doi: 10.1103/PhysRevD.111.104019

Cornish, N. J., & Littenberg, T. B. 2015, Class. Quant. Grav., 32, 135012, doi: 10.1088/0264-9381/32/13/135012

Cornish, N. J., Littenberg, T. B., Bécsy, B., et al. 2021, Phys. Rev. D, 103, 044006, doi: 10.1103/PhysRevD.103.044006

Cross-Parkin, M. L., Howlett, C., Davis, T. M., & Khetan, N. 2025, Dark sirens and the impact of redshift precision. https://arxiv.org/abs/2502.17747

Dal Canton, T., et al. 2014, Phys. Rev. D, 90, 082004, doi: 10.1103/PhysRevD.90.082004

Dalal, N., Holz, D. E., Hughes, S. A., & Jain, B. 2006, Phys. Rev. D, 74, 063006, doi: 10.1103/PhysRevD.74.063006

Dalang, C., & Baker, T. 2024, JCAP, 02, 024, doi: 10.1088/1475-7516/2024/02/024

Dalang, C., Fiorini, B., & Baker, T. 2024. https://arxiv.org/abs/2410.03275

Dálya, G., Galgóczi, G., Dobos, L., et al. 2018, Mon. Not. Roy. Astron. Soc., 479, 2374, doi: 10.1093/mnras/sty1703

Dálya, G., et al. 2022, Mon. Not. Roy. Astron. Soc., 514, 1403, doi: 10.1093/mnras/stac1443

Davies, G. S., Dent, T., Tápai, M., et al. 2020, Phys. Rev. D, 102, 022004, doi: 10.1103/PhysRevD.102.022004

Deffayet, C., Gao, X., Steer, D. A., & Zahariade, G. 2011, Phys. Rev. D, 84, 064039, doi: 10.1103/PhysRevD.84.064039

Del Pozzo, W. 2012, Phys. Rev. D, 86, 043011, doi: 10.1103/PhysRevD.86.043011

Del Pozzo, W., Li, T. G. F., & Messenger, C. 2017, Phys. Rev. D, 95, 043502, doi: 10.1103/PhysRevD.95.043502

Dhani, A., Völkel, S. H., Buonanno, A., et al. 2025, Phys. Rev. X, 15, 031036, doi: 10.1103/5pks-qz6b

Di Valentino, E., & Brout, D., eds. 2024, The Hubble Constant Tension, Springer Series in Astrophysics and Cosmology (Springer), doi: 10.1007/978-981-99-0177-7

Di Valentino, E., et al. 2025, Phys. Dark Univ., 49, 101965, doi: 10.1016/j.dark.2025.101965

Dietrich, T., Bernuzzi, S., & Tichy, W. 2017, Phys. Rev. D, 96, 121501, doi: 10.1103/PhysRevD.96.121501

Dietrich, T., et al. 2019, Phys. Rev. D, 99, 024029, doi: 10.1103/PhysRevD.99.024029

Ding, X., Biesiada, M., Zheng, X., et al. 2019, JCAP, 04, 033, doi: 10.1088/1475-7516/2019/04/033

Essick, R., Godwin, P., Hanna, C., Blackburn, L., & Katsavounidis, E. 2020, Machine Learning: Science and Technology, 2, 015004, doi: 10.1088/2632-2153/abab5f

Essick, R., Vitale, S., Katsavounidis, E., Vedovato, G., & Klimenko, S. 2015, Astrophys. J., 800, 81, doi: 10.1088/0004-637X/800/2/81

Essick, R., et al. 2025, In preparation

Ezquiaga, J. M. 2021, Phys. Lett. B, 822, 136665, doi: 10.1016/j.physletb.2021.136665

Ezquiaga, J. M., & Holz, D. E. 2021, Astrophys. J. Lett., 909, L23, doi: 10.3847/2041-8213/abe638

—. 2022, Phys. Rev. Lett., 129, 061102, doi: 10.1103/PhysRevLett.129.061102

Farah, A. M., Callister, T. A., Ezquiaga, J. M., Zevin, M., & Holz, D. E. 2025, Astrophys. J., 978, 153, doi: 10.3847/1538-4357/ad9253

Farah, A. M., Fishbach, M., Essick, R., Holz, D. E., & Galaudage, S. 2022, Astrophys. J., 931, 108, doi: 10.3847/1538-4357/ac5f03

Farr, W. M., Fishbach, M., Ye, J., & Holz, D. 2019, Astrophys. J. Lett., 883, L42, doi: 10.3847/2041-8213/ab4284

Farr, W. M., Sravan, N., Cantrell, A., et al. 2011, Astrophys. J., 741, 103, doi: 10.1088/0004-637X/741/2/103

Feeney, S. M., Peiris, H. V., Williamson, A. R., et al. 2019, Phys. Rev. Lett., 122, 061105, doi: 10.1103/PhysRevLett.122.061105

Ferri, J. a., Tashiro, I. L., Abramo, L. R., et al. 2024. https://arxiv.org/abs/2412.00202

Finke, A., Foffa, S., Iacovelli, F., Maggiore, M., & Mancarella, M. 2021a, JCAP, 08, 026, doi: 10.1088/1475-7516/2021/08/026

—. 2021b, Phys. Rev. D, 104, 084057, doi: 10.1103/PhysRevD.104.084057

—. 2022, Phys. Dark Univ., 36, 100994, doi: 10.1016/j.dark.2022.100994

Fishbach, M., Essick, R., & Holz, D. E. 2020, Astrophys. J. Lett., 899, L8, doi: 10.3847/2041-8213/aba7b6

Fishbach, M., & Holz, D. E. 2020, Astrophys. J. Lett., 891, L27, doi: 10.3847/2041-8213/ab7247

Fishbach, M., et al. 2019, Astrophys. J. Lett., 871, L13, doi: 10.3847/2041-8213/aaf96e

Fisher, R. P., Hemming, G., Bizouard, M.-A., et al. 2020. https://arxiv.org/abs/2008.11316

Fonseca, J., Zazzera, S., Baker, T., & Clarkson, C. 2023, JCAP, 08, 050, doi: 10.1088/1475-7516/2023/08/050

Fryer, C. L., Belczynski, K., Wiktorowicz, G., et al. 2012, Astrophys. J., 749, 91, doi: 10.1088/0004-637X/749/1/91

Gair, J. R., et al. 2023, Astron. J., 166, 22, doi: 10.3847/1538-3881/acca78

Gennari, V., Mastrogiovanni, S., Tamanini, N., Marsat, S., & Pierra, G. 2025. https://arxiv.org/abs/2502.20445

Gleyzes, J., Langlois, D., & Vernizzi, F. 2015, Int. J. Mod. Phys. D, 23, 1443010, doi: 10.1142/S021827181443010X

Górski, K. M., Hivon, E., Banday, A. J., et al. 2005, Astrophys. J., 622, 759, doi: 10.1086/427976

Gray, R., Messenger, C., & Veitch, J. 2022, Mon. Not. Roy. Astron. Soc., 512, 1127, doi: 10.1093/mnras/stac366

Gray, R., et al. 2020, Phys. Rev. D, 101, 122001, doi: 10.1103/PhysRevD.101.122001

—. 2023, JCAP, 12, 023, doi: 10.1088/1475-7516/2023/12/023

Hanna, C., et al. 2020, Phys. Rev. D, 101, 022003, doi: 10.1103/PhysRevD.101.022003

Hanselman, A. G., Vijaykumar, A., Fishbach, M., & Holz, D. E. 2025, Astrophys. J., 979, 9, doi: 10.3847/1538-4357/ad9393

Harris, C. R., et al. 2020, Nature, 585, 357, doi: 10.1038/s41586-020-2649-2

Heinzel, J., Mould, M., & Vitale, S. 2025, Phys. Rev. D, 111, L061305, doi: 10.1103/PhysRevD.111.L061305

Holz, D. E., & Hughes, S. A. 2005, Astrophys. J., 629, 15, doi: 10.1086/431341

Horndeski, G. W. 1974, Int. J. Theor. Phys., 10, 363, doi: 10.1007/BF01807638

Hoy, C., & Raymond, V. 2021, SoftwareX, 15, 100765, doi: 10.1016/j.softx.2021.100765

Hunter, J. D. 2007, Comput. Sci. Eng., 9, 90, doi: 10.1109/MCSE.2007.55

Ishak, M., et al. 2024. https://arxiv.org/abs/2411.12026

Ivezić, v., et al. 2019, Astrophys. J., 873, 111, doi: 10.3847/1538-4357/ab042c

Jasche, J., & Wandelt, B. D. 2013, Mon. Not. Roy. Astron. Soc., 432, 894, doi: 10.1093/mnras/stt449

John Zweizig. 2006, The Data Monitor Tool Project, labcit.ligo.caltech.edu/~jzweizig/DMT-Project.html

Joshi, P., et al. 2025. https://arxiv.org/abs/2506.06497

Kalogera, V., et al. 2021. https://arxiv.org/abs/2111.06990

Kapil, V., Reali, L., Cotesta, R., & Berti, E. 2024, Phys. Rev. D, 109, 104043, doi: 10.1103/PhysRevD.109.104043

Karathanasis, C., Mukherjee, S., & Mastrogiovanni, S. 2023, Mon. Not. Roy. Astron. Soc., 523, 4539, doi: 10.1093/mnras/stad1373

Klimenko, S., & Mitselmakher, G. 2004, Class. Quant. Grav., 21, S1819, doi: 10.1088/0264-9381/21/20/025

Klimenko, S., Mohanty, S., Rakhmanov, M., & Mitselmakher, G. 2005, Phys. Rev. D, 72, 122002, doi: 10.1103/PhysRevD.72.122002

Klimenko, S., Yakushin, I., Mercer, A., & Mitselmakher, G. 2008, Class. Quant. Grav., 25, 114029, doi: 10.1088/0264-9381/25/11/114029

Klimenko, S., Vedovato, G., Drago, M., et al. 2011, Phys. Rev. D, 83, 102001, doi: 10.1103/PhysRevD.83.102001

Klimenko, S., et al. 2016, Phys. Rev. D, 93, 042004, doi: 10.1103/PhysRevD.93.042004

Kobayashi, T. 2019, Rept. Prog. Phys., 82, 086901, doi: 10.1088/1361-6633/ab2429

Kobayashi, T., Yamaguchi, M., & Yokoyama, J. 2011, Prog. Theor. Phys., 126, 511, doi: 10.1143/PTP.126.511

Krolak, A., & Schutz, B. F. 1987, Gen. Rel. Grav., 19, 1163, doi: 10.1007/BF00759095

Lagos, M., Fishbach, M., Landry, P., & Holz, D. E. 2019, Phys. Rev. D, 99, 083504, doi: 10.1103/PhysRevD.99.083504

Lalleman, M., Turbang, K., Callister, T., & van Remortel, N. 2025. https://arxiv.org/abs/2501.10295

Laureijs, R., et al. 2011. https://arxiv.org/abs/1110.3193

Leyde, K., Baker, T., & Enzi, W. 2024, JCAP, 12, 013, doi: 10.1088/1475-7516/2024/12/013

—. 2025. https://arxiv.org/abs/2507.12171

Leyde, K., Mastrogiovanni, S., Steer, D. A., Chassande-Mottin, E., & Karathanasis, C. 2022, JCAP, 09, 012, doi: 10.1088/1475-7516/2022/09/012

Li, Y.-J., Tang, S.-P., Wang, Y.-Z., & Fan, Y.-Z. 2024a, Astrophys. J., 976, 153, doi: 10.3847/1538-4357/ad888b

Li, Y.-J., Wang, Y.-Z., Tang, S.-P., Chen, T., & Fan, Y.-Z. 2025a, Astrophys. J., 987, 65, doi: 10.3847/1538-4357/add535

Li, Y.-J., Wang, Y.-Z., Tang, S.-P., & Fan, Y.-Z. 2024b, Phys. Rev. Lett., 133, 051401, doi: 10.1103/PhysRevLett.133.051401

Li, Z., Gray, R., & Heng, I. S. 2025b, Using gravitational wave dark sirens to choose between host galaxy weighting models. https://arxiv.org/abs/2508.15574

LIGO Scientific Collaboration, Virgo Collaboration, & KAGRA Collaboration. 2018, LVK Algorithm Llibrary - LALSuite, Free software (GPL), doi: 10.7935/GT1W-FZ16

LIGO Scientific Collaboration, VIRGO Collaboration, & KAGRA Collaboration. 2026, GWTC-5.0: Constraints on the Cosmic Expansion Rate and Modified Gravitational-wave Propagation, Zenodo, doi: 10.5281/zenodo.20378418

LIGO Scientific Collaboration and Virgo Collaboration. 2018, Data quality report user documentation, docs.ligo.org/detchar/data-quality-report/

Littenberg, T. B., Kanner, J. B., Cornish, N. J., & Millhouse, M. 2016, Phys. Rev. D, 94, 044050, doi: 10.1103/PhysRevD.94.044050

Liu, C., Laghi, D., & Tamanini, N. 2024, Phys. Rev. D, 109, 063521, doi: 10.1103/PhysRevD.109.063521

Loredo, T. J. 2004, AIP Conf. Proc., 735, 195, doi: 10.1063/1.1835214

Lyke, B. W., et al. 2020, Astrophys. J. Suppl., 250, 8, doi: 10.3847/1538-4365/aba623

MacLeod, C. L., & Hogan, C. J. 2008, Phys. Rev. D, 77, 043512, doi: 10.1103/PhysRevD.77.043512

Macleod, D. M., Areeda, J. S., Coughlin, S. B., Massinger, T. J., & Urban, A. L. 2021, SoftwareX, 13, 100657, doi: 10.1016/j.softx.2021.100657

Madau, P., & Dickinson, M. 2014, Ann. Rev. Astron. Astrophys., 52, 415, doi: 10.1146/annurev-astro-081811-125615

Makarov, D., Prugniel, P., Terekhova, N., Courtois, H., & Vauglin, I. 2014, Astron. Astrophys., 570, A13, doi: 10.1051/0004-6361/201423496

Mali, U., & Essick, R. 2025a, Astrophys. J., 980, 85, doi: 10.3847/1538-4357/ad9de7

—. 2025b, The Astrophysical Journal, 980, 85, doi: 10.3847/1538-4357/ad9de7

Mancarella, M., Genoud-Prachex, E., & Maggiore, M. 2022, Phys. Rev. D, 105, 064030, doi: 10.1103/PhysRevD.105.064030

Mancarella, M., Iacovelli, F., Foffa, S., Muttoni, N., & Maggiore, M. 2024, Phys. Rev. Lett., 133, 261001, doi: 10.1103/PhysRevLett.133.261001

Mandel, I., Farr, W. M., & Gair, J. R. 2019, Mon. Not. Roy. Astron. Soc., 486, 1086, doi: 10.1093/mnras/stz896

Markovic, D. 1993, Phys. Rev. D, 48, 4738, doi: 10.1103/PhysRevD.48.4738

Mastrogiovanni, S., Leyde, K., Karathanasis, C., et al. 2021, Phys. Rev. D, 104, 062009, doi: 10.1103/PhysRevD.104.062009

Mastrogiovanni, S., Laghi, D., Gray, R., et al. 2023, Phys. Rev. D, 108, 042002, doi: 10.1103/PhysRevD.108.042002

Mastrogiovanni, S., Pierra, G., Perriès, S., et al. 2024, Astron. Astrophys., 682, A167, doi: 10.1051/0004-6361/202347007

McMahon, I., Laghi, D., Soares-Santos, M., et al. 2026, Measurement of the Hubble constant using the Dark Energy Survey Year 6 Gold galaxy catalog and the fourth Gravitational-Wave Transient Catalog. https://arxiv.org/abs/2602.04766

Mellier, Y., et al. 2025, Astron. Astrophys., 697, A1, doi: 10.1051/0004-6361/202450810

Messenger, C., & Read, J. 2012, Phys. Rev. Lett., 108, 091101, doi: 10.1103/PhysRevLett.108.091101

Messick, C., et al. 2017, Phys. Rev. D, 95, 042001, doi: 10.1103/PhysRevD.95.042001

Mishra, T., Bhaumik, S., Gayathri, V., et al. 2025, Phys. Rev. D, 111, 023054, doi: 10.1103/PhysRevD.111.023054

Mukherjee, S. 2022, Mon. Not. Roy. Astron. Soc., 515, 5495, doi: 10.1093/mnras/stac2152

Mukherjee, S., Krolewski, A., Wandelt, B. D., & Silk, J. 2024, Astrophys. J., 975, 189, doi: 10.3847/1538-4357/ad7d90

Mukherjee, S., Lavaux, G., Bouchet, F. R., et al. 2021a, Astron. Astrophys., 646, A65, doi: 10.1051/0004-6361/201936724

Mukherjee, S., Wandelt, B. D., Nissanke, S. M., & Silvestri, A. 2021b, Phys. Rev. D, 103, 043520, doi: 10.1103/PhysRevD.103.043520

Mukherjee, S., Wandelt, B. D., & Silk, J. 2020, Mon. Not. Roy. Astron. Soc., 494, 1956, doi: 10.1093/mnras/staa827

—. 2021c, Mon. Not. Roy. Astron. Soc., 502, 1136, doi: 10.1093/mnras/stab001

Müller, M., Mukherjee, S., & Ryan, G. 2024, Astrophys. J. Lett., 977, L45, doi: 10.3847/2041-8213/ad8dd1

Neijssel, C. J., Vigna-Gómez, A., Stevenson, S., et al. 2019, Mon. Not. Roy. Astron. Soc., 490, 3740, doi: 10.1093/mnras/stz2840

Nishizawa, A. 2017, Phys. Rev. D, 96, 101303, doi: 10.1103/PhysRevD.96.101303

—. 2018, Phys. Rev. D, 97, 104037, doi: 10.1103/PhysRevD.97.104037

Nissanke, S., Holz, D. E., Dalal, N., et al. 2013. https://arxiv.org/abs/1307.2638

Nissanke, S., Holz, D. E., Hughes, S. A., Dalal, N., & Sievers, J. L. 2010, Astrophys. J., 725, 496, doi: 10.1088/0004-637X/725/1/496

Nitz, A. H., Dent, T., Dal Canton, T., Fairhurst, S., & Brown, D. A. 2017, Astrophys. J., 849, 118, doi: 10.3847/1538-4357/aa8f50

Noller, J., & Nicola, A. 2019, Phys. Rev. D, 99, 103502, doi: 10.1103/PhysRevD.99.103502

Oguri, M. 2016, Phys. Rev. D, 93, 083511, doi: 10.1103/PhysRevD.93.083511

O'Shaughnessy, R., Bellovary, J. M., Brooks, A., et al. 2017, Mon. Not. Roy. Astron. Soc., 464, 2831, doi: 10.1093/mnras/stw2550

Ouzriat, A., Sordini, V., & Di Renzo, F. 2025, Characterizing Low-Latency Sky Localization in Multi-Detector Gravitational-Wave Networks. https://arxiv.org/abs/2510.21930

Ozel, F., Psaltis, D., Narayan, R., & McClintock, J. E. 2010, Astrophys. J., 725, 1918, doi: 10.1088/0004-637X/725/2/1918

Palmese, A., et al. 2020, Astrophys. J. Lett., 900, L33, doi: 10.3847/2041-8213/abaeff

Papadopoulos, A., Chapman-Bird, C. E. A., Gray, R., Messenger, C., & Bertheas, T. 2026. https://arxiv.org/abs/2605.23538

Pedrotti, A., Mancarella, M., Bel, J., & Gerosa, D. 2025. https://arxiv.org/abs/2504.10482

Perenon, L., Piazza, F., Marinoni, C., & Hui, L. 2015, JCAP, 11, 029, doi: 10.1088/1475-7516/2015/11/029

Perivolaropoulos, L., & Skara, F. 2022, New Astron. Rev., 95, 101659, doi: 10.1016/j.newar.2022.101659

Perna, G., Mastrogiovanni, S., & Ricciardone, A. 2024. https://arxiv.org/abs/2405.07904

Pettorino, V., & Amendola, L. 2015, Phys. Lett. B, 742, 353, doi: 10.1016/j.physletb.2015.02.007

Pierra, G., Mastrogiovanni, S., & Perriès, S. 2024a, Astron. Astrophys., 692, A80, doi: 10.1051/0004-6361/202452545

Pierra, G., Mastrogiovanni, S., Perriès, S., & Mapelli, M. 2024b, Phys. Rev. D, 109, 083504, doi: 10.1103/PhysRevD.109.083504

Pierra, G., & Papadopoulos, A. 2026, Heavy Black-Holes Also Matter in Standard Siren Cosmology. https://arxiv.org/abs/2601.03257

Pratten, G., et al. 2021, Phys. Rev. D, 103, 104056, doi: 10.1103/PhysRevD.103.104056

Rauf, L., Howlett, C., Davis, T. M., & Lagos, C. D. P. 2023, Mon. Not. Roy. Astron. Soc., 523, 5719, doi: 10.1093/mnras/stad1757

Renk, J., Zumalacárregui, M., Montanari, F., & Barreira, A. 2017, JCAP, 10, 020, doi: 10.1088/1475-7516/2017/10/020

Riess, A. G., Casertano, S., Yuan, W., et al. 2021, Astrophys. J. Lett., 908, L6, doi: 10.3847/2041-8213/abdbaf

Riess, A. G., et al. 2022, Astrophys. J. Lett., 934, L7, doi: 10.3847/2041-8213/ac5c5b

Rinaldi, S., Del Pozzo, W., Mapelli, M., Lorenzo-Medina, A., & Dent, T. 2024, Astron. Astrophys., 684, A204, doi: 10.1051/0004-6361/202348161

Robinet, F., Arnaud, N., Leroy, N., et al. 2020, SoftwareX, 12, 100620, doi: 10.1016/j.softx.2020.100620

Romano, A. E. 2025, Phys. Rev. D, 112, 124088, doi: 10.1103/y884-s66d

Romero-Shaw, I. M., et al. 2020, Mon. Not. Roy. Astron. Soc., 499, 3295, doi: 10.1093/mnras/staa2850

Roy, S. K., van Son, L. A. C., Ray, A., & Farr, W. M. 2025, Astrophys. J. Lett., 985, L33, doi: 10.3847/2041-8213/add34a

Sachdev, S., et al. 2019. https://arxiv.org/abs/1901.08580

Sakon, S., et al. 2024, Phys. Rev. D, 109, 044066, doi: 10.1103/PhysRevD.109.044066

Saltas, I. D., Sawicki, I., Amendola, L., & Kunz, M. 2014, Phys. Rev. Lett., 113, 191101, doi: 10.1103/PhysRevLett.113.191101

Salvarese, A., & Chen, H.-Y. 2024, Astrophys. J. Lett., 974, L16, doi: 10.3847/2041-8213/ad7bbc

Santoliquido, F., Mapelli, M., Giacobbo, N., Bouffanais, Y., & Artale, M. C. 2021, Mon. Not. Roy. Astron. Soc., 502, 4877, doi: 10.1093/mnras/stab280

Schechter, P. 1976, Astrophys. J., 203, 297, doi: 10.1086/154079

Schutz, B. F. 1986, Nature, 323, 310, doi: 10.1038/323310a0

Seraille, E., Noller, J., & Sherwin, B. D. 2024, Phys. Rev. D, 110, 123525, doi: 10.1103/PhysRevD.110.123525

Skrutskie, M. F., et al. 2006, Astron. J., 131, 1163, doi: 10.1086/498708

Smith, J. R., Abbott, T., Hirose, E., et al. 2011, Class. Quant. Grav., 28, 235005, doi: 10.1088/0264-9381/28/23/235005

Soares-Santos, M., et al. 2019, Astrophys. J. Lett., 876, L7, doi: 10.3847/2041-8213/ab14f1

Speagle, J. S. 2020, Mon. Not. Roy. Astron. Soc., 493, 3132, doi: 10.1093/mnras/staa278

Srinivasan, R., Lamberts, A., Bizouard, M. A., Bruel, T., & Mastrogiovanni, S. 2023, Mon. Not. Roy. Astron. Soc., 524, 60, doi: 10.1093/mnras/stad1825

Talbot, C., & Golomb, J. 2023, Mon. Not. Roy. Astron. Soc., 526, 3495, doi: 10.1093/mnras/stad2968

Taylor, S. R., Gair, J. R., & Mandel, I. 2012, Phys. Rev. D, 85, 023535, doi: 10.1103/PhysRevD.85.023535

Thrane, E., & Talbot, C. 2019, Publ. Astron. Soc. Austral., 36, e010, doi: 10.1017/pasa.2019.2

Tong, H., Fishbach, M., & Thrane, E. 2025. https://arxiv.org/abs/2502.10780

Tsukada, L., et al. 2023, Phys. Rev. D, 108, 043004, doi: 10.1103/PhysRevD.108.043004

Turski, C., Bilicki, M., Dálya, G., Gray, R., & Ghosh, A. 2023, Mon. Not. Roy. Astron. Soc., 526, 6224, doi: 10.1093/mnras/stad3110

Urban, A. L., et al. 2021, gwdetchar/gwdetchar, doi.org/10.5281/zenodo.2575786, Zenodo, doi: 10.5281/zenodo.597016

Usman, S. A., et al. 2016, Class. Quant. Grav., 33, 215004, doi: 10.1088/0264-9381/33/21/215004

Viets, A., et al. 2018, Class. Quant. Grav., 35, 095015, doi: 10.1088/1361-6382/aab658

Vijaykumar, A., Fishbach, M., Adhikari, S., & Holz, D. E. 2024, Astrophys. J., 972, 157, doi: 10.3847/1538-4357/ad6140

Virgo Collaboration. 2021, PythonVirgoTools, v5.1.1, git.ligo.org/virgo/virgoapp/PythonVirgoTools

Virtanen, P., et al. 2020, Nature Meth., 17, 261, doi: 10.1038/s41592-019-0686-2

Vitale, S., Gerosa, D., Farr, W. M., & Taylor, S. R. 2020, doi: 10.1007/978-981-15-4702-7_45-1

Waskom, M. 2021, J. Open Source Softw., 6, doi: 10.21105/joss.03021

Wette, K. 2020, SoftwareX, 12, 100634, doi: 10.1016/j.softx.2020.100634

White, D. J., Daw, E. J., & Dhillon, V. S. 2011, Class. Quant. Grav., 28, 085016, doi: 10.1088/0264-9381/28/8/085016

Williams, D., Veitch, J., Chiofalo, M. L., et al. 2023, J. Open Source Softw., 8, 4170, doi: 10.21105/joss.04170

Williams, M. J. 2021, nessai: Nested Sampling with Artificial Intelligence, latest, Zenodo, doi: 10.5281/zenodo.4550693

Williams, M. J., Veitch, J., & Messenger, C. 2021, Phys. Rev. D, 103, 103006, doi: 10.1103/PhysRevD.103.103006

Ye, C., & Fishbach, M. 2021, Phys. Rev. D, 104, 043507, doi: 10.1103/PhysRevD.104.043507

You, Z.-Q., Zhu, X.-J., Ashton, G., Thrane, E., & Zhu, Z.-H. 2021, Astrophys. J., 908, 215, doi: 10.3847/1538-4357/abd4d4

Zazzera, S., Fonseca, J., Baker, T., & Clarkson, C. 2025, Mon. Not. Roy. Astron. Soc., 537, 1912, doi: 10.1093/mnras/staf150

Zonca, A., Singer, L., Lenz, D., et al. 2019, Journal of Open Source Software, 4, 1298, doi: 10.21105/joss.01298